

LOG # D1866U

*Koto White*

# NEW MATERIALS FOR INFRARED TRANSMITTING ELECTROOPTIC FILTERS

Final Technical Report

For period 01 May 1978 through 30 June 1980

Contract MDA 903-78-C-0180

Program Code Number 8D10

Program Element Code 61101E

Hughes Research Laboratories  
3011 Malibu Canyon Road  
Malibu, CA 90265

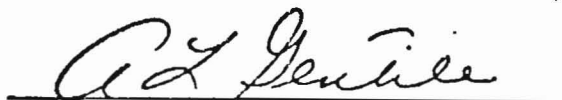
August 1980

Sponsored by

Defense Advanced Research Projects Agency (DoD)

DARPA Order No. 3519

Monitored by DARPA under Contract MDA 903-78-C-0180



A.L. Gentile  
Principal Investigator  
(213) 456-6411

*The views and conclusions contained in this document are those of the authors and should not be interpreted as necessarily representing the official policies, either expressed or implied, of the Defense Advanced Research Projects Agency or the U.S. Government.*

**HMTEC**

ARPA Order Number	3519
Name of Contractor	Hughes Research Laboratories 3011 Malibu Canyon Road Malibu, CA 90265
Effective Date of Contract	1 February 1978
Contract Expiration Date	31 March 1980
Contract Number	MDA 903-78-C-0180
Name and Phone Number of Principal Investigator	A.L. Gentile (213) 456-6411
Contract Period Covered by This Report	1 May 1978 through 30 June 1980

SECURITY CLASSIFICATION OF THIS PAGE (When Data Entered)

REPORT DOCUMENTATION PAGE		READ INSTRUCTIONS BEFORE COMPLETING FORM
1. REPORT NUMBER	2. GOVT ACCESSION NO.	3. RECIPIENT'S CATALOG NUMBER
4. TITLE (and Subtitle) NEW MATERIALS FOR INFRARED TRANSMITTING ELECTROOPTIC FILTERS		5. TYPE OF REPORT & PERIOD COVERED Final Technical Report 1 May 1978-31 June 1980
		6. PERFORMING ORG. REPORT NUMBER
7. AUTHOR(s) A.L. Gentile, S.R. Sashital, N.R. Kyle, R.C. Pastor, M. Braunstein, L.E. Gorre, P.L. Richards, A. Borshchzovsky, R.S. Feigelson, and A. Yariv		8. CONTRACT OR GRANT NUMBER(s)
9. PERFORMING ORGANIZATION NAME AND ADDRESS Hughes Research Laboratories 3011 Malibu Canyon Road Malibu, CA 90265		10. PROGRAM ELEMENT, PROJECT, TASK AREA & WORK UNIT NUMBERS Program Code No. 8D10 Program Element Code 61101
11. CONTROLLING OFFICE NAME AND ADDRESS Defense Advanced Research Projects Agency (DOD) 1400 Wilson Boulevard Arlington, VA 22209		12. REPORT DATE August 1980
		13. NUMBER OF PAGES 88
14. MONITORING AGENCY NAME & ADDRESS (if different from Controlling Office)		15. SECURITY CLASS. (of this report)  UNCLASSIFIED
		15a. DECLASSIFICATION DOWNGRADING SCHEDULE
16. DISTRIBUTION STATEMENT (of this Report)  Approved for public release; distribution unlimited.		
17. DISTRIBUTION STATEMENT (of the abstract entered in Block 20, if different from Report)		
18. SUPPLEMENTARY NOTES		
19. KEY WORDS (Continue on reverse side if necessary and identify by block number) Electrooptic materials                      Ternal chalcogenides IR materials                                      'Defect' chalcopyrites Binary chalcogenides		
20. ABSTRACT (Continue on reverse side if necessary and identify by block number) The primary objectives of this program were to find and develop new infrared (IR) transmitting materials and provide new data on the electro-optic (EO) properties of those materials most likely to have an EO coefficient an order of magnitude higher than those of materials presently in development for tunable filters. A higher EO coefficient would allow an engineering margin on designs for increased voltage from drive chips. In addition, numerous applications can be envisioned for such materials		

UNCLASSIFIED

SECURITY CLASSIFICATION OF THIS PAGE(When Data Entered)

in sensor and communication systems. Since tensor symmetry is the same as for the EO tensor, such a material is also likely to have excellent piezoelectric properties and thereby have many uses as an ultrasonic transducer. Many of the materials can also be used in devices requiring collinear acoustooptic effects.

We have succeeded in identifying two new materials,  $\text{CdIn}_2\text{Te}_4$  and  $\text{AgGaTe}_2$ , which have the potential of having an EO constant at least an order of magnitude higher than those of materials currently available for EO tunable filters.

This project has also led to the development of synthesis techniques for materials preparation and crystal growth of binary and ternary chalcogenide materials. We have worked out a technique to widen the range of materials as far as resistivity is concerned for measurement of dielectric constant by the use of blocking contacts.

Our predictions for new materials with high dielectric constants and hence the potential for high EO coefficients, based on structural analogs, were proven both by experiment and by the theoretical work of A. Yariv and C. Shih. In a parallel program, Shih and Yariv developed a technique for calculating EO coefficient based on the localized band charge model. Their results on binary compounds are in excellent agreement with experiment, and they calculated very high EO coefficients for the materials we predicted.

We recommend the continuation of this type of materials study, specifically to obtain single-crystal samples large enough to make EO coefficient measurements — an aspect we did not complete during this program.

UNCLASSIFIED

SECURITY CLASSIFICATION OF THIS PAGE(When Data Entered)

## TABLE OF CONTENTS

SECTION	PAGE
	5
1	7
A.	7
B.	7
C.	10
2	13
3	17
A.	17
B.	24
C.	25
D.	41
E.	45
4	51
A.	51
B.	54
C.	62
5	73
6	77
	79
	81
	87

## LIST OF ILLUSTRATIONS

FIGURE		PAGE
1	Point groups for longitudinal EO effect . . . . .	8
2	Point groups for transverse EO effect . . . . .	9
3	Point groups for collinear acoustooptic effect . . . . .	10
4	$\text{LiNbO}_3$ structure . . . . .	14
5	Importance of octahedral coordination to EO effect . . . . .	14
6	Structure of $\text{ZnIn}_2\text{S}_4$ . . . . .	16
7	Reaction process I for $\text{GeS}_2$ formation . . . . .	18
8	Zone refiner used for formation of $\text{GeS}_2$ . . . . .	18
9	X-ray diffraction pattern: orthorhombic $\text{GeS}_2$ . . . . .	20
10	Phase equilibria in the system Ge-S . . . . .	21
11	X-ray diffraction pattern (indexed) of $\text{GeS}_2$ . . . . .	22
12	Preparation of $\text{In}_2\text{Se}_3$ or $\text{In}_2\text{S}_3$ . . . . .	26
13	Sublimation purification of II-VI compounds . . . . .	27
14	X-ray diffraction pattern of $\text{Zn}_3\text{In}_2\text{S}_6$ . . . . .	31
15	X-ray diffraction pattern of $\text{ZnIn}_2\text{S}_4$ . . . . .	32
16	X-ray diffraction pattern of $\text{CdIn}_2\text{S}_4$ . . . . .	33
17	X-ray diffraction pattern of $\text{CdIn}_2\text{Se}_4$ . . . . .	34
18	X-ray diffraction pattern of $\text{CdIn}_2\text{S}_4$ . . . . .	38
19	Phase equilibrium diagram for $\text{CdTe-In}_2\text{Te}_3$ . . . . .	40
20	X-ray diffraction pattern of $\text{CdIn}_2\text{Te}_4$ . . . . .	42
21	Ingot containing single-crystal $\text{CdIn}_2\text{Te}_4$ . . . . .	43

FIGURE		PAGE
22	SEM photograph of tip of $\text{CdIn}_2\text{Te}_4$ . . . . .	43
23	X-ray diffraction pattern of $\text{Cu}_2\text{GeS}_3$ . . . . .	46
24	X-ray diffraction pattern of cubic $\text{Cu}_2\text{GeTe}_3$ . . . . .	47
25	X-ray diffraction pattern of $\text{Cu}_2\text{CdGeTe}_4$ . . . . .	48
26	Electrical testing apparatus . . . . .	49
27	Electrical testing apparatus (internal view) . . . . .	49
28	$\text{GeS}_2$ dielectric constant as a function of frequency . . . . .	56
29	Dissipation factor versus frequency . . . . .	57
30	$\tan \delta$ versus frequency for $\text{GeSe}_2$ . . . . .	58
31	Dissipation factor versus frequency for $\text{ZnGa}_2\text{S}_4$ . . . . .	59
32	IR transmission spectrum: $\text{AgGaTe}_2$ . . . . .	61
33	Dielectric relaxation of $\text{ZnSiAs}_2$ . . . . .	63
34	Far-IR transmission of $\text{GeS}_2$ (Curve 1) . . . . .	64
35	Far-IR transmission of $\text{AgInTe}_2$ . . . . .	66
36	Far-IR transmission of $\text{CdIn}_2\text{Te}_4$ . . . . .	67
37	Far-IR transmission of $\text{AgInSe}_2$ . . . . .	68
38	Far-IR transmission spectrum of $\text{TlSe}$ . . . . .	69
39	Far-IR transmission of $\text{AgGa}(\text{S,Se})_2$ . . . . .	71

## SECTION 1

### INTRODUCTION AND SUMMARY

#### A. PROGRAM OBJECTIVES

The primary objectives of this program were to find and develop new infrared (IR) transmitting materials and provide new data on the electro-optic (EO) properties of those materials most likely to have an EO coefficient an order of magnitude higher than those of materials presently in development for tunable filters. A higher EO coefficient would allow an engineering margin on designs for increased voltage from drive chips. In addition, numerous applications can be envisioned for such materials in sensor and communication systems. Since tensor symmetry is the same as for the EO tensor, such a material is also likely to have excellent piezoelectric properties and thereby have many uses as an ultrasonic transducer. Many of the materials can also be used in devices requiring collinear acoustooptic effects.

#### B. BACKGROUND

Approximately three years ago, personnel at Hughes Research Laboratories (HRL) reviewed the requirements for an IR transmitting, spectrally tunable filter for the HALO program.<sup>1</sup> We concluded that both the total power consumption and the drive power density would be excessive if an acoustooptic filter were used. This led us toward the invention of an electronic analog to the  $\Delta\theta$  filter. Such a filter would require orders of magnitude less drive power. Progress on the reduction to practice of this invention has been excellent, but development work is not without technical risks. The test-sample-acquisition and materials-development tasks we have already completed in pursuit of the filter provided us with a data base of EO crystals (mostly crystals having the chalcopyrite structure (e.g.,  $\text{AgGaS}_2$ ), which was selected for the HALO program. A material having an EO coefficient an



order of magnitude greater than that of  $\text{AsGaS}_2$  would reduce required maximum drive voltages to less than 100 V maximum.

A parallel study<sup>2</sup> made at HRL concerned with fundamental EO concepts led to the extension of the number of allowable crystal classes suitable for application to tunable filter designs when crystallographic orientations other than those of the principal axes are used for the selected direction of light propagation. Figure 1 shows the crystal classes as indicated by the point groups, which are useful for devices employing the longitudinal EO effect using principal axes (i.e., unrotated) and those additional point groups that become applicable when principal axes are rotated. Figure 2 shows a similar extension of point groups for materials having the transverse EO effect. Materials falling into the indicated point groups are applicable to tunable filters recently designed at HRL. The crystal classes containing materials useful in collinear acousto-optic devices are shown in Figure 3.

CRYSTAL STRUCTURES 6364-7A

TYPE	POINT GROUP						
CUBIC	23,	M3,	432,	$\bar{4}3M$ ,	M3M		
HEXAGONAL	(6),	$\bar{6}$ ,	6/M,	(622),	6MM,	$\bar{6}M2$	6/MMM
TRIGONAL	(3),	$\bar{3}$ ,	(32),	$\bar{3}M$ ,	$\bar{3}M$		
TETRAGONAL	(4),	$\bar{4}$ ,	4/M,	(422),	4MM,	(42M)	4/MMM
ORTHORHOMBIC	(222),	$\bar{2}22$ ,	MMM				
MONOCLINIC	(2),	M,	2/M				
TRICLINIC	(1),	$\bar{1}$					

LONGITUDINAL UNROTATED
  LONGITUDINAL ROTATED

Figure 1. Point groups for longitudinal EO effect.

## CRYSTAL STRUCTURES

TYPE	POINT GROUP					
CUBIC	23,	M <sub>3</sub> ,	432,	$\bar{4}3M$ ,	M <sub>3</sub> M	
HEXAGONAL	6,	$\bar{6}$ ,	6/M,	622,	6MM	$\bar{6}M2$ , 6/MMM
TRIGONAL	3,	$\bar{3}$ ,	32,	3M,	$\bar{3}M$	
TETRAGONAL	4,	$\bar{4}$ ,	4/M,	422,	4MM,	$\bar{4}2M$ 4/MMM
ORTHORHOMBIC	222,	MM <sub>2</sub> ,	MMM			
MONOCLINIC	2,	M,	2/M			
TRICLINIC	1,	$\bar{1}$				

○ TRANSVERSE  
UNROTATED

□ TRANSVERSE  
ROTATED

Figure 2. Point groups for transverse EO effect.

CRYSTAL STRUCTURES

6384-7B

TYPE	POINT GROUP						
CUBIC	23,	M3,	432,	$\bar{4}3M$ ,	M3M		
HEXAGONAL	$\diamond 6,$	$\diamond \bar{6},$	$\diamond 6/M,$	622,	6MM,	$\bar{6}M2,$	6/MMM
TRIGONAL	3,	$\bar{3},$	$\diamond 32,$	$\diamond 3M,$	$\diamond \bar{3}M$		
TETRAGONAL	$\diamond 4,$	$\diamond \bar{4},$	$\diamond 4/M,$	422,	4MM,	$\bar{4}2M,$	4/MMM
ORTHORHOMBIC	222,	MM2,	MMM				
MONOCLINIC	2,	M,	2/M				
TRICLINIC	1,	$\bar{1}$					

$\diamond$  ACOUSTO OPTIC (COLLINEAR)

Figure 3. Point groups for collinear acoustooptic effect.

The use of axis rotation considerably widens the selection of new materials available for tunable filters. However, an extensive literature search reveals that very little data was available on many of these materials.

C. SUMMARY

We have succeeded in identifying two new materials,  $CdIn_2Te_4$  and  $AgGaTe_2$ , which have the potential of having an EO constant at least an order of magnitude higher than those of materials currently available for EO tunable filters.

This project has also led to the development of synthesis techniques for materials preparation and crystal growth of binary and ternary chalcogenide materials. We have worked out a technique to widen the

range of materials as far as resistivity is concerned for measurement of dielectric constant by the use of blocking contacts.

Our predictions for new materials with high dielectric constants and hence the potential for high EO coefficients, based on structural analogs, was proven both by experiment and by the theoretical work of A. Yariv and C. Shih. In a parallel program, Shih and Yariv developed a technique for calculating EO coefficient based on the localized bond charge model. Their results on binary compounds are in excellent agreement with experiment, and they calculated very high EO coefficients for the materials we predicted.

We recommend the continuation of this type of materials study, specifically to obtain single-crystal samples large enough to make EO coefficient measurements - an aspect we did not complete during this program.

## SECTION 2

### MATERIALS SELECTION

This investigation involved the selection of new materials based on compound semiconductors that have point groups appropriate for a programmable spectral filter. The prime candidates were chosen based on a semiconducting analog to the best observed EO materials in the visible spectrum range (i.e.,  $\text{LiNbO}_3$  and  $\text{LiTaO}_3$ ).

We applied the principles of crystal chemistry to a structural analog of lithium niobate within an allowed crystal class to find a similarly large E-O coefficient in a chalcogenide (IR transmitting) material. A detailed analysis of the lithium niobate structure (Figure 4) shows that it consists of a planar sheet structure of anions (oxygen) in approximately hexagonal close packing, which results in distorted, partially occupied octahedral sites — essentially a defect structure. These sites are one-third occupied by niobium and one-third by lithium; the remainder are vacant. The sequence of distorted octahedra along the c-axis with Nb at the origin is Nb-V-Li-Nb-V-Li, where V is a vacancy.

A plot of the vertical position of Nb (in an octahedral site) versus potential energy (Figure 5) shows curves for temperatures above and below the Curie point ( $T_c$ ). The existence of curve 2 (with  $T \approx T_c$ ) indicates a large ionic contribution to the polarizability, contributing to a large EO coefficient, which, for  $\text{LiNbO}_3$ , is  $32 \times 10^{-12}$  m/V.

An obstacle in seeking a semiconductor analog appeared to be the tetrahedral coordination typical of semiconducting materials (e.g., zincblende and chalcopyrite structures). However, our study uncovered a group of materials of the general formula  $A^{II}B_2^{III}C_4^{VI}$  that are closely analogous to  $\text{LiNbO}_3$  and thereby show considerable promise of having high EO coefficients. These materials have been described<sup>3</sup> as crystallizing in the crystal classes  $3m$  (same as  $\text{LiNbO}_3$ ),  $\bar{4}$ , and  $\bar{4}2m$  (same as chalcopyrites); all of these are potentially usable for tunable filters.

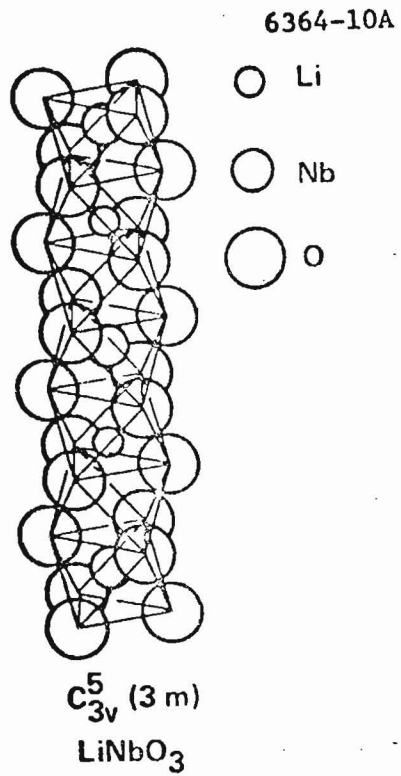


Figure 4. LiNbO<sub>3</sub> structure.

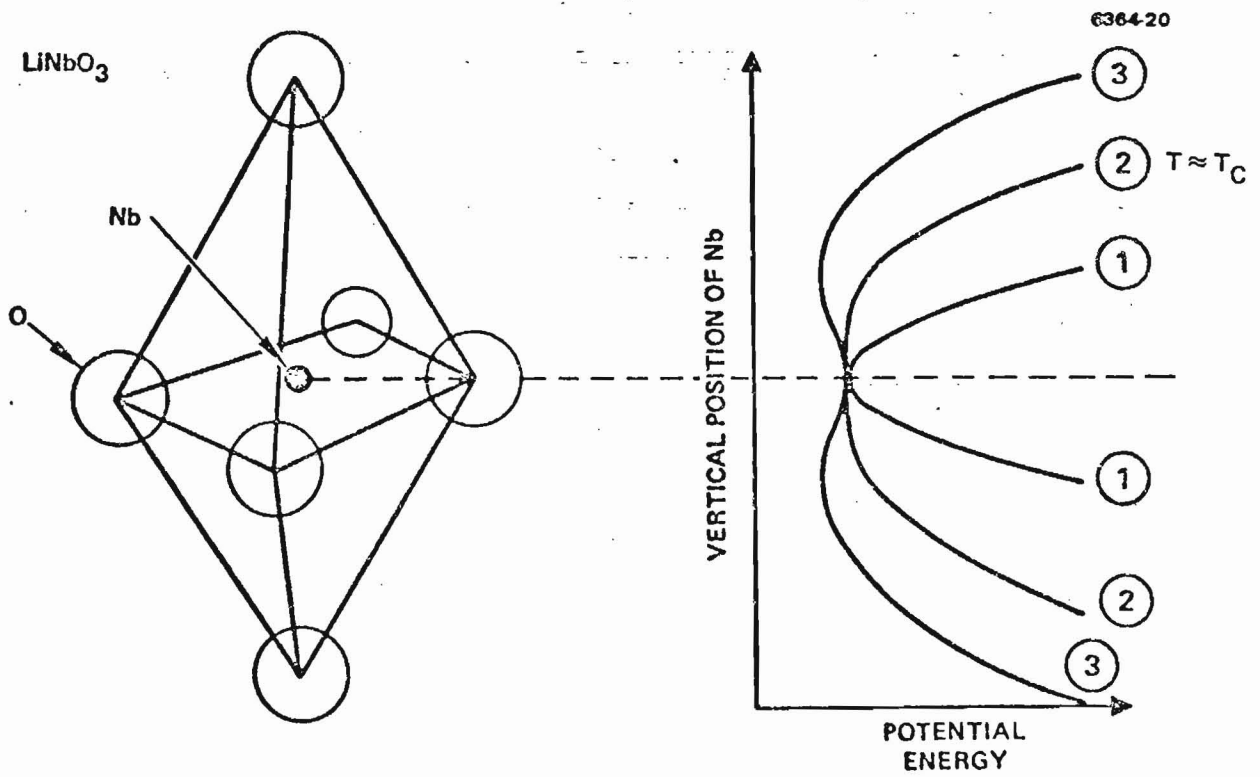


Figure 5. Importance of octahedral coordination to EO effect.

The  $3m$  point group, of which  $ZnIn_2S_4$  is a member (Figure 6), has a unit cell consisting of 12 closely packed sulfur layers. Octahedral sites contain one-half the total number of In atoms; Zn atoms and the other half of the In atoms are in tetrahedral sites. An inverse structure has also been described in which the divalent and one-half of the trivalent atoms are in octahedral sites; one-half of the trivalent are in tetrahedral sites, leaving a fraction of vacancies in each type of site. The inverse structure has been described for  $XIn_2S_4$ , where X is Mg, Fe, Co, Ni,  $CdGa_2S_4$ , or  $CdIn_2Te_4$ . A structural comparison of two chalcogenides with  $LiNbO_3$  is shown in Table 1. Existing theories of the EO effect in crystals predict that the EO coefficients of these materials should be significantly higher than those of the chalcopyrites. There is little data in the literature concerning the preparation and properties of these materials.

Because the lead time required to synthesize single-crystal samples is long, our experimental approach involved synthesizing small polycrystalline samples of a wide selection of candidate materials and then measuring the dielectric constant of each at ambient and liquid nitrogen temperatures. The low-frequency dielectric constant is essentially a measure of lattice polarizability. A large lattice contribution to the EO coefficient is essential but not sufficient for a large EO effect. Thus, measuring the dielectric constant is an excellent screening method in a materials survey of this nature.

A second phase planned for this program was aimed at (1) growing single crystals of at least two materials such as  $ZnIn_2S_4$  and  $CdIn_2Te_4$  or the best (highest dielectric constant) from the materials surveyed in the first phase of investigation and (2) subsequently evaluating the electrical and optical properties of these materials, including EO coefficient, transmission range, resistivity, refractive index, and birefringence.

Table 1. Structural Comparisons of Chalcogenides with  $\text{LiNbO}_3$

PROPERTY	$\text{LiNbO}_3$	$\text{ZnIn}_2\text{S}_4$	$\text{CdIn}_2\text{Te}_2$ <span style="float: right;">6384-12</span>
CRYSTAL CLASS	3m	3m	$\bar{4}$
STRUCTURE CHARACTER	DEFECT	DEFECT	DEFECT
ANIONS	LAYER CLOSE PACKING (OXYGEN)	LAYER CLOSE PACKING (SULFUR)	LAYER CLOSE PACKING (TELLURIUM)
COORDINATION	DISTORTED OCTAHEDRAL	MIXED OCTAHEDRAL TETRAHEDRAL	MIXED (INVERSE) OCTAHEDRAL TETRAHEDRAL
SITE OCCUPANCY	$\left\{ \begin{array}{l} 1/3 \text{ Nb} \\ 1/3 \text{ Li} \\ 1/3 \text{ VACANCY} \end{array} \right.$	OCTAHEDRAL $\left\{ \begin{array}{l} 1/2 \text{ In}_{\text{total}} \\ 1/2 \text{ In}_{\text{total}} \\ \text{Zn}_{\text{total}} \end{array} \right.$ TETRAHEDRAL $\left\{ \begin{array}{l} 1/2 \text{ In}_{\text{total}} \\ \text{Zn}_{\text{total}} \end{array} \right.$	$\left\{ \begin{array}{l} 1/2 \text{ In}_{\text{total}} \\ \text{Cd}_{\text{total}} \\ 1/2 \text{ In}_{\text{total}} \end{array} \right.$
E-O COEFFICIENT, $r_{ij}$	$32 \times 10^{-12} \text{ m/V}$	?	?

2 VACANT METAL SITES  
"DEFECT CHALCOPYRITE"

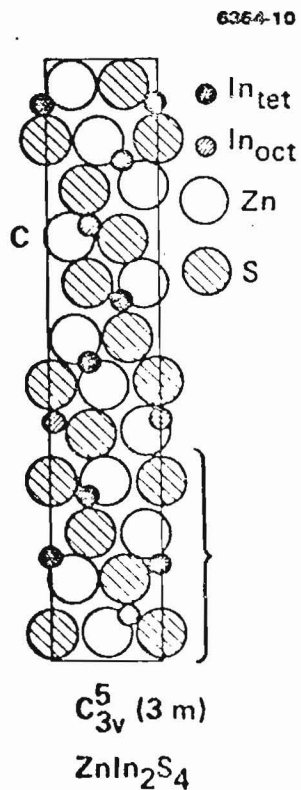


Figure 6. Structure of  $\text{ZnIn}_2\text{S}_4$ .



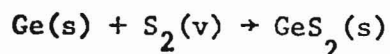
### SECTION 3

#### MATERIALS SYNTHESIS

##### A. BINARY COMPOUNDS

##### 1. Synthesis of GeS<sub>2</sub>

Our first attempt to synthesize GeS<sub>2</sub> (orthorhombic, MM2), we used a reaction procedure similar to one developed at HRL<sup>4</sup> for AgGaS<sub>2</sub>. High-purity germanium (greater than 99.9999% pure) was placed in a fused quartz boat and subsequently in a sealed, evacuated fused silica tube with the required amount of sulfur (minimum 99.9995+% pure) to react according to the relation:



at temperatures where sulfur vapor (v) reacts with solid (s) germanium to form the solid compound GeS<sub>2</sub>. A schematic of the apparatus used is shown in Figure 7.

The reaction takes place readily as the tube is moved into the hot furnace even though Ge is solid (melting point = 956°C). However, this procedure yielded two products: GeS<sub>2</sub> and GeS. Although the experiment was designed to prevent formation of GeS by using a temperature at which that compound is unstable and decomposes, a significant amount of it transported to the cold portion of the tube and remained intact. GeS<sub>2</sub>, which also formed, sublimed as well to the cooler portion of the tube. Before completion of the run, the combined sublimate plugged the tube, isolating the remaining elements and preventing further reaction. At this point, the run was aborted.

To avoid a repeat of this problem, we modified our approach using a zone refiner (Figure 8) with two furnaces (two zones). In addition, a heated outer tube employing a flat nichrome ribbon to maintain a minimum temperature throughout the tube of ~400°C was established to maintain a constant overpressure of sulfur above the germanium. The zone furnaces were heated to 850°C and 800°C, respectively; the temperature of these furnaces is not critical. Rapid reaction was observed

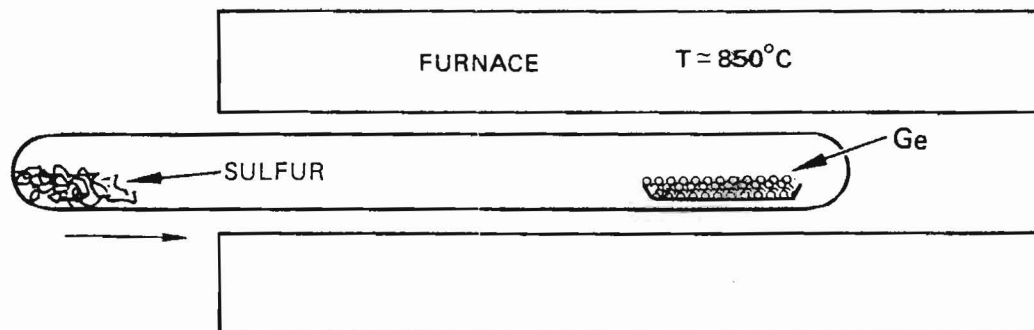


Figure 7. Reaction process I for  $\text{GeS}_2$  formation.

M12463

6948-2R1

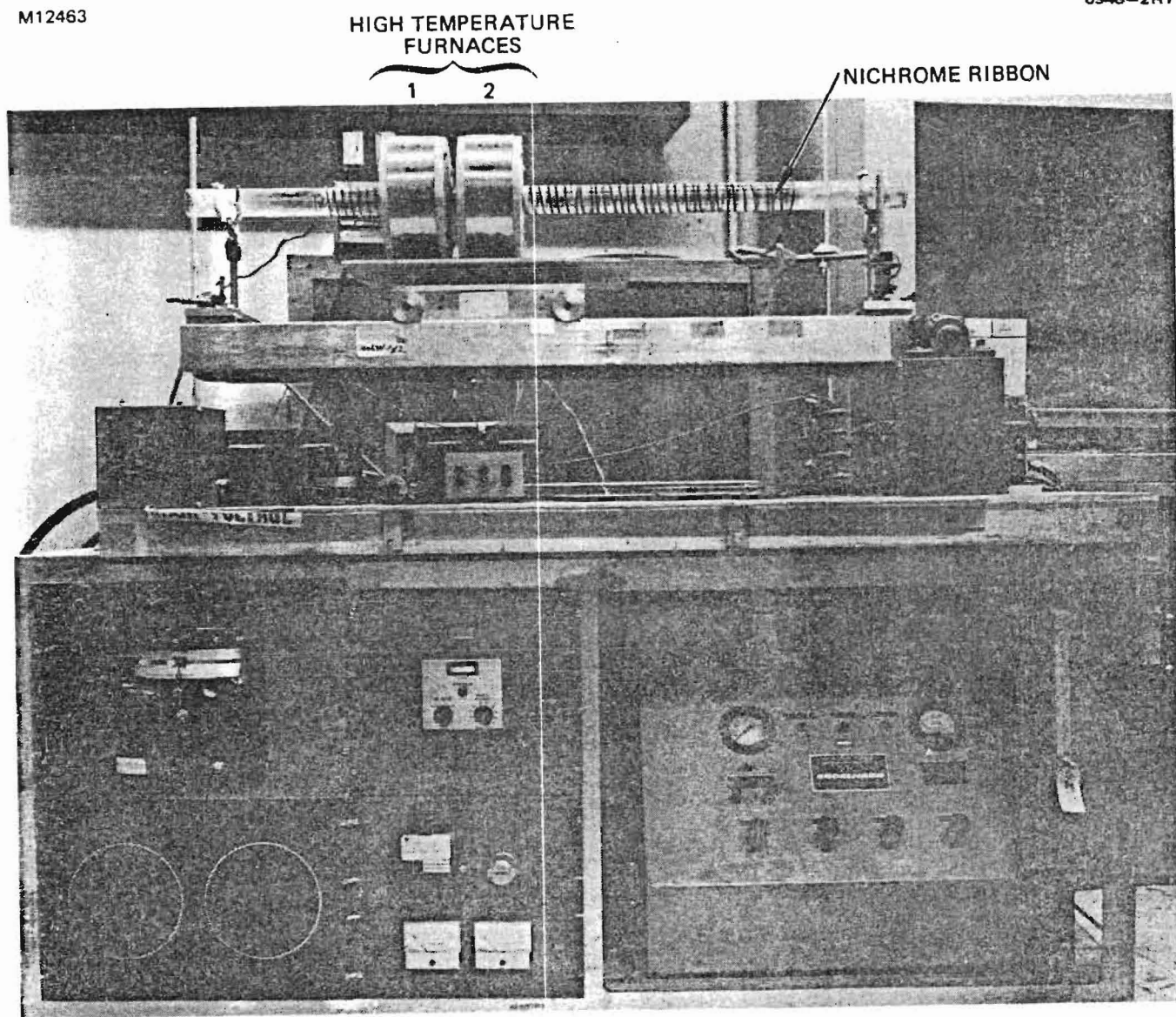


Figure 8. Zone refiner used for formation of  $\text{GeS}_2$ .

between the sulfur vapor and germanium, forming  $\text{GeS}_2$  (white in color), which sublimed to a cooler portion of the tube. A total of six zone passes (three passes times two furnaces) was made following in situ heating during which the germanium sat in the higher temperature furnace until the reaction with sulfur appeared to have gone to completion. The resulting product was white crystalline  $\text{GeS}_2$  with a small residue of yellow amorphous material ( $\text{GeS}_2$ ). The crystalline material was identified by X-ray diffraction analysis to be orthorhombic  $\text{GeS}_2$  (see Figure 9). The melting point of  $\text{GeS}_2$  is reported<sup>5</sup> to be  $840 \pm 5^\circ\text{C}$ . The equilibrium phase diagram<sup>5</sup> for the system Ge-S is shown in Figure 10.

Two approaches were taken to grow single crystals of  $\text{GeS}_2$ : sublimation and Bridgman techniques. In the preparation of  $\text{GeS}_2$  by direct reaction of the elements, the observation that  $\text{GeS}_2$  sublimed readily presented the possibility that  $\text{GeS}_2$  could be grown by sublimation. The compound was encapsulated under vacuum into a 1-cm (i.d.) tube, 20 cm in length, and placed in a furnace with a flat profile at  $700^\circ\text{C}$ . The tube was pulled through the profile at a rate of 0.1 cm/hr for 15 days. No sublimation took place. The material was solid and polycrystalline.

No information could be found on the vapor pressure of  $\text{GeS}_2$  at any temperature. Since the compound was observed to sublime and possibly to decompose at high temperatures, attempts at Bridgman growth would increase the possibility of an explosion due to excessively high vapor pressures. The Bridgman method was tried in a furnace set at  $850^\circ\text{C}$ . The rate of growth was 2 mm/hr. The run was taken out of the furnace hot before the last remaining liquid had frozen. A dark brown vapor was observed above the compound, indicating a sulfur pressure over the melt and hence some decomposition. The result was a yellowish crystalline material identified as  $\text{GeS}_2$  by X-ray diffraction (Figure 11), from which single-crystal layers could be peeled. An amber-colored amorphous section (the last to freeze) was also identified as  $\text{GeS}_2$  by microprobe analysis.

7483-B

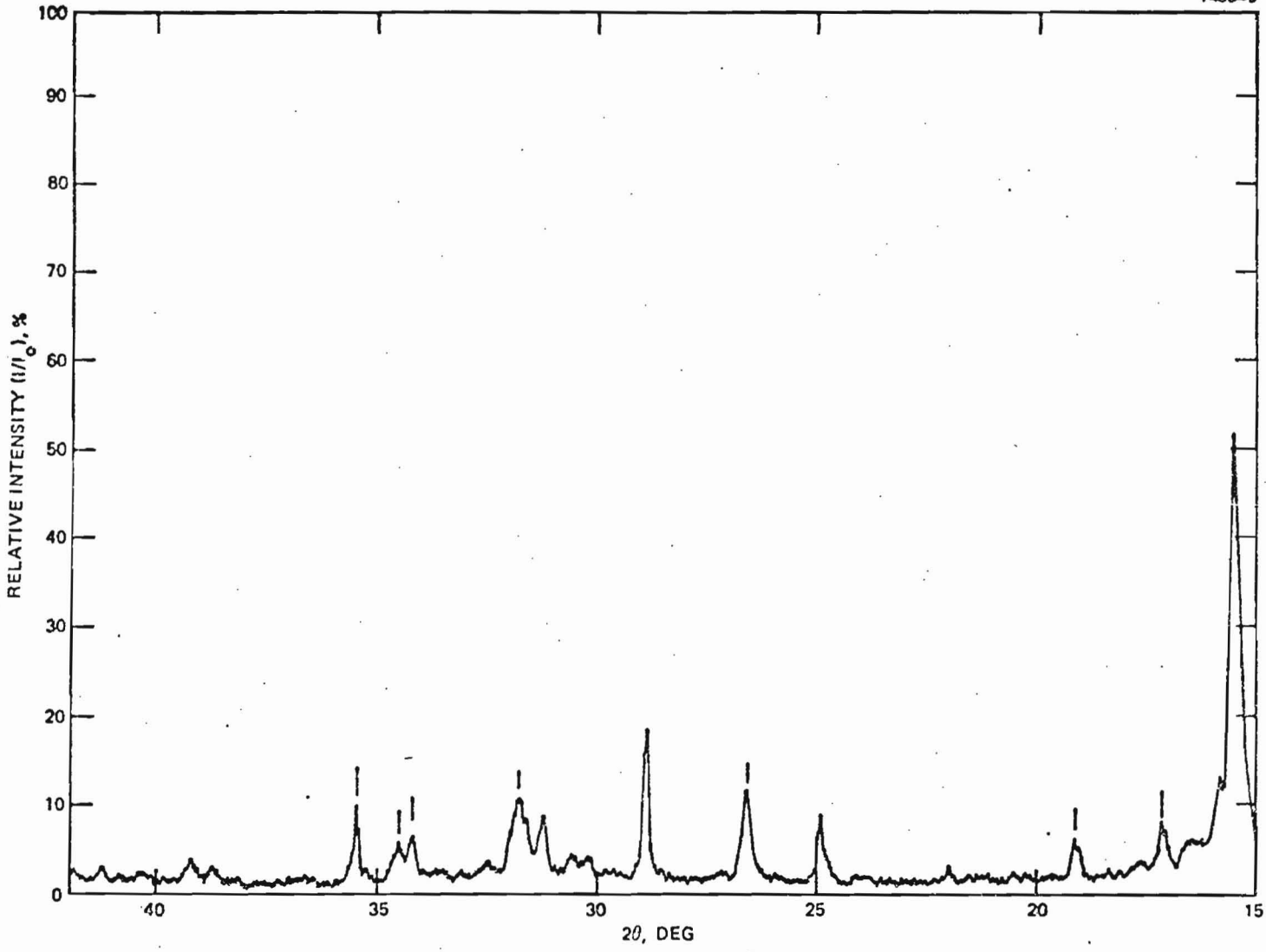


Figure 9. X-ray diffraction pattern: orthorhombic GeS<sub>2</sub>.

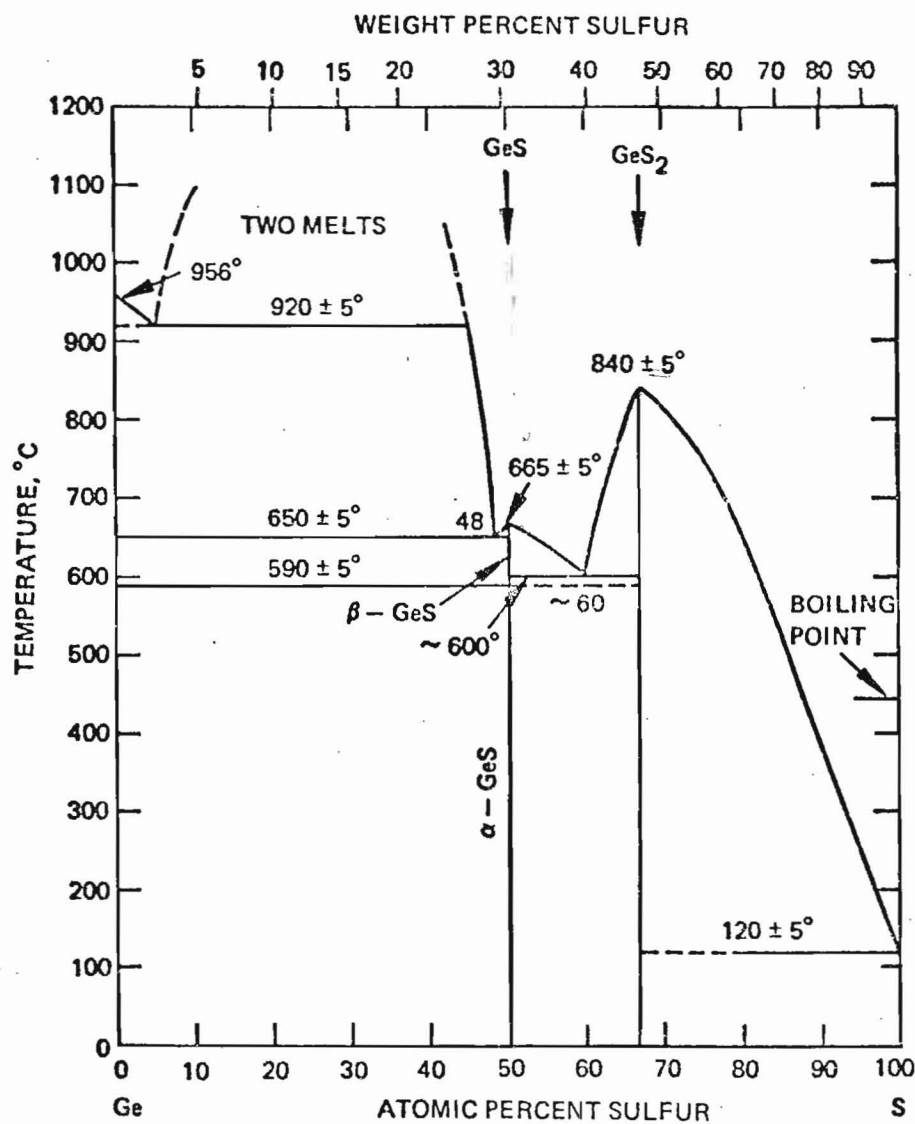


Figure 10. Phase equilibria in the system Ge-S.

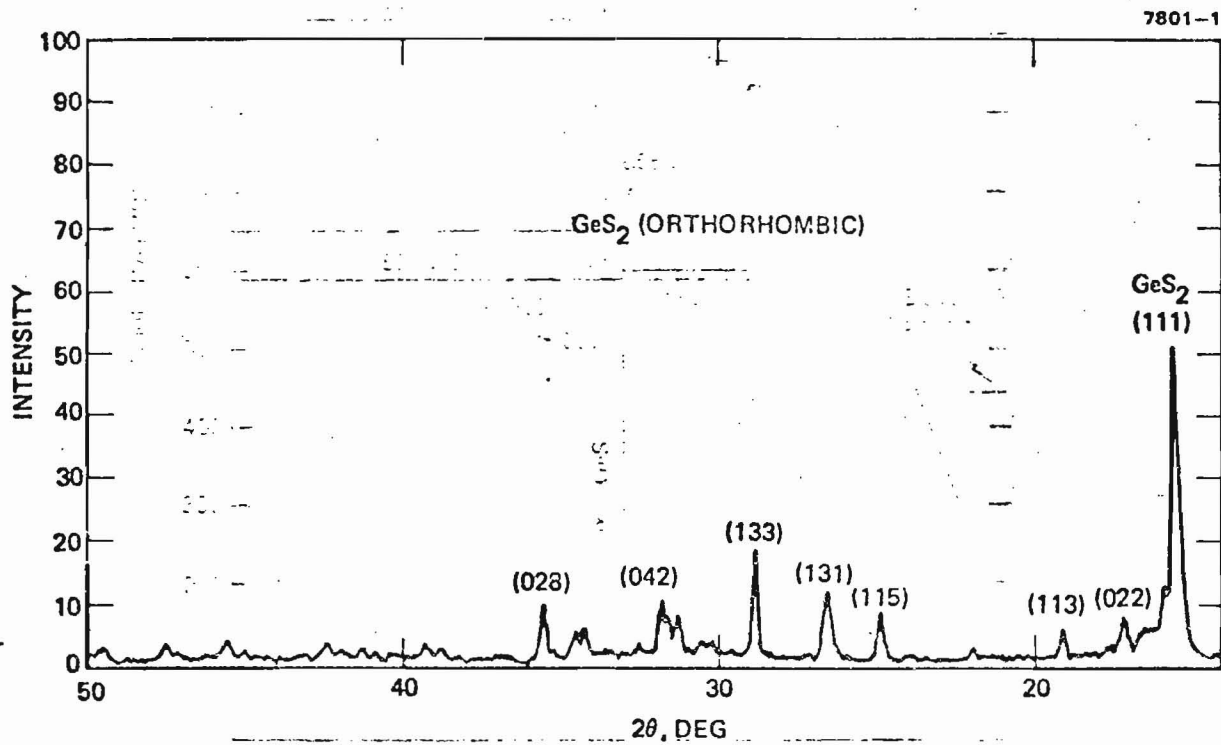


Figure 11. X-ray diffraction pattern (indexed) of GeS<sub>2</sub>.

## 2. Preparation of GeSe<sub>2</sub>

GeSe<sub>2</sub> was synthesized by mixing stoichiometric amounts of Ge and Se in two vitreous silica ampoules under a flow of nitrogen. An excess of 1.0 g of Se was added to provide 1 atm of Se<sub>2</sub> vapor at the processing temperature. The tube was then evacuated and sealed.

The setup was heated to 410°C over a period of 16 hr, and 690°C for 30 hr (boiling point of Se is 688°C). The color of the Se<sub>2</sub> vapor was used as an indicator of the extent of completion of the reaction. When the color of the vapor appeared to become lighter, the temperature was raised to 725°C for 18 hr, then to 740°C (melting point of GeSe<sub>2</sub>) for four days. After this time, no Se<sub>2</sub> vapor was observed and the material sublimed to the colder ends of the tube. Part of the tube was pushed out of the furnaces to attempt to nucleate and grow crystals. The temperature of the furnace was increased to 765°C in two days, after which the setup was slowly cooled to room temperature.

The material obtained was a mica-like mixture of gray, red, and yellow. However, X-ray analysis showed the material to be GeSe<sub>2</sub>. The color differences were caused by variations in thickness.

The material was transferred into a vitreous SiO<sub>2</sub> crystal growth tube, evacuated, and sealed. Crystal growth by the vertical Bridgman method was attempted at 800°C. The resulting material was polycrystalline. Samples were sliced and submitted for dielectric constant measurements.

## 3. Preparation of NbGe<sub>2</sub>

The preparation of NbGe<sub>2</sub> was done using the constituent elements powdered into an intimate mixture. The mixture was placed in a vitreous carbon boat inside an aluminum tube. Under a nitrogen atmosphere, the setup was heated to 1400°C for 1.5 hr and 1450° for 2 hr. The material was heated to 1400°C for 1.5 hr and 1450° for 2 hr. The material was sintered. X-ray analysis showed the material to be a mixture of NbGe<sub>2</sub> and Ge.

## B. TERNARY CHALCOPYRITES

### 1. AgGaTe<sub>2</sub>

Polycrystalline ingots of AgGaTe<sub>2</sub> were grown from the melt using the Bridgman-Stockbarger technique. AgGaTe<sub>2</sub> is believed to be a congruently melting chalcopyrite, but the existence region has not been studied in detail. Successful synthesis of AgGaTe<sub>2</sub> was achieved from Ga<sub>2</sub>Te<sub>3</sub>-rich solution. Our measurements, as discussed below, indicate the possibility of variations in stoichiometry within the ingot.

### 2. Synthesis of LiGaS<sub>2</sub>

Because Li<sub>2</sub>S is deliquescent and highly reactive to water in the atmosphere, the ternary chalcogenide LiGaS<sub>2</sub> was prepared by reaction of H<sub>2</sub>S with LiGaO<sub>2</sub> rather than with the binary compounds Li<sub>2</sub>S and Ga<sub>2</sub>S<sub>3</sub>. Gallium metal was first dissolved in 15 N HNO<sub>3</sub>; after complete dissolution, a stoichiometric amount of LiNO<sub>3</sub> was added. The mixture was evaporated to dryness on a hot plate to obtain LiGa(NO<sub>3</sub>)<sub>4</sub>. This material was transferred into a fused silica boat in a fused silica ampoule.

Since the physical and chemical properties of LiGaS<sub>2</sub> are not reported in the handbooks, the preparation had to be carried out cautiously; a great part of it depended on observation. The set-up was heated slowly to approximately 600°C under N<sub>2</sub> to decompose the nitrate to the oxide. When brown fumes of nitrogen oxide were no longer visible, the temperature was raised to 800°C over a period of 4 hr under H<sub>2</sub>S. Emerging H<sub>2</sub>S gas flowed into an outlet connected to two bubblers containing NH<sub>4</sub>OH; these acted as H<sub>2</sub>S traps. X-ray diffraction showed that the material was mostly LiGaO<sub>2</sub>.

The LiGaO<sub>2</sub> was ground and reheated to 1000°C for 2 hr. This time, the material was heterogeneous: colored pink and white. X-ray analysis of both phases gave the same lines, but the pink phase had better defined lines and the LiGaO<sub>2</sub> lines were not as intense. There were other lines present and these could not be identified. (There is no ASTM index card for LiGaS<sub>2</sub>.) These lines could not be attributed to Li<sub>2</sub>S, Ga<sub>2</sub>S<sub>3</sub>, LiGa silicates, Li silicates, or Ga oxides.



The material was ground again and then reheated to 1000°C for 3 hr in H<sub>2</sub>S and N<sub>2</sub>. Melting was observed. X-ray analysis showed the same lines as seen during the previous run. Since there was some attack on the SiO<sub>2</sub> (probably due to the Li<sub>2</sub>O), the run was repeated using a graphite boat at 1000°C for 3 hr under H<sub>2</sub>S and N<sub>2</sub>. The final product, which was mostly LiGaS<sub>2</sub>, still retained a significant amount of oxide.

### C. DEFECT CHALCOPYRITE COMPOUNDS

Compounds of the type A<sup>II</sup>B<sub>2</sub><sup>III</sup>C<sub>4</sub><sup>IV</sup> are known as defect chalcopyrite compounds. The synthesis of these compounds (e.g., ZnIn<sub>2</sub>S<sub>4</sub>) was initially approached by vapor transport (using iodine as a transport medium) because of the various properties of these compounds, including high melting points and incongruent melting properties.<sup>3</sup> The selection was based on reports of crystal growth in the Russian literature as cited in Ref. 3. We used mixtures of II-VI and III-VI compounds as starting materials for the reaction. High-purity ZnS, ZnSe, and CdS were purchased from General Electric Company and further purified by vacuum sublimation. In this process, a dynamic vacuum is used (Figure 12); pumping is continuous through a liquid nitrogen trap to prevent back-diffusion as well as to enhance the removal of impurities by the addition of a cryogenic pump. The fused quartz tube is transported (raised) through a thermal gradient as indicated in Figure 12. The material sublimates to a cooler portion of the tube; many more volatile impurities are removed and trapped by pumping while others segregate according to their vapor-solid equilibrium temperatures.

The synthesis of In<sub>2</sub>S<sub>3</sub> involved a two-temperature process using two vitreous silica boats in a vitreous silica tube (Figure 13). A stoichiometric equivalent of sulfur plus a small excess to provide 1 atm overpressure of S<sub>2</sub> at the reaction temperature was introduced into the first boat at one end of the tube and then melted, cooled, and pumped to remove occluded H<sub>2</sub>O. The stoichiometric weight of indium was placed into the second boat. Since the In pellets appeared slightly oxidized, the In end was heated to 1000°C for 2 hr under a flow of H<sub>2</sub> keeping the other (sulfur-containing) end cool. The tube was cooled, evacuated to approximately 100 μm, and then sealed.

7801-3

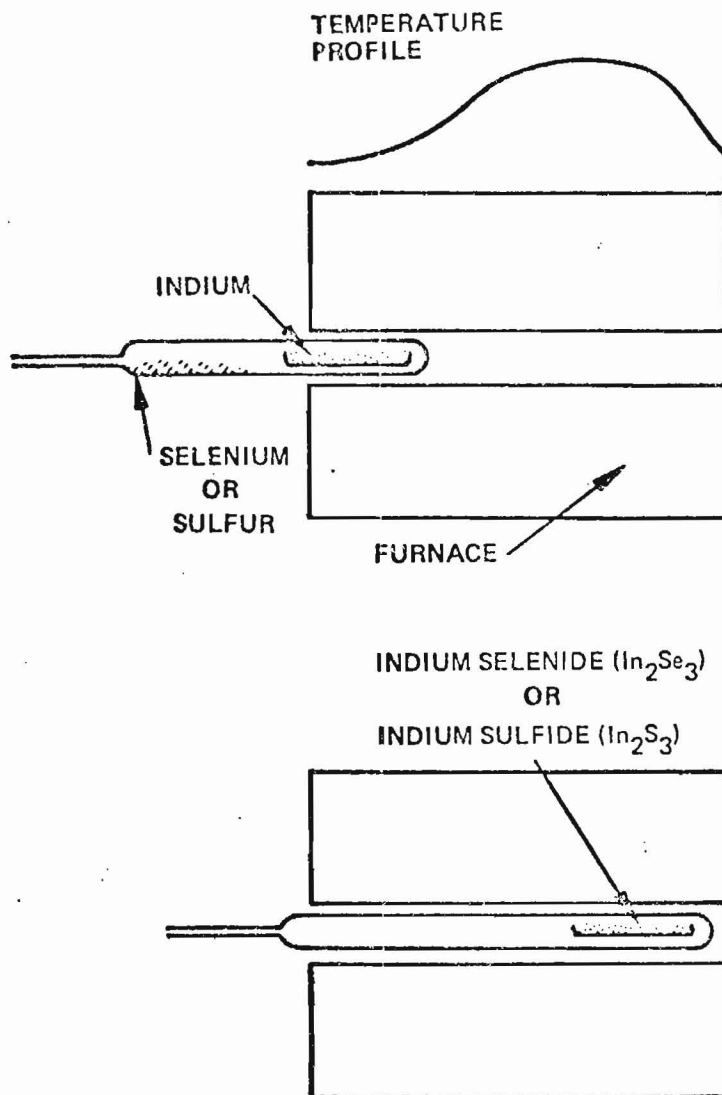


Figure 12. Preparation of  $\text{In}_2\text{Se}_3$  or  $\text{In}_2\text{S}_3$ .

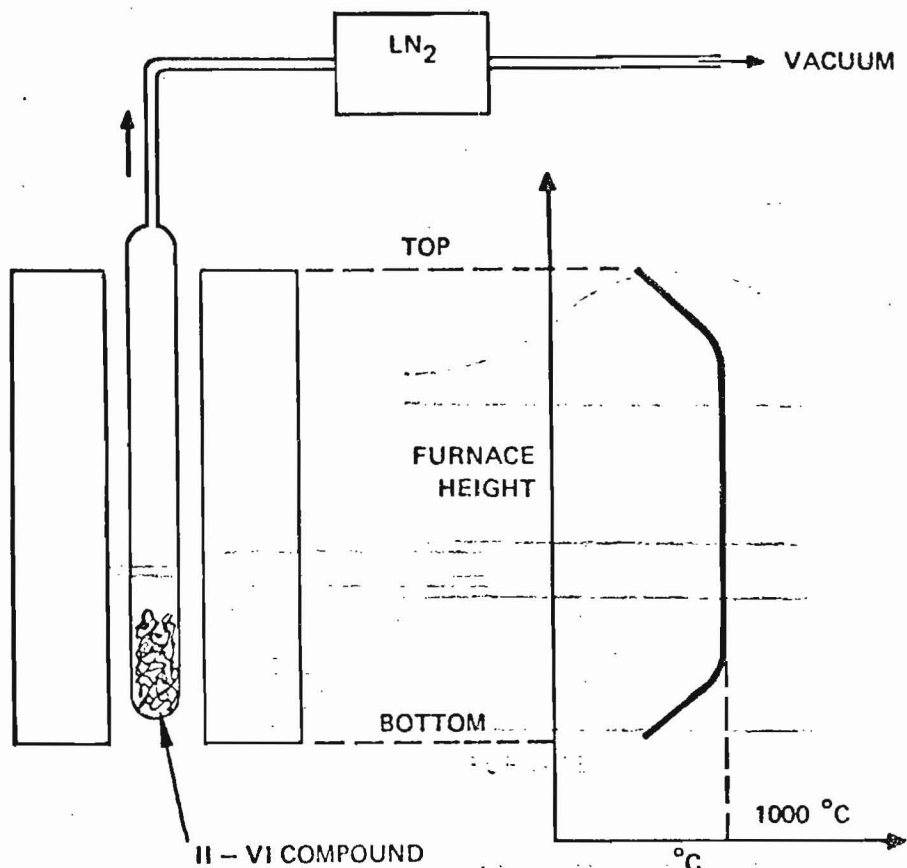
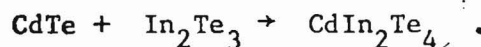
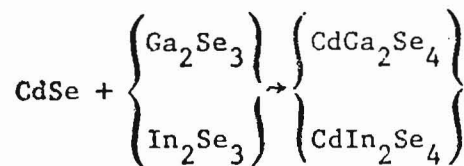
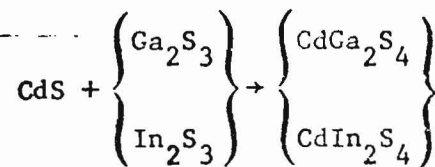
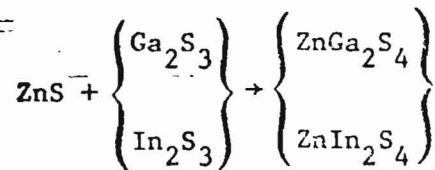


Figure 13. Sublimation purification of II-VI compounds.

Precaution was taken to avoid a runaway exothermic reaction. The preparation involved slow heating to 900°C for In and 450°C for S within a 12-hr period. The last step consisted of heating to transport all unreacted sulfur to the sulfur-containing end. The bulk material produced was identified by X-ray diffraction analysis to be  $\beta$  - In<sub>2</sub>S<sub>3</sub>.

Mixtures of binary chalcogenides can be used as source material in the gas transport reaction method to synthesize ternary compound crystals. Following the preparation of ZnS, CdS, CdSe, CdTe, In<sub>2</sub>Se<sub>3</sub>, Ga<sub>2</sub>S<sub>3</sub>, In<sub>2</sub>S<sub>3</sub>, Ga<sub>2</sub>Se<sub>3</sub>, and In<sub>2</sub>Te<sub>3</sub>, we proceeded to investigate the synthesis of the following ternary compounds based on the reactions:



#### 1. Preparation of Ternary Compounds by Chemical Vapor Transport

Chemical vapor transport (CVT) is a useful technique for materials that have a high melting point, dissociate at the melting point, or melt under elevated pressures. By using CVT, lower temperatures can be used since the volatile intermediate phases have higher vapor pressures relative to the material of interest. In addition, this method allows separation of phases, since the solid condenses within the section of the container that is at the proper temperature. Compounds that melt incongruently (i.e., with decomposition) can also be synthesized since the growth takes place at temperatures below the melting point of the compound. Many of the defect chalcopyrites of the type  $\text{A}^{\text{II}}\text{B}_2^{\text{III}}\text{C}_4^{\text{VI}}$  fall into this category.

The mass transport rate for this process is a function of:

- Tube geometry. Increasing the cross section of the tube increases the rate (which is controlled by thermal convective processes); increasing the length of the tube slows down the rate of transport.

- The concentration of the transport. At low concentrations, the rate is slow. As the concentration is increased, the rate increases, slowly at first and then more rapidly.
  - The average temperature and the temperature difference ( $\Delta T$ ) between the source material and the growing crystal. The temperature difference will be of minor importance when thermal convective processes are dominant. Higher temperatures increase both vapor concentration and convection, as discussed above. A greater thermal differential increases the transport rate since vapor pressure will tend to equilibrate to the temperature at the source, while condensation occurs in the cooler zone.
- a. Iodine as Transport Medium

Initial results in vapor transport reaction, using II-VI and III-VI binary compounds as starting materials followed by the addition of iodine into the ampoule, were not universally successful (as reported in the literature<sup>3</sup>) in forming the desired ternary compound (i.e.,  $A^{II}B_2^{III}C_4^{IV}$ ) or even in completely transporting material to form an ingot (as previously described). Those compounds that had not previously yielded usable samples for evaluation (either by reaction and recrystallization in situ or by vapor transport) were repeated using  $CdI_2$  and  $ZnI_2$  as starting materials. In these cases, iodine is still the transport medium, but advantages are gained by (1) minimizing the loss of the very volatile elemental iodine in the preparation stages and (2) having constituent elements in a more volatile form, e.g., the iodide, which yields a highly reactive metal atom on decomposition.

(1)  $ZnIn_2S_4$  and  $CdIn_2S_4$  - The CVT method using iodine as the transport medium initially was used to grow  $ZnIn_2S_4$  and  $CdIn_2S_4$ ; this technique has been described in the literature.<sup>3</sup> Two tube sizes were used for growing these compounds: each had a 1-cm i.d., but one was 20 cm long and the other was 33 cm long. The 20-cm tubes were pulled through a sloping temperature gradient, while the 33-cm tubes were placed in a thermal gradient and remained stationary. A sloping gradient is

useful along the crystallization tube to find the optimal temperature for crystal deposition. The tubes, which contained ~25 g of crystal source material, were loaded with iodine in various amounts and sealed off under vacuum. To prevent the iodine from subliming during evacuation, the tube was immersed in liquid nitrogen.

Five runs were made to grow  $\text{ZnIn}_2\text{S}_4$ . Three of the runs consisted of pulling the tube through the temperature gradient from  $930^\circ\text{C}$  to  $700^\circ\text{C}$  at a speed of 2 mm/hr. In the first of these, the tube exploded; in the remaining two, the runs were completed without incident. The other two runs of the five were done in situ. In those two runs, the tubes were loaded as before with equal molar amounts of  $\text{ZnS}$  and  $\text{In}_2\text{S}_3$ , iodine was introduced, and the tube was evacuated and sealed. These tubes were placed in a temperature gradient of  $1000^\circ\text{C}$  to  $700^\circ\text{C}$ . The growth time for each was ~150 hr. The concentration of iodine ranged from 0.6 to  $6 \text{ mg/cm}^3$  of tube volume.

In all cases described above, there was insignificant transport. We identified  $\text{Zn}_3\text{In}_2\text{S}_6$  by X-ray analysis (Figure 14) as the resulting compound that dominated in all the runs. A small amount of transported material was identified as being  $\text{ZnIn}_2\text{S}_4$  (Figure 15). The bulk of the material sintered and underwent grain growth; this was identified as being primarily  $\text{Zn}_3\text{In}_2\text{S}_6$ .

Equal molar amounts of  $\text{CdS}$  and  $\text{In}_2\text{S}_3$  along with iodine equivalent to  $6 \text{ mg/cm}^3$  of tube volume were sealed under vacuum into a 33-cm tube. This tube was placed in a temperature gradient of  $1000^\circ\text{C}$  to  $700^\circ\text{C}$ . After 150 hr, no significant transport had taken place. The material sintered and underwent grain growth. X-ray diffraction analysis was used to identify it as  $\text{CdIn}_2\text{S}_4$  (Figure 16). A 1 cm x 2 mm sample has been cut for measurements.

The reason for the lack of transport in the above experiments is not obvious. The tubes were of sufficient diameter and not too long; the sizes are comparable to the sizes reported in the literature. Also, tubes of this size had been used on numerous occasions in this laboratory to grow binary compounds by CVT techniques. The concentration of iodine is sufficient without getting into the dangerous situation of

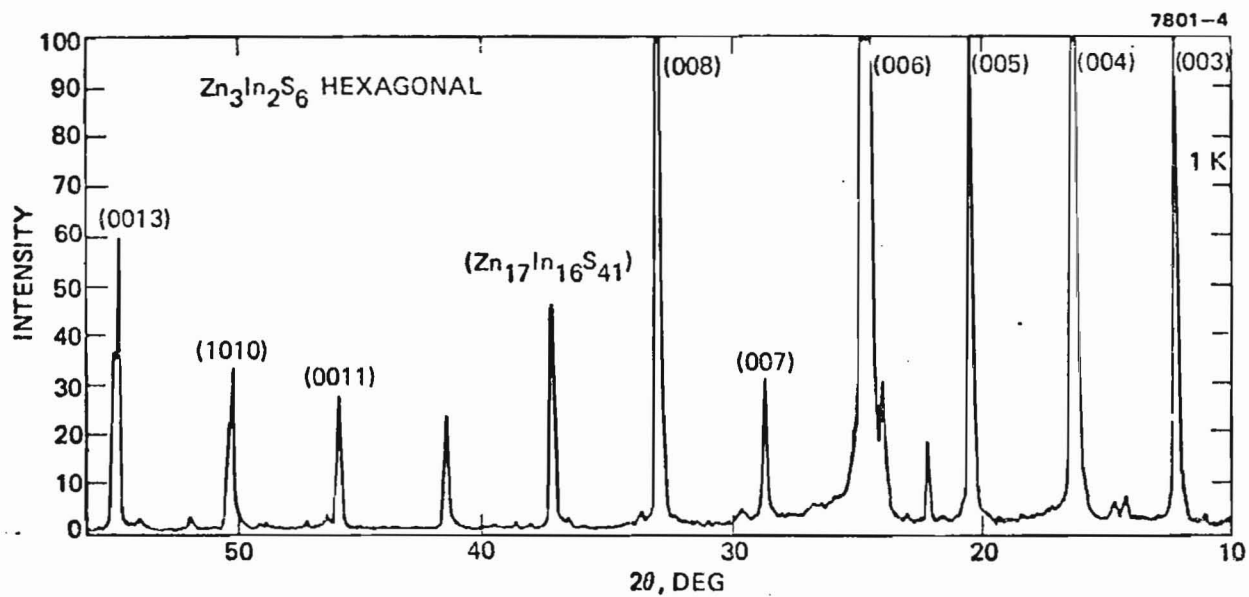
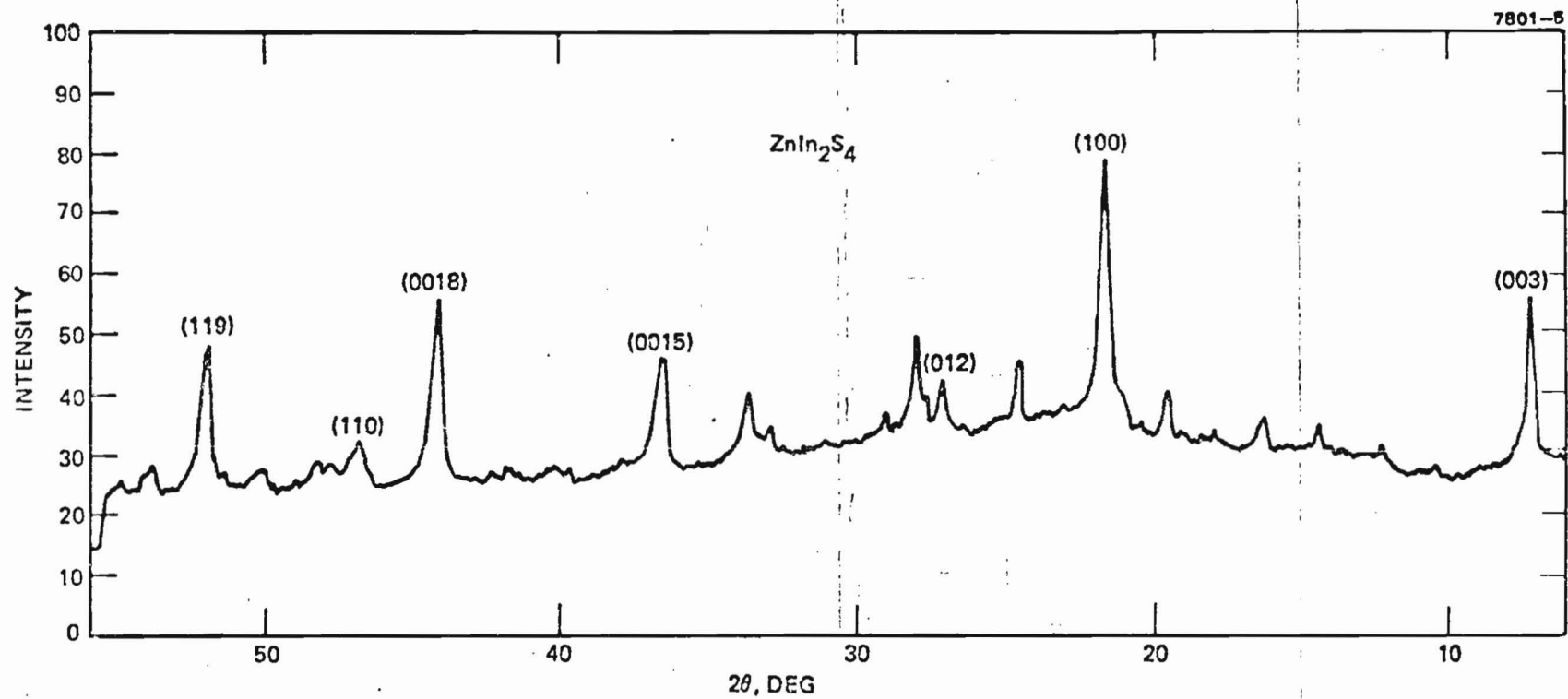


Figure 14. X-ray diffraction pattern of  $Zn_3In_2S_6$ .



32

Figure 15. X-ray diffraction pattern of  $\text{ZnIn}_2\text{S}_4$ .



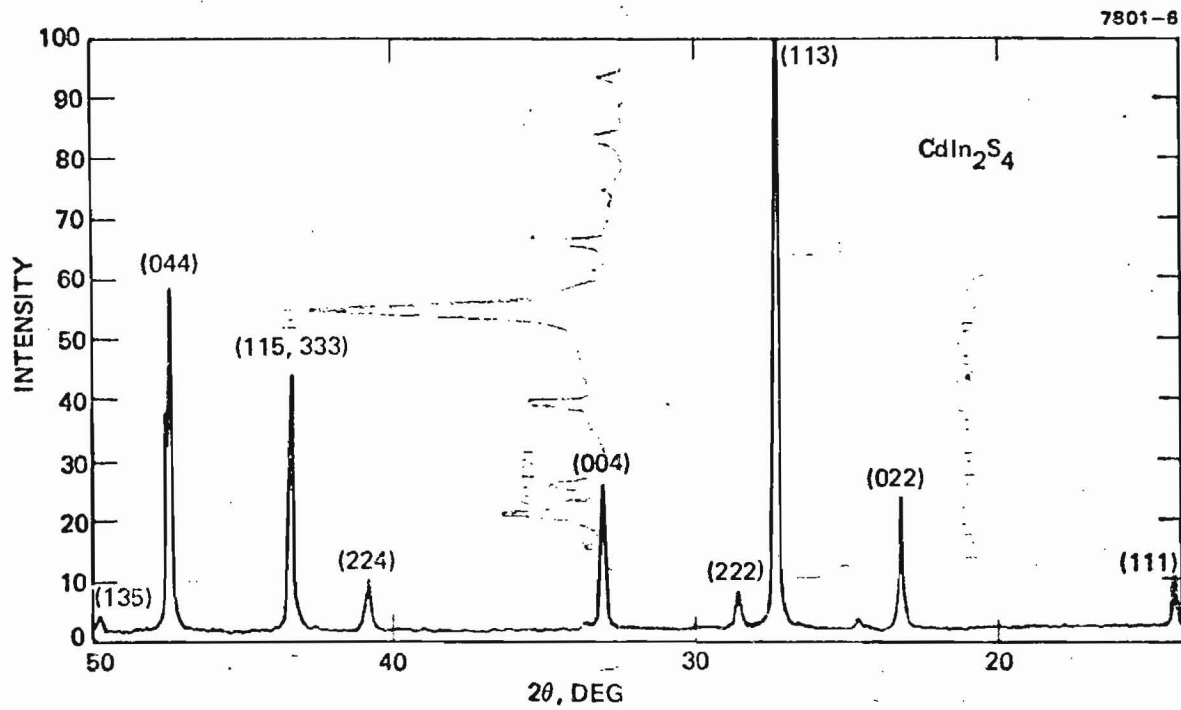


Figure 16. X-ray diffraction pattern of  $\text{CdIn}_2\text{S}_4$ .

pressure buildup. The temperature difference ( $\Delta T$ ) is large enough for transport even though it may not be operative since convective processes may be dominant. The length of time in the furnace was certainly adequate for transfer to occur.

This procedure was followed, to synthesize  $\text{CdIn}_2\text{S}_4$ ,  $\text{CdIn}_2\text{Se}_4$ , and  $\text{ZnIn}_2\text{S}_4$ , using 1-cm-diameter ampoules and calculating iodine concentration to obtain 1 atm of iodine at the run temperature; stoichiometry was balanced using appropriate II-VI binary compounds. Runs typically were carried out around  $1000^\circ\text{C}$  at the source with a large thermal gradient on the order of  $400^\circ\text{C}$ .

Successful results in transporting and forming  $\text{CdIn}_2\text{Se}_4$  were obtained; the compound was identified by X-ray analysis (Figure 17). A small amount of  $\text{ZnS} + \text{In}_2\text{S}_3$  transported, but not enough for identification. No transport of constituents was observed in the  $\text{CdIn}_2\text{S}_4$  experiment.

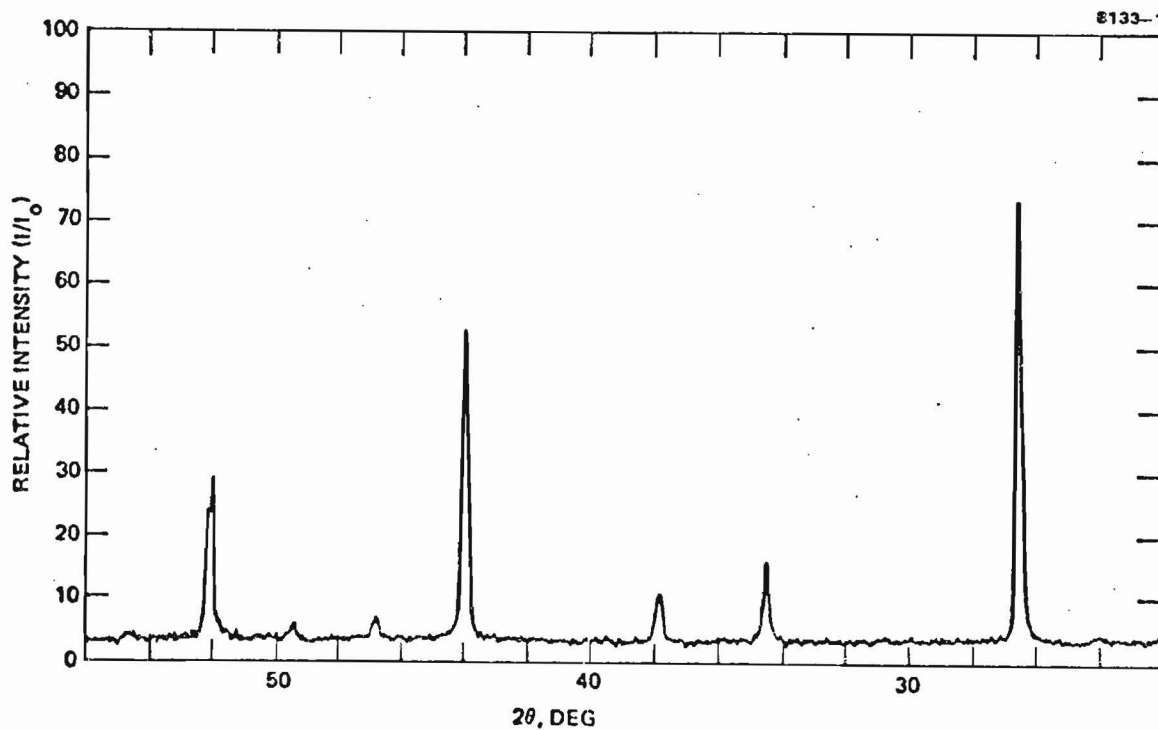


Figure 17. X-ray diffraction pattern of  $\text{CdIn}_2\text{Se}_4$ .

## b. HCl as Transport Medium

Early observations of little or no transport using iodine as a carrier gas led to the search for a more efficient carrier. Based on optimistic reports in the literature, we selected HCl for this carrier gas. Special equipment for loading this corrosive gas into the ampoule had to be acquired. The only additional significant change in these runs was to increase the tube diameter from 1 cm to 2 cm in accordance with theories that the transport rate increases exponentially with increased ampoule diameter (as discussed above). Using HCl as the transport medium at a pressure calculated to be 1 atm at run temperature,  $\text{CdIn}_2\text{S}_4$  was prepared and confirmed by X-ray diffraction analysis.

Initial runs using HCl for the preparation of  $\text{ZnIn}_2\text{S}_4$  indicated that there was a substantial amount of the desired ternary compound present as well as  $\text{Zn}_9\text{In}_8\text{S}_{21}$  and  $\text{Zn}_3\text{In}_2\text{S}_6$ . A ternary compound close to  $\text{CdGa}_2\text{S}_4$ , as identified by X-ray analysis, was also formed by HCl vapor transport reactions. Some free  $\text{Ga}_2\text{S}_3$  (a volatile component) was collected from the run and identified. In addition, the formation of  $\text{CdGa}_2\text{Se}_4$  from its binary constituents ( $\text{CdSe}$  and  $\text{Ga}_2\text{Se}_3$ ) was accomplished using this procedure.

The results of all vapor transport reaction studies are summarized in Table 2.

(1)  $\text{ZnGa}_2\text{S}_4$  and  $\text{CdGa}_2\text{Se}_4$  Synthesis Using HCl as Transport Medium -- In the case of  $\text{ZnGa}_2\text{S}_4$ , all starting material was transported to the conical end of the sealed ampoule at temperatures as high as  $1100^\circ\text{C}$ . The ampoule contained three distinct bands: yellow, white, and translucent. Initial DTA investigation of  $\text{ZnGa}_2\text{S}_4$  indicated a melting point in excess of  $2100^\circ\text{C}$  (limit of current DTA apparatus) and a possible phase transition above  $1000^\circ\text{C}$ . Attempts at single-crystal growth by vapor were not successful.

The sample of  $\text{CdGa}_2\text{Se}_4$  showed almost no transport, yielding only a thin coating showing two different colors. The temperature in the hot zone was  $900^\circ\text{C}$ ; 1 atm of HCl was maintained at the operating temperature.

Results indicated the need for an increased temperature ( $1000^\circ\text{C}$  appears useful) and for an increased pressure of HCl at operating

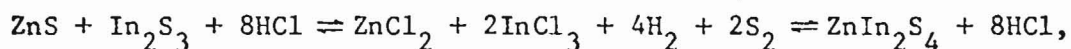
Table 2. Vapor Transport Reaction Studies

Desired Compound	Starting Materials	Temperature Range, °C	Carrier	Tube Diameter, cm	Amount of Source Left	Transport	X-Ray	Remarks
$\text{CdIn}_2\text{Se}_4$	$\text{CdSe} + \text{In}_2\text{Se}_3$	990 to 550	$\text{I}_2$	1	None	Yes	Yes	Two sections of tube coated: yellow crystalline in high temperature section; red, yellow, white coatings in low temperature region.
$\text{CdIn}_2\text{S}_4$	$\text{CdS} + \text{In}_2\text{S}_3$	990 to 550	$\text{I}_2$	1	All	No	—	
$\text{ZnIn}_2\text{S}_4$	$\text{ZnS} + \text{In}_2\text{S}_3$	990 to 550	$\text{I}_2$	1	Much	Little	—	
$\text{ZnIn}_2\text{S}_4$	$\text{ZnS} + \text{In}_2\text{S}_3$	1010 to 625	HCl	2	Much	Yes	Yes (Black)	Also $\text{Zn}_9\text{In}_8\text{S}_{21}$ and $\text{Zn}_3\text{In}_4\text{S}_6$
$\text{CdIn}_2\text{S}_4$	$\text{CdS} + \text{In}_2\text{S}_3$	1010 to 625	HCl	2	Some	Yes	Yes (Black)	
$\text{CdIn}_2\text{S}_4$	$\text{CdS} + \text{Ga}_2\text{S}_3$	650	HCl	2	Much	Yes	Yes	Close to $\text{CdGa}_2\text{S}_4$ , some free $\text{Ga}_2\text{S}_3$
$\text{CdIn}_2\text{Se}_4$	$\text{CdSe} + \text{Ga}_2\text{Se}_3$	900	HCl	2	Much	Yes	Yes	

temperatures. A review of recent crystal growth literature uncovered a report of the use of 2 to 3 atm pressure of HCl under operating conditions for a successful yield of ternary chalcogenide crystals by vapor transport.

(2) Preparation of ZnIn<sub>2</sub>S<sub>4</sub> and CdIn<sub>2</sub>S<sub>4</sub> — For the preparation of ZnIn<sub>2</sub>S<sub>4</sub>, the starting materials were the respective compounds encapsulated in a silica tube with 380 mm HCl at ~25°C. To clean its tip, the tube was placed vertically in a hot furnace for one day so that the collection end of the tube was hotter than the source end. The temperature was then reversed, and the tube was pulled slowly (0.8 mm/hr) through the temperature profile until it was several centimeters out of the furnace. For the zinc compound, the maximum temperature was 1000°C and the "growth" time was 18 days; for the cadmium compound, the maximum temperature was 960°C and the "growth" time was 19 days. After the run, the tube was air quenched to room temperature.

In previous runs with HCl, the pressure of HCl was calculated to give 1 atm of pressure at the operating temperature. These runs were filled with 380 mm HCl at room temperature. The HCl pressure was ~2 atm for each run at maximum temperature. The increase in HCl pressure was suggested by results from our previous runs, in which the amount of material transported had been relatively low. An inspection of the reaction equations,



indicated that the reaction is pressure dependent, and that it may be possible to increase the amount of transported material by increasing the pressure. This was later verified. The material was submitted for X-ray analysis. The compound CdIn<sub>2</sub>S<sub>4</sub> was identified by X-ray powder diffraction analysis. The pattern is shown in Figure 18.

#### c. Crystal Growth of ZnIn<sub>2</sub>S<sub>4</sub>

Experiments to synthesize ZnIn<sub>2</sub>S<sub>4</sub> were conducted once again using iodine as the transport medium. The amount of reaction and transport increased significantly in runs lasting a few days as

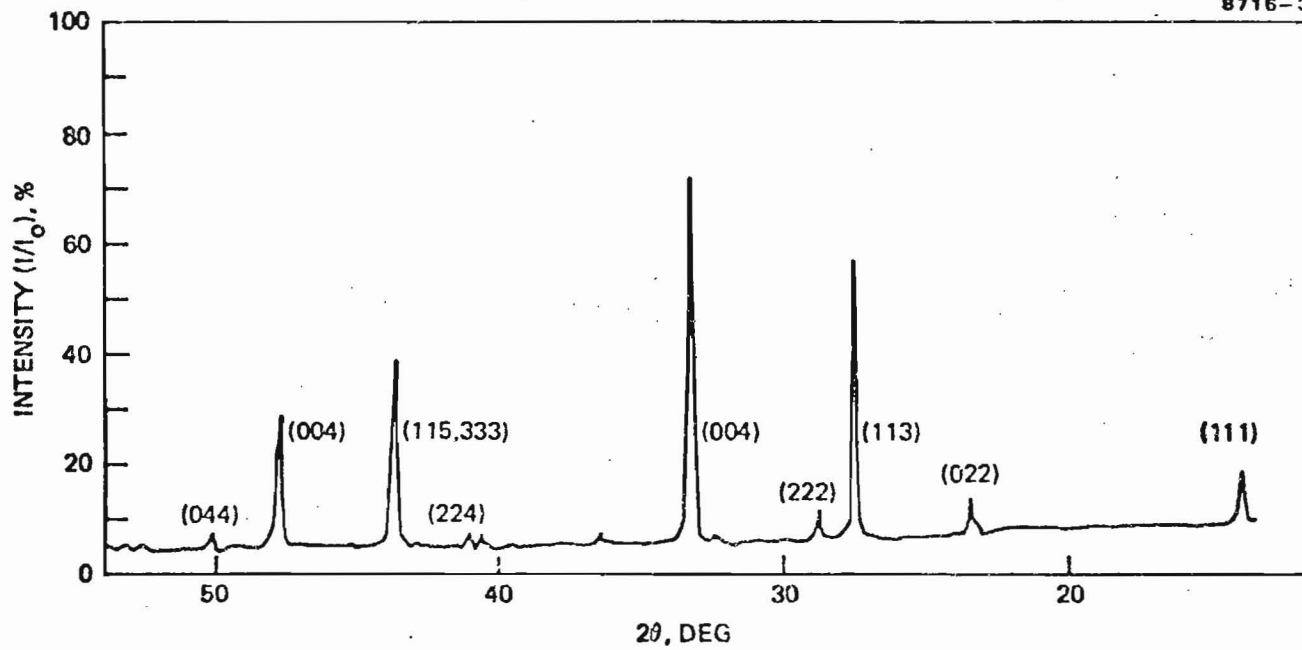


Figure 18. X-ray diffraction pattern of CdIn<sub>2</sub>S<sub>4</sub>.

compared to previous runs (using HCl) lasting several weeks. The transported material contained several compounds of  $Zn_x In_y S_x$  of varying stoichiometry; all were rich in  $In_2S_3$ , and some free ZnS was identified as well by X-ray powder diffraction techniques. In subsequent runs, the iodine transport technique combined with addition of excess  $In_2S_3$  (~2%) yielded high-quality platelets of  $ZnIn_2S_4$ . The yellow mica-like platelets were identified to be  $ZnIn_2S_4$  by X-ray diffraction. Some small (mm edge) crystals were also obtained.

## 2. Synthesis from Solution

### a. $CdIn_2Te_4$

Primary emphasis was placed on the crystal growth of single-crystal  $CdIn_2Te_4$ , a compound that we earlier had observed as having a high value for the low-frequency dielectric constant from solution. Using the solid-liquid relationships shown (Figure 19) in the pseudo-binary phase diagram  $CdTe-In_2Te_3$  as published<sup>6</sup> in the literature, we attempted to grow single-crystal material. Melt compositions were selected lying in the composition range covered by the line a-b. In this region, solid  $CdIn_2Te_4$  ( $\beta \equiv$  solid  $CdIn_2Te_4$ ) is in equilibrium with liquid (richer in  $In_2Te_3$ ) in the temperature range 785°C to 702°C. By selecting a starting composition close to "a," crystals of pure  $CdIn_2Te_4$  can be grown by lowering the temperature. Below 702°C, however, additional phases begin to solidify and cause a multiphase polycrystalline region to begin to grow, thus preventing further single-crystal growth.

Several runs were made utilizing the conditions discussed above to grow single-crystal  $CdIn_2Te_4$ . Fused ~16-mm-diameter quartz crucibles with conical bottoms were used to nucleate single-crystal growth. The sealed, evacuated ampoules were processed in a vertical two-zone Bridgman-like furnace. The ampoule was rotated, and vibrational stirring was applied during the growth cycle. Several ingots were produced in which the lower (conical-shaped) sections were single phase and, in one case, single-crystal  $CdIn_2Te_4$ ; the upper parts, as anticipated, were multiphase and polycrystalline. The compound  $CdIn_2Te_4$  was identified

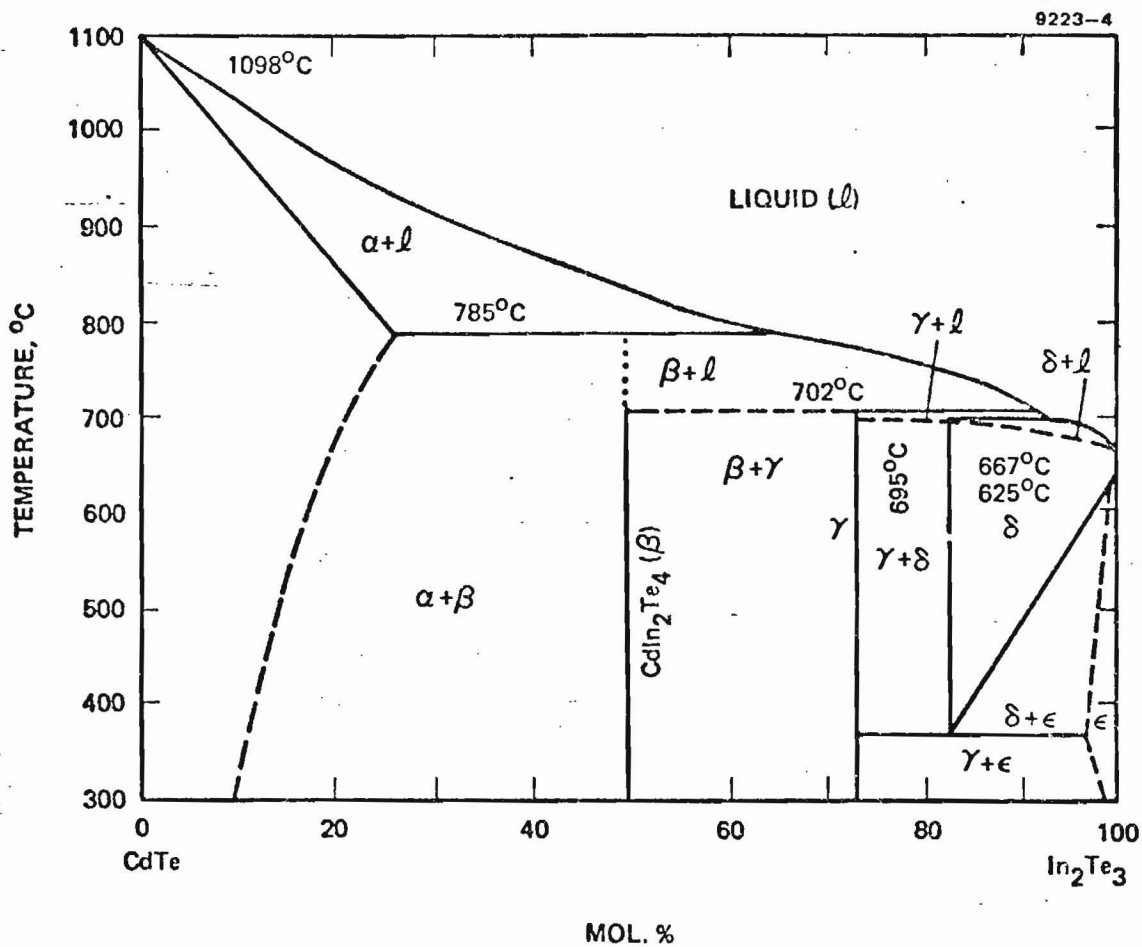


Figure 19. Phase equilibrium diagram for CdTe-In<sub>2</sub>Te<sub>3</sub>.



by X-ray diffraction analysis (Figure 20). Laue photographs showed several slices to be single crystals.

X-ray microprobe analysis of the single-phase material showed insignificant variations in composition from nose to tail with an average composition:

58% Te

29% In

13% Cd.

There are indications from the analysis that the composition is slightly rich in  $\text{In}_2\text{Te}_3$  and that there is some solid solubility between  $\text{CdIn}_2\text{Te}_4$  and  $\text{In}_2\text{Te}_3$ . However, our results indicate that the solid solubility line between the regions is more vertical than that reported in Ref. 6 (dashed line in Figure 19) and probably closer to the vertical (dotted) line in Figure 19.

The single-crystal section (cone-shaped) and the final multiphase section are shown in Figure 21. The boundary between the sections is noted. The tip of the cone appears as-grown and indicates a poor start with nucleation getting underway on an apparent gas void, resulting in a concave interface observed during crystallization. That the crystal grew single under these conditions (see Figure 22, an SEM photograph of the as-grown tip) is confirmed by the growth patterns shown in Figure 22 as well as by Laue photography (as previously indicated).

#### D. SYNTHESIS OF $\text{A}_2\text{B}^{\text{I}}\text{C}_3^{\text{IV,VI}}$ COMPOUNDS

A polycrystalline ingot of  $\text{Cu}_2\text{GeS}_3$  was obtained by quenching a melt of that composition. X-ray diffraction indicated the presence of at least one additional phase. Table 3 shows a compilation of lattice parameters of  $\text{A}_2\text{B}^{\text{I}}\text{C}_3^{\text{IV,VI}}$  compounds with literature references (compiled by A. Borshchevsky<sup>7</sup> of Stanford University) and indicates the existence of solid phase transitions and a variety of opinions on crystal class of the low-temperature form. Both the ingot and the starting powder were annealed. After annealing, no changes were observed in the powder. Published phase diagrams indicate that this compound is a peritectic and can be grown from a  $\text{GeS}_2$ -rich melt. An X-ray diffraction pattern for

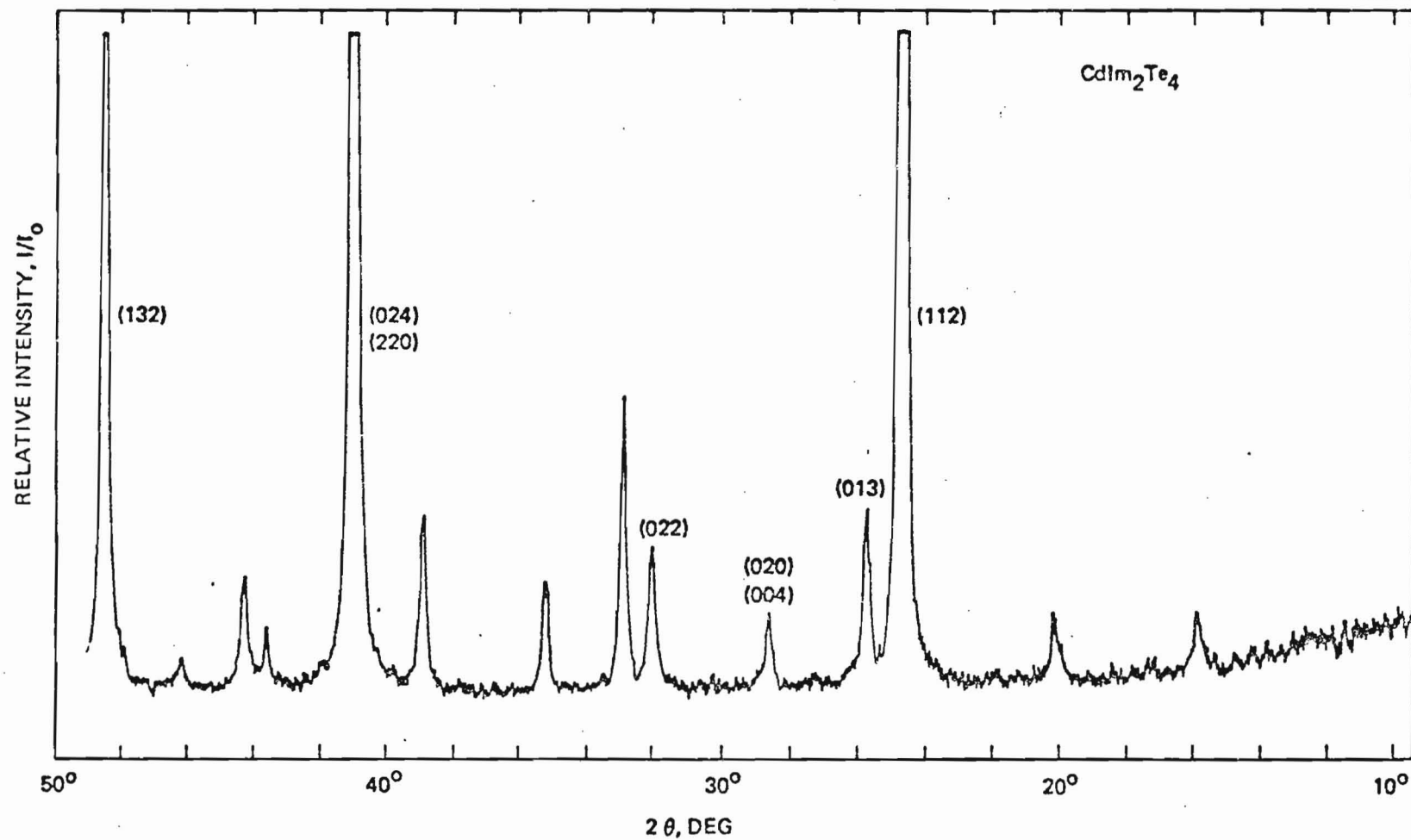


Figure 20. X-ray diffraction pattern of  $CdIn_2Te_4$ .

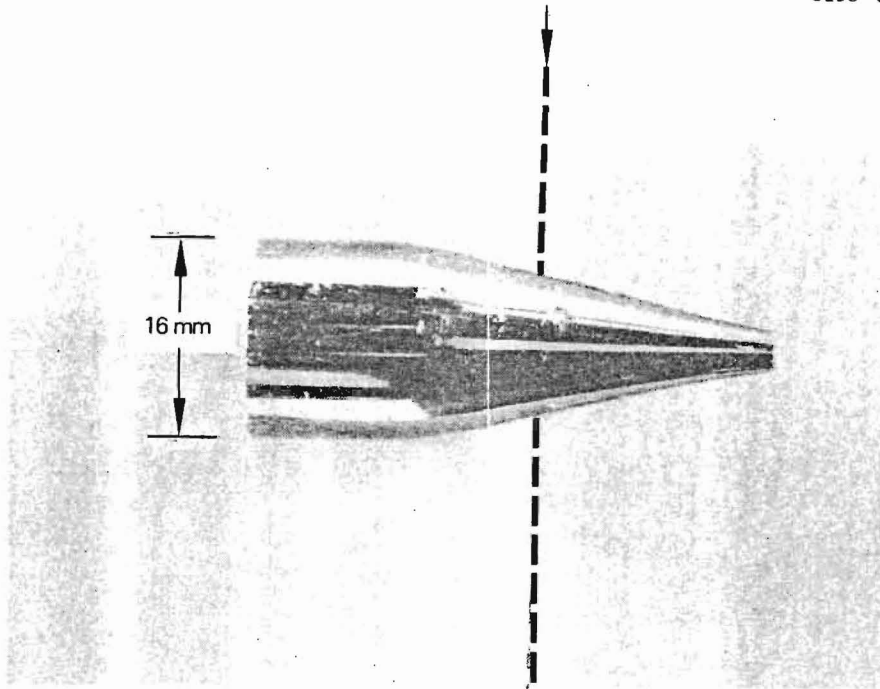


Figure 21. Ingot containing single-crystal CdIn<sub>2</sub>Te<sub>4</sub>.  
(Region to right of dashed line is single.)

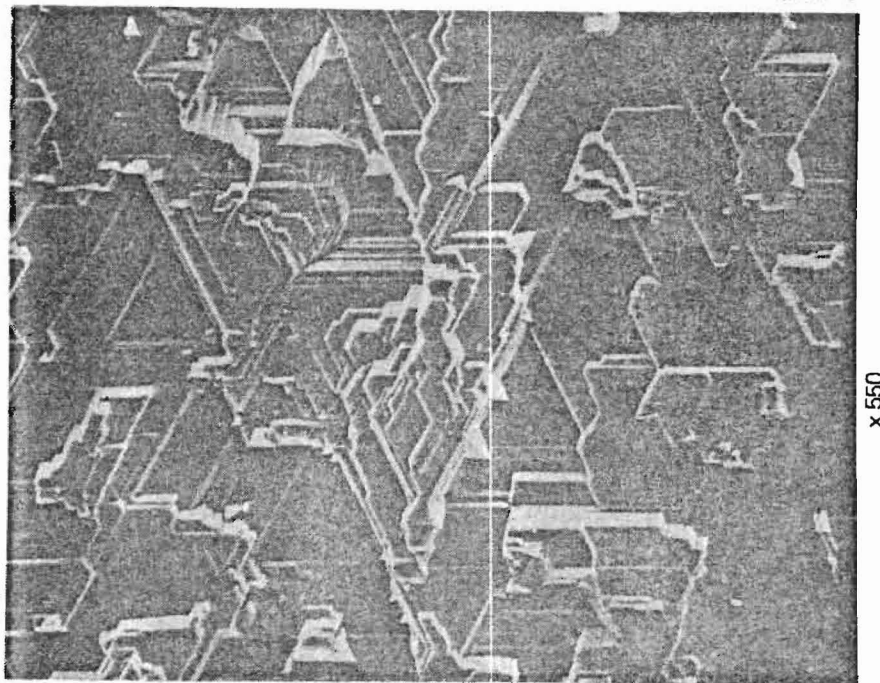


Figure 22. SEM photograph of tip of CdIn<sub>2</sub>Te<sub>4</sub>.

Table 3. Lattice Parameters of  $I_2IV VI_3$  Compounds

Compound	Crystal System	a, Å	b, Å	c, Å	$\beta$ , deg	Reference
$Cu_2SiS_3$ (H.T.)	Hex	3.684		6.044		8
$Cu_2SiS_3$ (L.T.)	Tetr	5.290		5.078		8
	Ortho	11.21	12.04	6.03		9
	Mono	11.51	5.34	8.16	98.95	9
	Ortho	10.981	6.416	6.046		10
$Cu_2SiSe_3$	Mono	12.10	5.62	8.61	99	9
$Cu_2SiTe_3$	Mono	12.86	6.07	9.05	99	9
	Cubic	5.93				8
$Cu_2GeS_3$ (H.T.)	Cubic	5.317				8
$Cu_2GeS_3$ (L.T.)	Tetr	5.326	5.219			8
	Tetr	5.320	10.41			9
	Ortho	11.321	3.766	5.21		10
	Cubic	5.30				11
	Mono	6.433	11.300	7.533	125.17	12
	Mono	7.464	22.38	10.64	91.17	13
$Cu_2GeSe_3$	Tetr	5.595	5.482			8
	Tetr	5.590	10.97			9
	Ortho	5.591	5.562	5.488		14
	Cubic	5.55				11
	Tetr	5.591	5.485			15
	Ortho	11.860	3.960	5.485		10
$Cu_2GeTe_3$	Tetr	5.956	5.926			8
	Tetr	5.916	11.85			9
	Cubic	5.95				11
$Cu_2SnS_3$	Cubic	5.445				8
	Tetr	5.426	10.88			9
	Cubic	5.43				11
$Cu_2SnSe_3$	Cubic	5.696				8
	Tetr	5.689	11.37			9
	Cubic	5.68				11
	Cubic	5.6877				15
$Cu_2SnTe_3$	Cubic	6.047				8
	Tetr	6.048	12.11			9
	Cubic	6.04				11

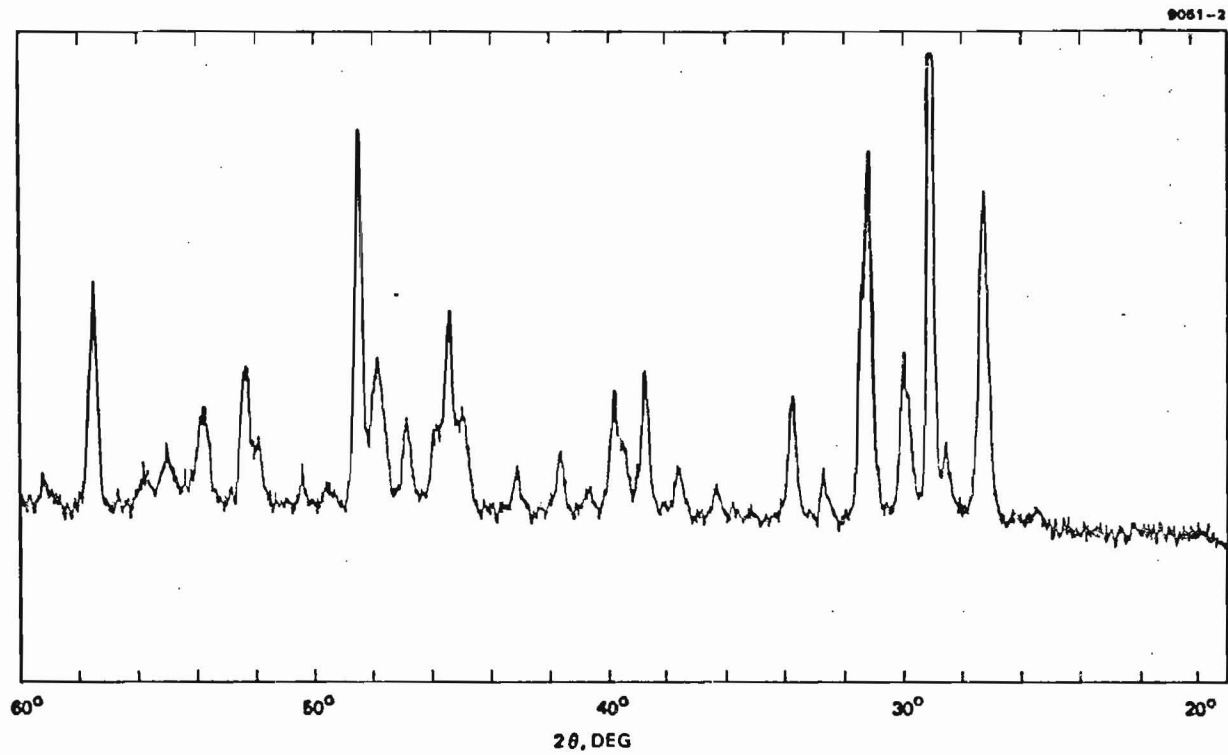
7209

$\text{Cu}_2\text{GeS}_3$  (Figure 23) shows the X-ray diffraction pattern of the high-temperature distorted-cubic phase quenched from the melt (Figure 23(a)); the annealed powder pattern (450°C for 500 hr) is shown in Figure 23(b). The phase transition is reported to be at 670°C. Although there is a slight difference in the patterns, we have not observed any definite evidence of a low-temperature phase.

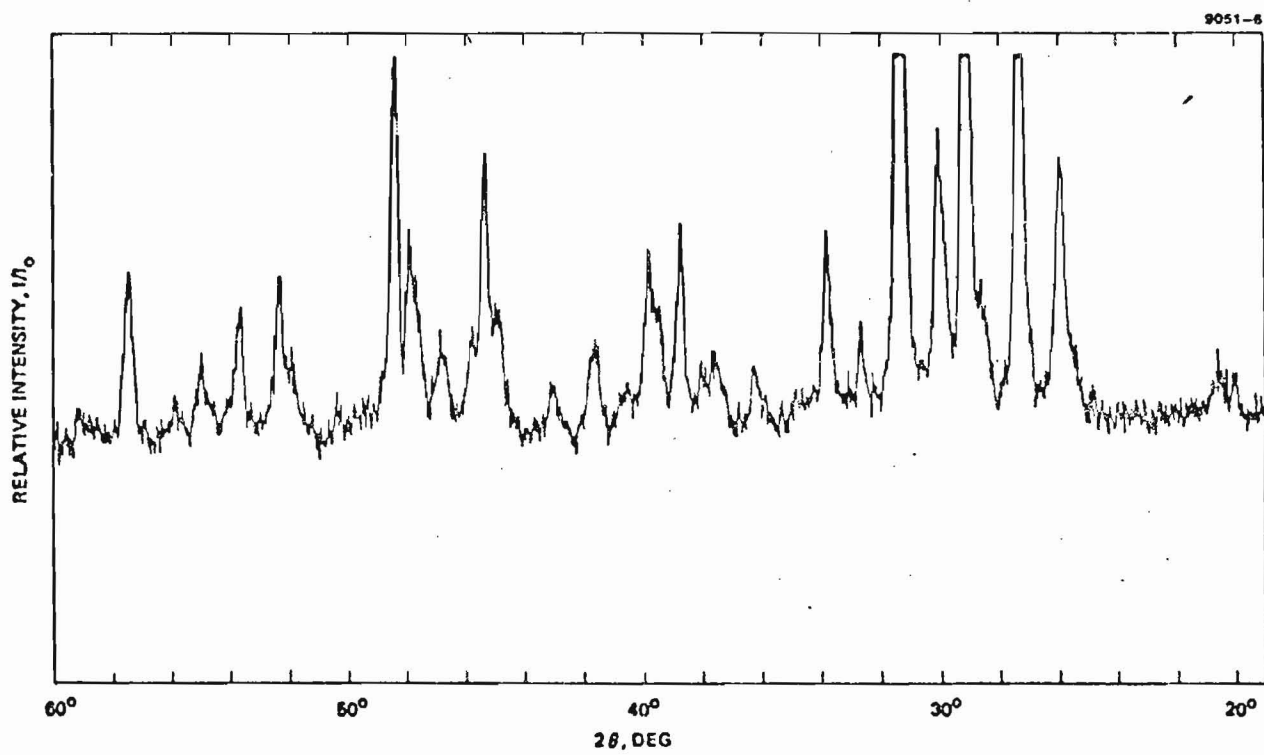
The structure of  $\text{Cu}_2\text{GeTe}_3$  as indicated by X-ray diffraction analysis appears to be cubic with  $a = 5.95 \pm 0.02 \text{ \AA}$ . No evidence of the reported tetragonal phase is indicated in the X-ray diffraction patterns (Figure 24) for as-grown and annealed (450°C for 500 hr) samples. However, differential thermal analysis (DTA) indicates the existence of a solid phase transformation (exact temperature undetermined) and a congruent melting compound at 490°C. The material contains a small amount of a second phase both before and after annealing. Although the literature (see Table 3) is not precise on that matter, there are reports of the observation of a tetragonal phase. Additional DTA work is required if the compound appears interesting (i.e., has a high dielectric constant).

#### E. QUARternary COMPOUNDS: $\text{Cu}_2\text{CdGeTe}_4$

As-grown and annealed samples of the reported quaternary compounds ( $\text{Cu}_2\text{CdGeTe}_4$ ) both show by X-ray diffraction analysis (Figure 25) free CdTe. The annealed sample (450°C for 500 hr) shows (Figure 25(b)) reduced CdTe peaks and a shift (change in lattice parameters) from the as-grown sample (Figure 25(a)), which may indicate that continued annealing will yield the quaternary from a composition that looks (as-synthesized, Figure 25(a)) like the ternary  $\text{Cu}_2\text{GeTe}_3$  plus CdTe. The presence of additional phases in the material also was observed both before and after annealing; perhaps this indicates two additional phases plus CdTe. DTA data showed at least three phase transformations: 786, 523, and 513°C.



(a) As-grown sample



(b) After annealing

Figure 23. X-ray diffraction pattern of  $\text{Cu}_2\text{GeS}_3$ .

9051-3

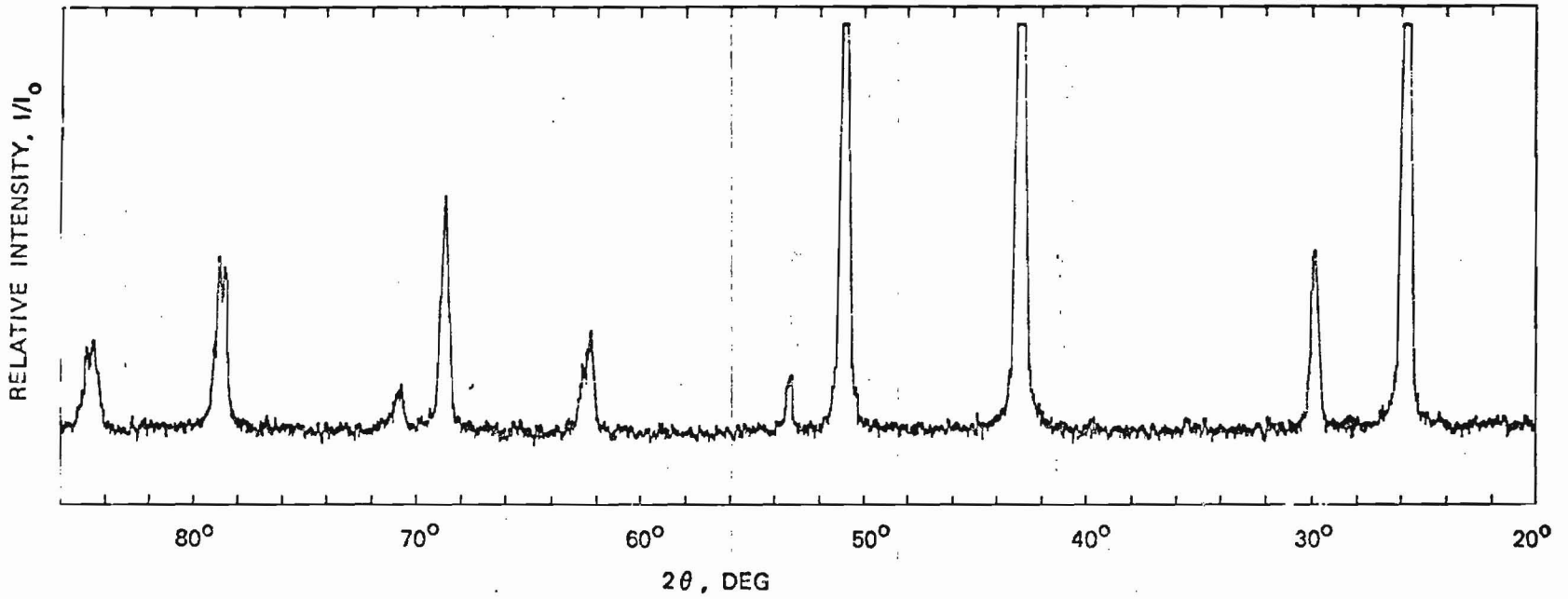
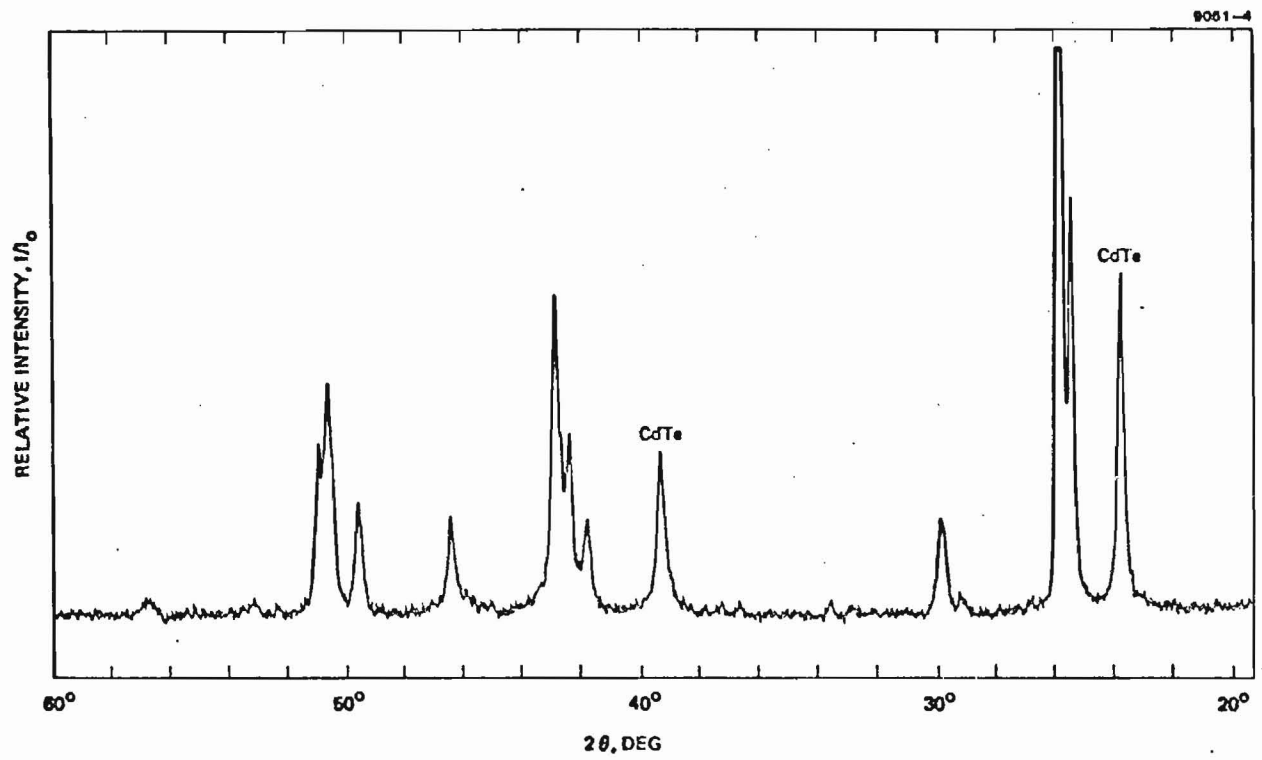
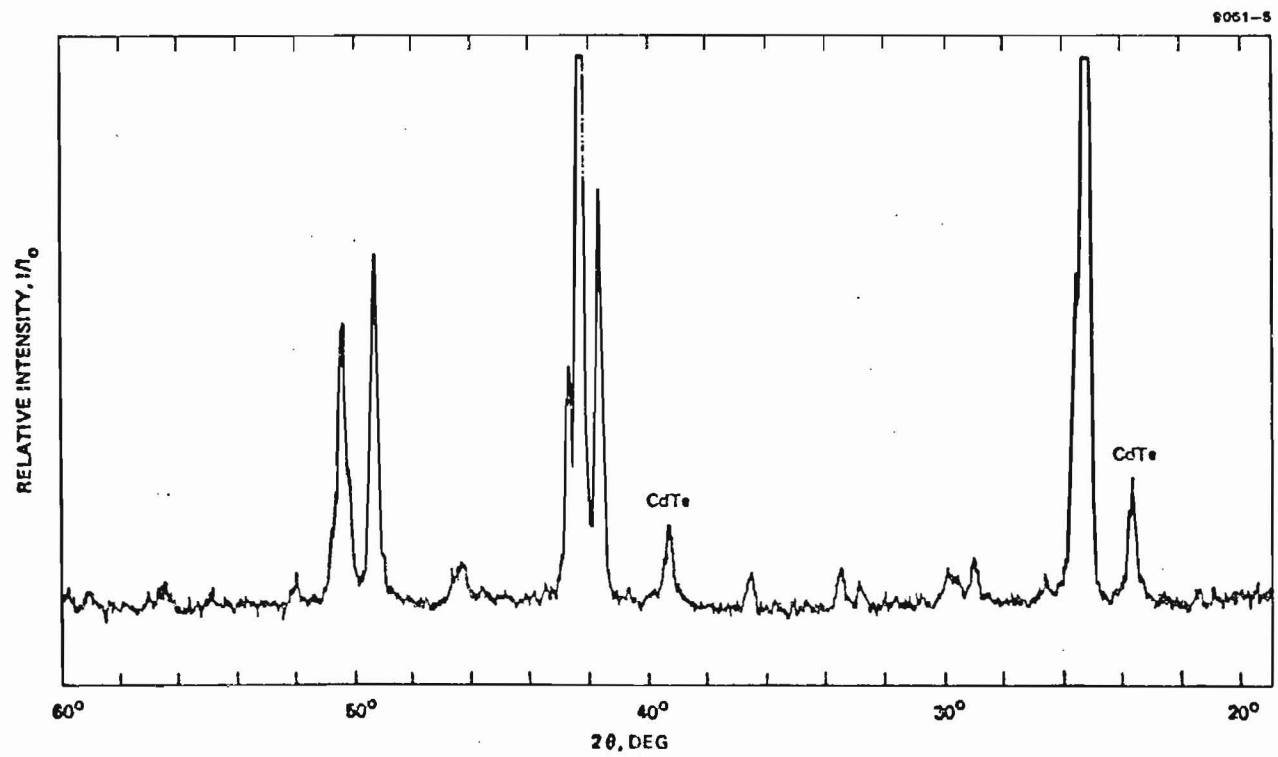


Figure 24. X-ray diffraction pattern of cubic  $\text{Cu}_2\text{GeTe}_3$ .



(a) As-grown sample



(b) After annealing

Figure 25. X-ray diffraction pattern of  $\text{Cu}_2\text{CdGeTe}_4$ .



M12680

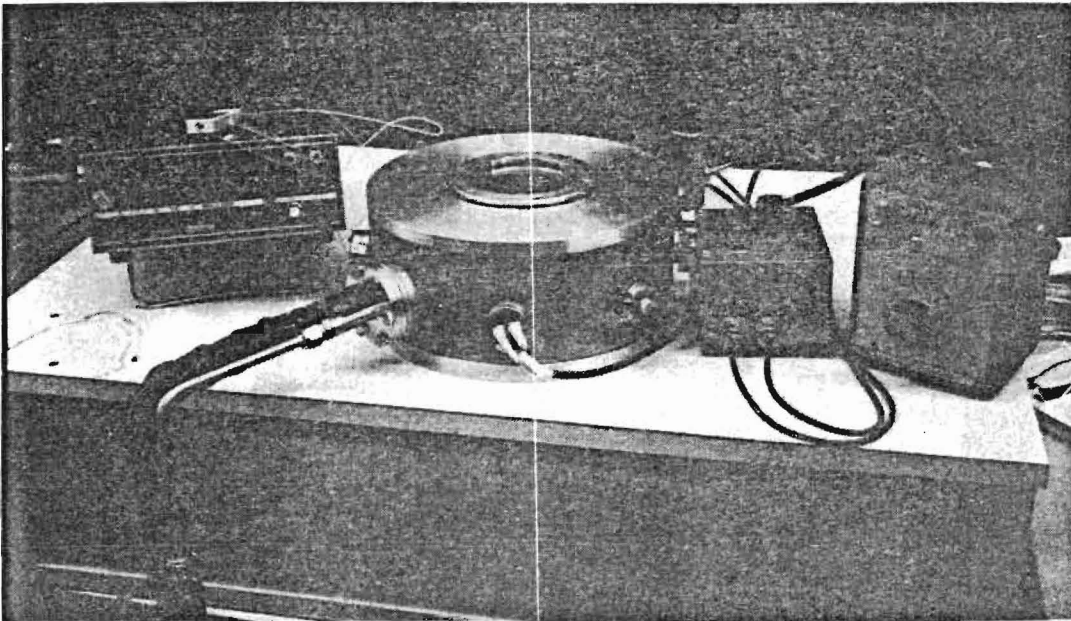


Figure 26. Electrical testing apparatus.

M12678

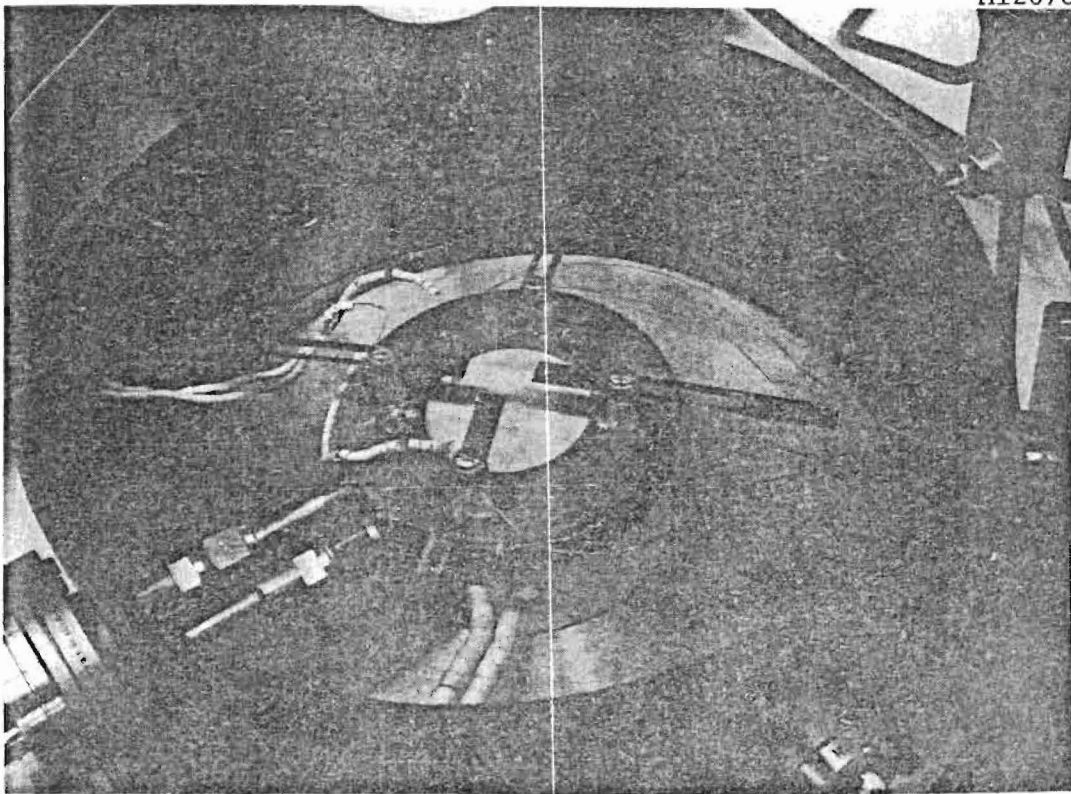


Figure 27. Electrical testing apparatus (internal view).

## SECTION 4

### MATERIALS CHARACTERIZATION

#### A. MEASUREMENT OF DIELECTRIC CONSTANT AND DIELECTRIC RELAXATION

The ability to make accurate capacitance and dielectric relaxation measurements on a new insulating or semi-insulating compound depends markedly on the availability of a good metalization system for electrical contacts. If high Schottky barriers are formed at the metal-contact/insulator interface and the insulator does not have a sufficiently high resistance ( $10^7 \Omega$  or higher), the measured capacitance will be rather high and essentially will represent the Schottky-barrier capacitance. This phenomenon was observed with  $\text{ZnSiAs}_2$  having silver paint electrodes. An absurdly high value ( $\epsilon = 9500$ ) was measured for the dielectric constant. That this was genuinely a Schottky-barrier effect was ascertained by applying a voltage bias to the capacitor and observing the change in capacitance. Although, for any given material, a metal or an alloy system may be found to yield non-barrier-forming contacts, the search for such contacts for the new materials made during this program would represent a major undertaking. Alternatively, if a suitable metal that is also a constituent of the ternary chalcogenide (e.g., In for  $\text{CdIn}_2\text{Se}_4$ ,  $\text{CuInSe}_2$ , and  $\text{AgInSe}_2$ ) is used as the contact and further diffused into the shallow surface layers of the chalcogenide, a graded, nearly Ohmic junction may be expected at the metal-insulator interface. Although this approach has worked well with single crystals (e.g., Ag on  $\text{AgGaS}_2$ ), it has one main drawback with polycrystalline insulators. Even after a moderate diffusion anneal of In in polycrystalline  $\text{CuInSe}_2$ ,  $\text{AgInSe}_2$ , and  $\text{CdIn}_2\text{Se}_4$ , we observed that the samples were essentially shorted or exhibited resistances on the order of a few hundred ohms and therefore could not be measured. We believe that the shorts are caused by diffusion of the metal along grain boundaries and the subsequent formation of conducting filaments across the bulk of the insulator.

As a solution to these problems, we decided that capacitance measurements should be made with two blocking contacts. This also prevents carrier injection. The blocking electrodes consist of two thin (0.004 in.) sheets of Mylar with evaporated silver contacts. The Mylar capacitors have the same area as the test insulator. The insulator is sandwiched between the two Mylar capacitors, and the capacitance  $C_m$  and the equivalent parallel resistance  $R_m$  of the sandwich structure at a frequency  $\omega$  are measured using a Boonton 750C capacitance bridge. The insulator is then removed from the sandwich, and the total capacitance  $C_s$  and shunt resistance  $R_s$  are measured at the same frequency,  $\omega$ . A network analysis of the equivalent circuits for the two cases yields the capacitance  $C_T$  and resistance  $R_T$  of the test insulator (as shown in Appendix A).

The frequency range was from 5 kHz to 100 kHz. These measurements were performed at room temperature using peak test signal levels of 1 to 3 V.

The static dielectric constant  $\epsilon_s$  was obtained from the calculated capacitance (Appendix A) at any given frequency by using the formula:

$$\epsilon_s = \frac{C_T d}{8.85 A} ,$$

where  $d$  is the thickness of the capacitor (in m),  $A$  is the area of coincidence of the electrodes (in  $m^2$ ), and  $C_T$  is the measured capacitance (in pF).

A general-purpose portable electrical test fixture was fabricated for dielectric constant, dissipation, resistivity (using Van der Pauw's four-point probe method),<sup>16</sup> dielectric breakdown, and EO coefficient. Measurements are possible with this apparatus at any temperature from 77°C to 600°C. In addition, the fixture can be evacuated to  $10^{-7}$  Torr. Figures 26 and 27 show some of the salient features of this facility. The measurements made on materials synthesized during this program are summarized in Table 4. Data on dissipation factor ( $\tan \delta$ ) is given in Table 5.

Table 4. Dielectric Constants at Indicated Frequencies for Some Binary and Ternary Chalcogenides

Compound	Dielectric Constant	Frequency, kHz
GeS <sub>2</sub>	10.7	10
GeSe <sub>2</sub>	5.32	6
	5.31	10
	5.30	50
	5.30	100
	5.26	400
	AgGaS <sub>2</sub>	13.7
AgGaTe <sub>2</sub>	200	5
	270	1000
ZnSiAs <sub>2</sub>	34.78	6
	34.65	10
	33.64	100
	32.91	400
ZnGa <sub>2</sub> S <sub>4</sub>	62.1	6
	40.9	10
	35.8	20
	21.3	50
	18.1	100
	13.5	400
	CuInSe <sub>2</sub>	36.81
36.15		10
35.74		100
35.71		400
Cu <sub>2</sub> GeS <sub>3</sub>	49	10
Cu <sub>2</sub> CdGeTe <sub>4</sub>	60.3	10
CdIn <sub>2</sub> Te <sub>4</sub>	264.5	10

7209

Table 5. Dissipation Factor ( $\tan \delta$ )  
for Several Chalcogenide Materials

Material	$\tan \delta$
$\text{ZnGa}_2\text{S}_4$	0.499
$\text{Cu}_2\text{GeS}_3$	0.00028
$\text{Cu}_2\text{CdGeTe}_4$	0.00364
$\text{CdIn}_2\text{Te}_4$	0.00515

7209

Numerous samples were synthesized that could not be measured because their resistivities were too low for our set-up. These included:

$\text{AgInSe}_2$   
 $(\text{Cu}, \text{Ag})\text{GaS}_2$   
 $\text{AgGa}(\text{S}, \text{Se})_2$   
 $\text{AgInTe}_2$   
 $\text{TlSe}$   
 $\text{CdIn}_2\text{S}_4$   
 $\text{Ag}(\text{Ga}, \text{In})\text{S}_2$   
 $\text{Ag}_3\text{AsS}_3$   
 $\text{AnIn}_2\text{Se}_4$  .

Unfortunately, the scope of the program did not allow detailed study of these materials to allow us to control resistivity (e.g., annealing, doping studies). This is discussed in more detail in Section 6. In addition, absorption caused by free carriers precluded far-IR spectroscopy of many of these samples.

## B. DISCUSSION OF RESULTS

Reproducibility of results was checked by measuring two separate samples from the same as-grown ingot at two different low frequencies.

The reproducibility was fairly good. The small sample-to-sample variations noted were probably caused by minor local variations in structure, impurity, or defect concentrations.

### 1. GeS<sub>2</sub>

Figure 28 shows the dielectric constant as a function of frequency in GeS<sub>2</sub>. The change in the dielectric constant is fairly small (10.73 at 5 kHz as compared to 10.52 at 100 kHz). Figure 29 shows the dissipation factor for GeS<sub>2</sub> as a function of test frequency. The curve has some interesting features. Two strong primary peaks are seen at 5.5 and 65. kHz; these are followed by a definite, albeit weaker, secondary peak at 45 kHz. These dielectric relaxation peaks suggest separate, distinct relaxation processes and deserve further investigation.

The data shown in Figures 26 and 27 represents measurements on only one sample. Since the as-grown GeS<sub>2</sub> crystal boule had a small diameter and the crystal tends to cleave easily, we were not able to obtain a large enough sample on which large-area electrodes could be formed. The small-electrode-area sample discussed above had only a small capacitance (a few pF). Because the capacitance of the test capacitor was so low, accurate measurements of the dielectric constant and dissipation factor were very difficult. Larger crystals which would yield larger capacitance ( $\leq 100$  pF) capacitors should be used to check the reproducibility and accuracy of the dielectric constant and the relaxation measurements.

### 2. GeSe<sub>2</sub>

Figure 30 shows the variation of dissipation factor versus frequency of GeSe<sub>2</sub>; the same plot for ZnGa<sub>2</sub>S<sub>4</sub> is shown in Figure 31. In the case of GeSe<sub>2</sub>, two dielectric relaxation peaks corresponding to 8.5 kHz and 70 kHz are observed. The plot for ZnGa<sub>2</sub>S<sub>4</sub> shows only a small peak at 27 kHz. The dielectric constant of ZnGa<sub>2</sub>S<sub>4</sub> is much higher at low frequencies (6 kHz) than similar constants for other materials that we have previously investigated in this project.

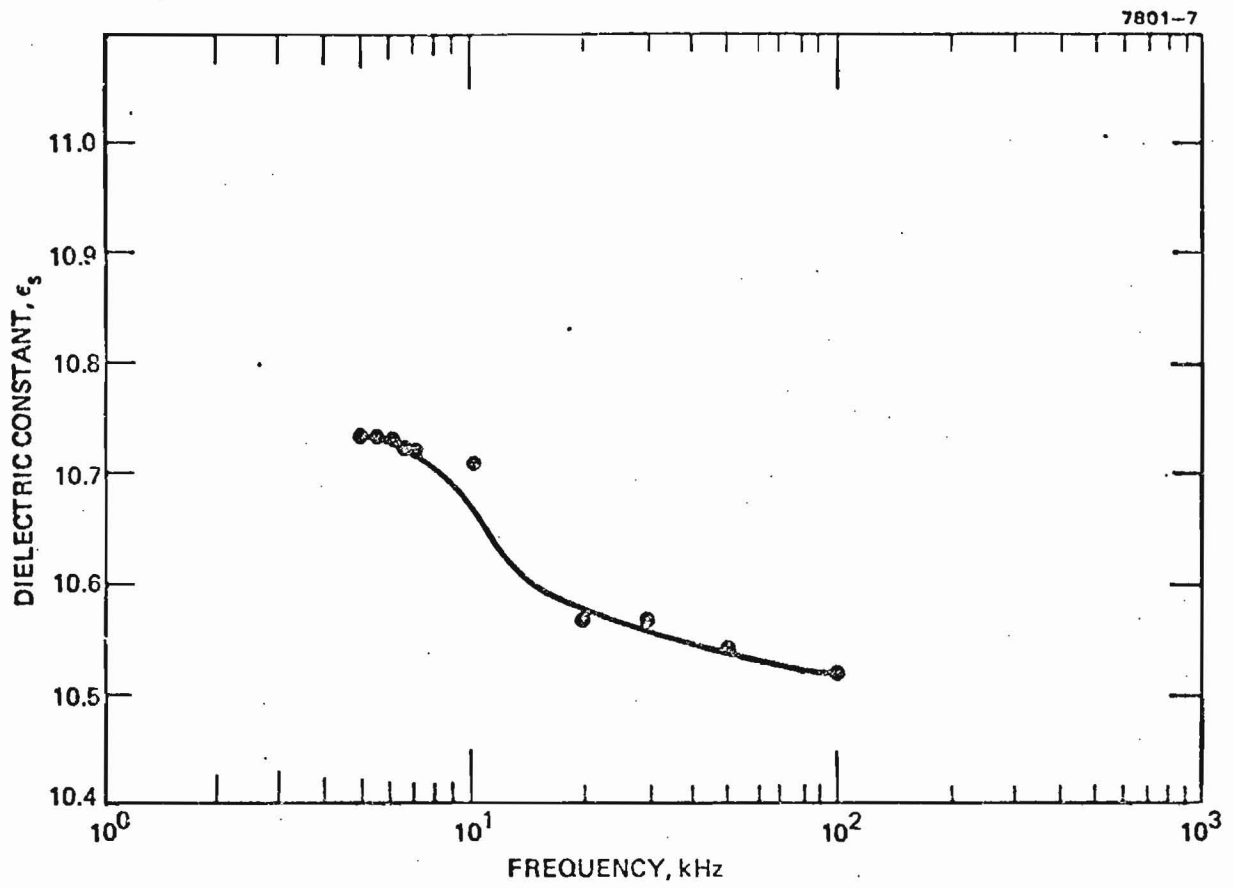


Figure 28.  $\text{GeS}_2$  dielectric constant as a function of frequency.

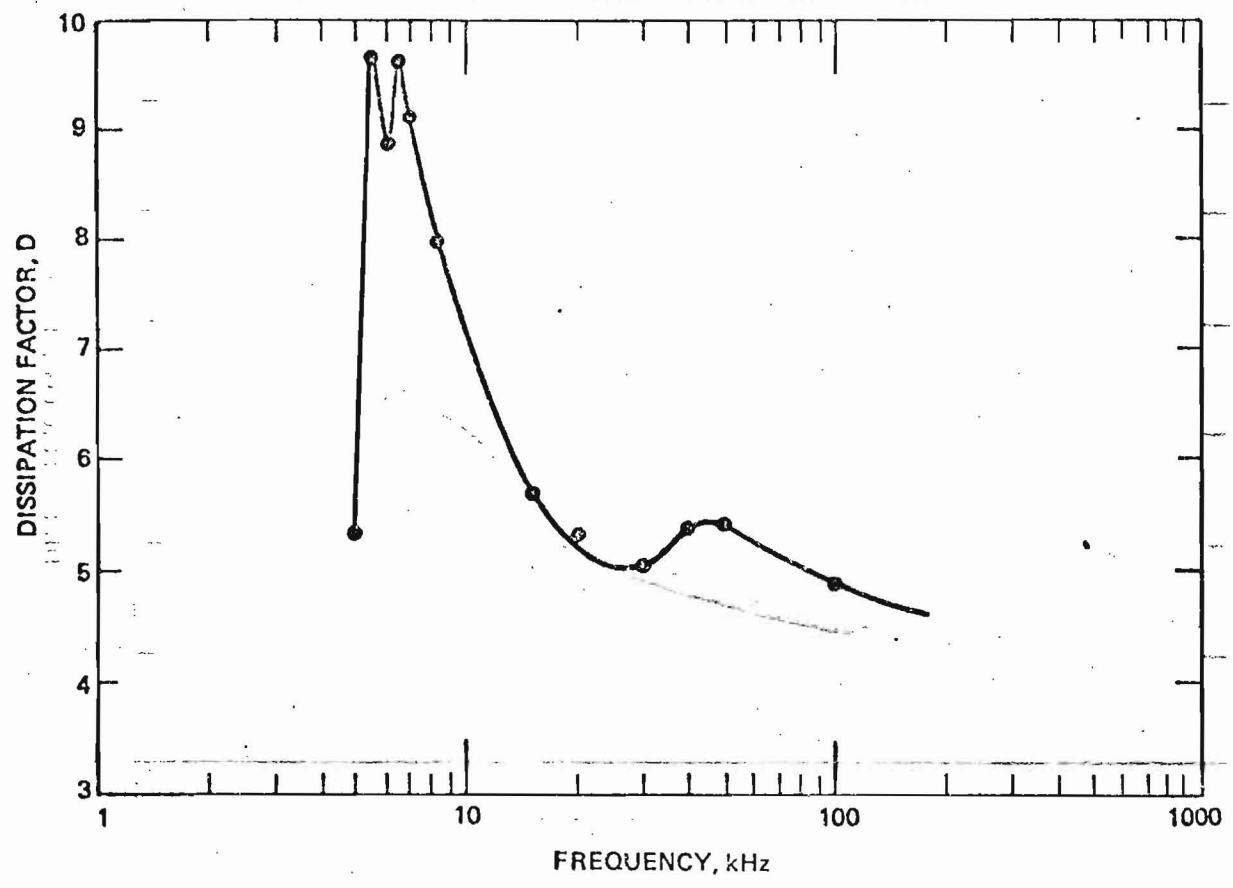


Figure 29. Dissipation factor versus frequency. Sample is GeS<sub>2</sub>.



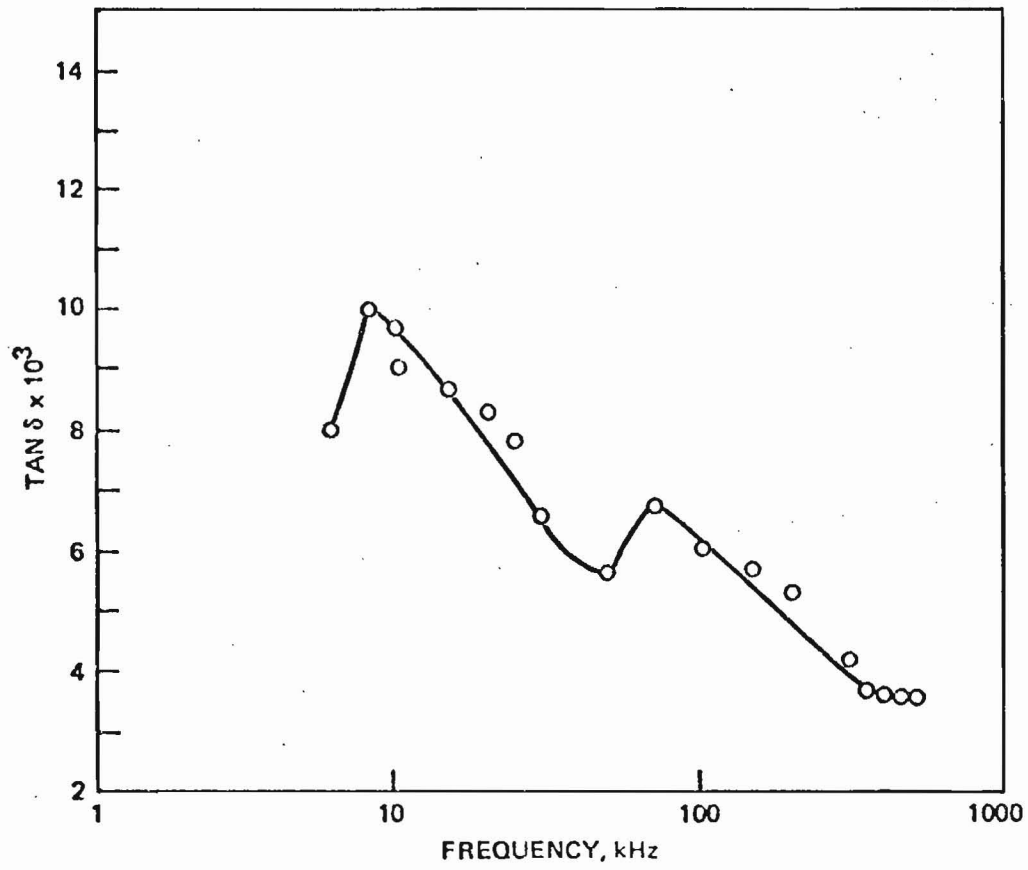


Figure 30.  $\text{Tan } \delta$  versus frequency for  $\text{GeSe}_2$ .

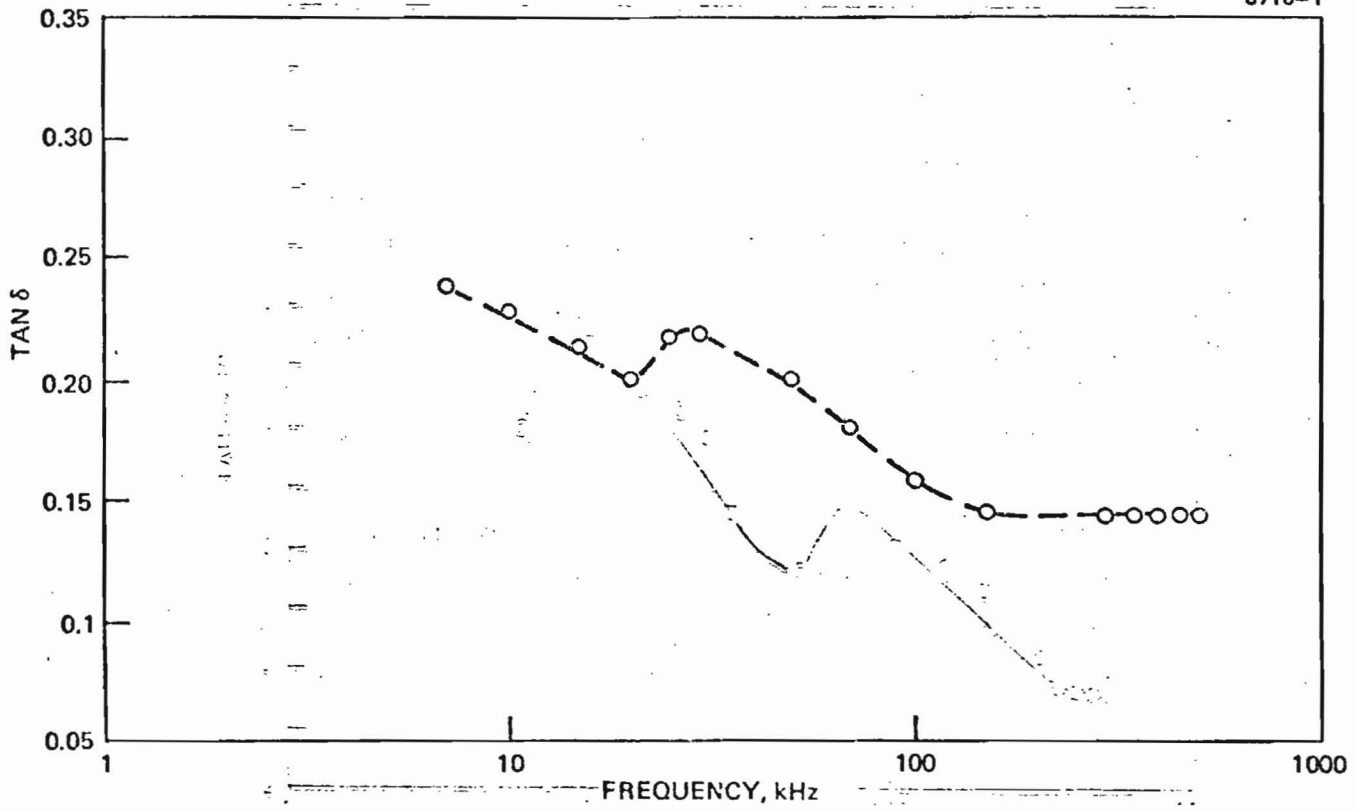


Figure 31. Dissipation factor versus frequency for  $\text{ZnGa}_2\text{S}_4$  (zinc thiogallate).

The dissipation factors, on the order of  $10^1$ , are fairly high as compared with the chalcogenides (listed above), which are on the order of  $10^{-3}$ . At present we do not understand these relaxation phenomena because of a lack of knowledge of the details of the local atomic arrangements and defect structures in this material.

### 3. AgGaTe<sub>2</sub>

The 0.5-in.-diameter boule, grown by the Bridgman-Stockbarger technique, was found to be polycrystalline along its entire length. A few large pieces were mined out for dielectric measurements. The average dielectric constant, measured at 1 MHz for this material, was 270 (Table 4). However, there were large variations in the measurements from sample to sample (nearly 35%), indicating variations in stoichiometry. IR transmission measurements (Figure 32) showed transmission of ~40% (uncorrected for Fresnel losses) at 2.5  $\mu\text{m}$ , decreasing in a manner typical of free-carrier absorption, becoming opaque beyond 4.5  $\mu\text{m}$ . From its composition and relationship to other chalcopyrites, transmission further out in the IR would be expected. DC resistivity for AgGaTe<sub>2</sub> was measured to be  $\sim 6 \times 10^7 \Omega\text{-cm}$ .

### 4. CdIn<sub>2</sub>Te<sub>4</sub>

The dielectric constant measurements and relaxation spectra for this material are shown in Tables 4 and 5. We attempted to detect ferroelectricity in this material by employing thermally induced depolarization currents in the range of 77 to 300°K. This work was done under the direction of Professor Ruben Braunstein, Department of Physics, UCLA. No peaks in the depolarization current versus temperature were observed, indicating the absence of the effect at least in the above temperature range. Similar measurements at high temperatures (300 to 750°K) also showed no peaks.

T9

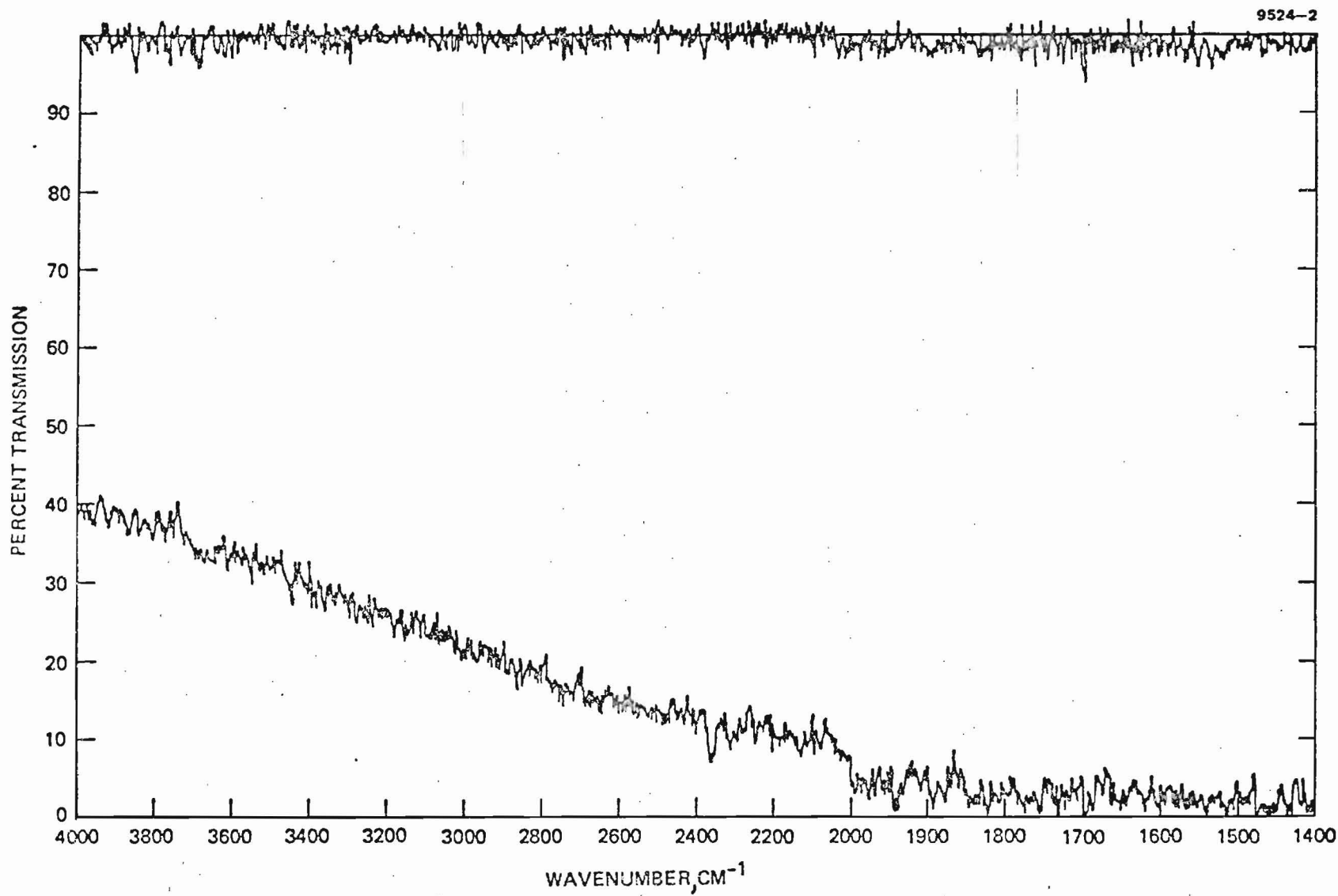


Figure 32. IR transmission spectrum: AgGaTe<sub>2</sub>.

The dielectric relaxation spectrum, a plot of the dissipation factor ( $\tan \delta$ ) versus frequency for  $\text{ZnSiAs}_2$ , is shown in Figure 33. There are two distinct peaks corresponding to frequencies of 60 kHz and 220 kHz, which correspond to relaxation times of 16  $\mu\text{sec}$  and 0.7  $\mu\text{sec}$ , respectively. Although sufficient details of the defect structure of this sample are not presently available to draw any definite conclusions, we can speculate that the shorter time constant, 0.7  $\mu\text{sec}$ , corresponds to the jump frequency of the lightest of host ions, silicon, into and out of Si vacancies. The longer time constant of 16  $\mu\text{sec}$  may be due to similar jump frequencies of the other host cation, zinc. The host anion, arsenic, because of its large mass, is not expected to respond to the applied high frequency of electric fields corresponding to the observed peaks.

### C. FAR-IR SPECTROSCOPY

Far-IR spectroscopy in the range of 5 to 100  $\text{cm}^{-1}$  was performed on all synthesized materials that were transparent in this section at these frequencies. Transmission spectra were obtained and analyzed under the direction of Professor Paul L. Richards, Department of Physics, University of California at Berkeley. The index of refraction is estimated from the measured mechanical thickness,  $t$ , and the observed wavelengths of the maximum,  $\lambda_{\text{max}}$ , and minimum,  $\lambda_{\text{min}}$ , in transmission:

$$\lambda_{\text{max}} = \frac{2n\lambda t}{m}$$

$$\lambda_{\text{min}} = \frac{4n\lambda t}{2m+1}$$

where  $m$  is any integer  $\geq 1$ . These equations are applied in the spectral regions where the complex part of the index is negligible. At these frequencies, the dielectric constant,  $\epsilon$ , is equal to the index of refraction squared:

$$\epsilon = n^2$$

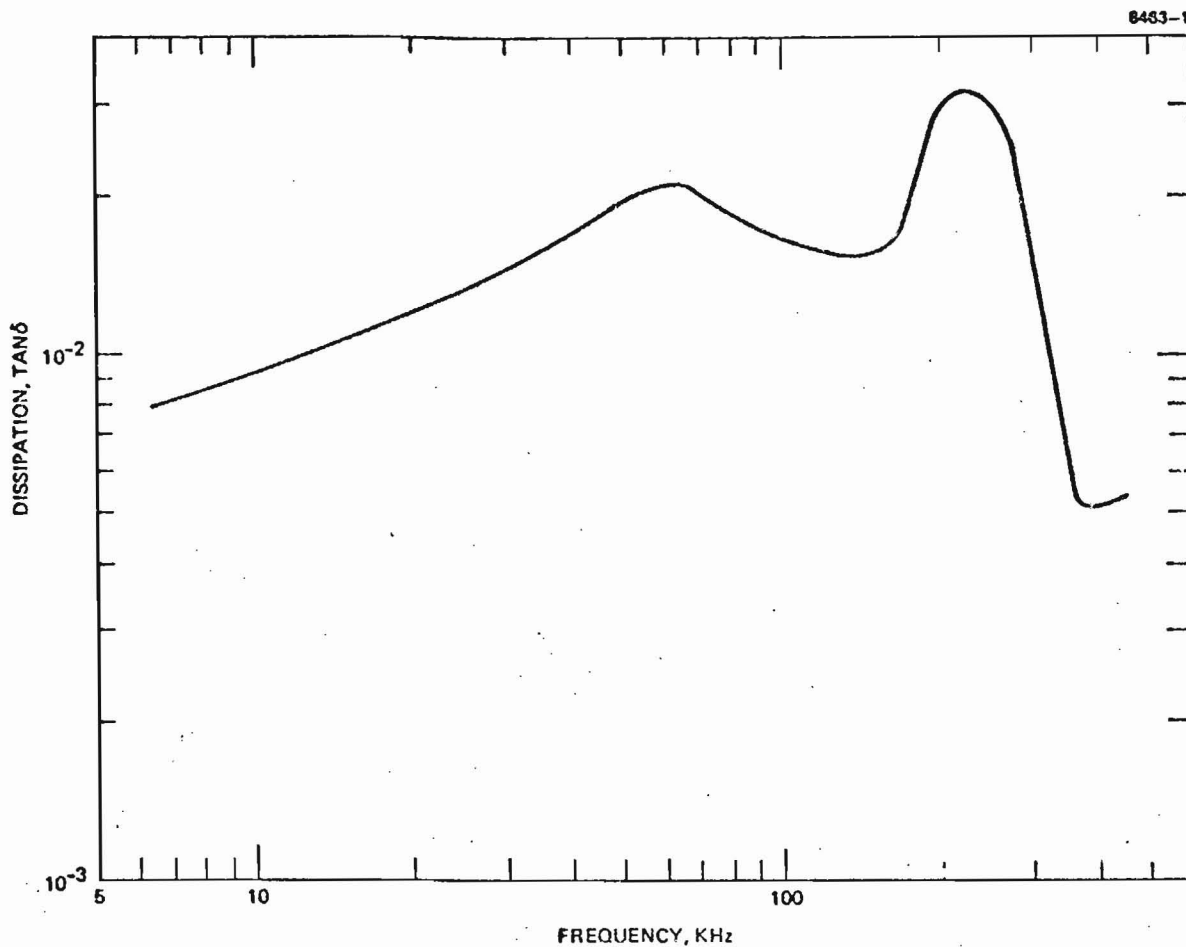


Figure 33. Dielectric relaxation of ZnSiAs<sub>2</sub>.

1. GeS<sub>2</sub>

The far-IR spectrum of GeS<sub>2</sub> is shown in Figure 34. The top curve (1) in Figure 34 shows the transmittance through a GeS<sub>2</sub> sample 0.356 mm thick at a temperature of 1.3°K. The spectrum shows interference fringes and sharp absorptions at 48 to 63 cm<sup>-1</sup>. Curve 2 shows the estimated index of refraction. The calculated dielectric constant from this data is in good agreement with measured values. The dispersion due to the 48 to 63 cm<sup>-1</sup> modes and also to higher modes shows clearly in the diagram.

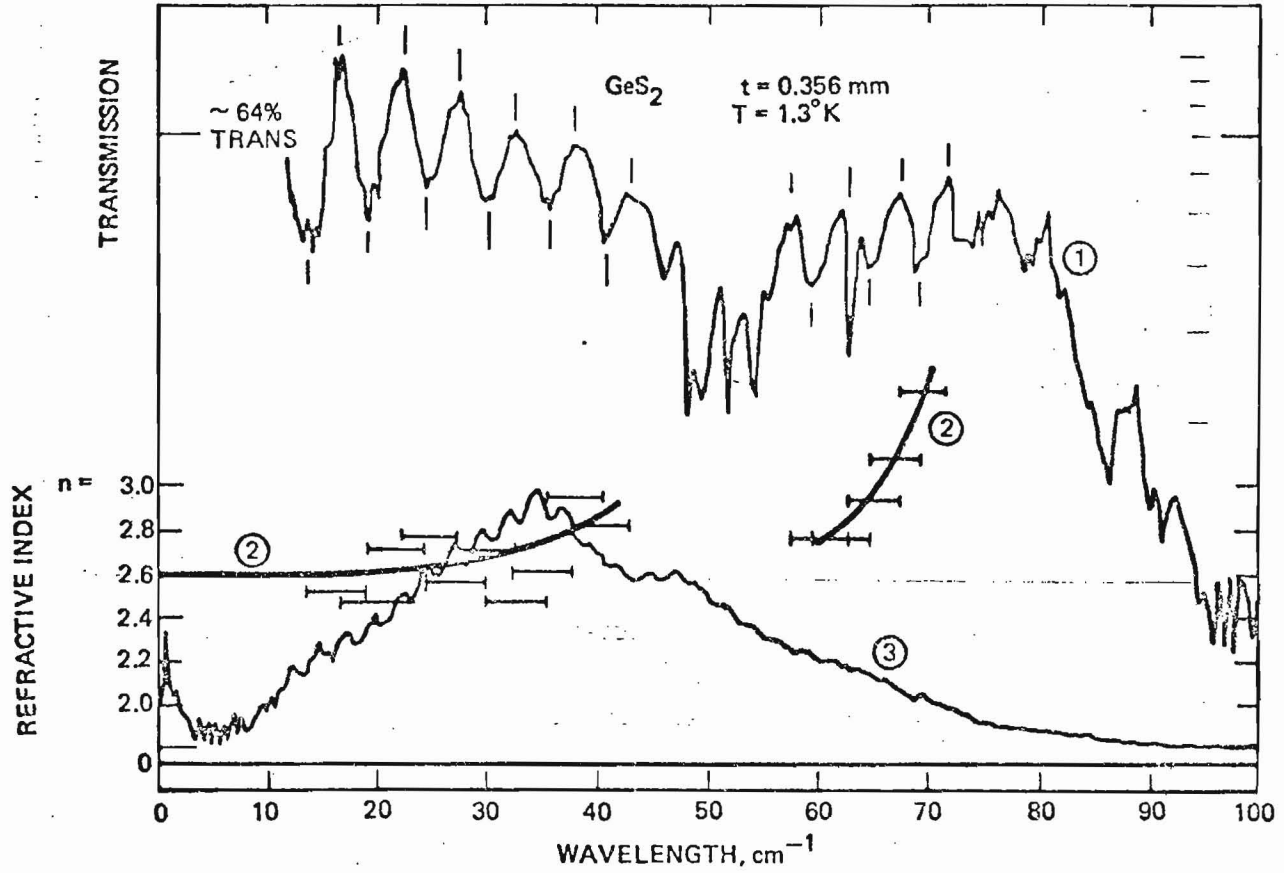


Figure 34. Far-IR transmission of  $\text{GeS}_2$  (Curve 1). Index of refraction of  $\text{GeS}_2$  as a function of wavelength (Curve 2). Curve 3 is empty sample cell.

2. AgInTe<sub>2</sub>

The far-IR transmission spectrum of AgInTe<sub>2</sub> (Figure 35) was determined and analyzed from a sample with a measured thickness of 0.113 cm. The index of refraction was determined to be 3.40, and no noticeable dispersion over the measured frequency range was observed.

3. CdIn<sub>2</sub>Te<sub>4</sub>

Far-IR transmission measurements on CdIn<sub>2</sub>Te<sub>4</sub>, without AR coatings, in the range of 500 to 40 cm<sup>-1</sup> wave numbers (corresponding to 20 to 2500 μm) show a constant relative transmission of 20% between 20 to 32 μm, followed by a medium absorption peak at 340 cm<sup>-1</sup> and two strong absorptions at 212 cm<sup>-1</sup> and at 125 cm<sup>-1</sup> (Figure 36). The nature of these absorptions is not yet understood and will require further transmission studies at low temperatures with increased instrument resolution.

4. AgInSe<sub>2</sub>

The spectrum for a 29.4-mil-thick sample of AgInSe<sub>2</sub> is shown in Figure 37. An average index of 3.18 in the indicated range was determined by this measurement.

5. TlSe

TlSe of 18.0-mil thickness (Figure 38) was determined to have an average index of 4.63 in the range 15 to 23 cm<sup>-1</sup>.

6. Mixed Crystal AgGa(S,Se)<sub>2</sub>

A sample of the mixed crystal AgGa(S,Se)<sub>2</sub>, where [S] = [Se], having a thickness of 58.9 mil was also evaluated in the spectral region of 0 to 40 cm<sup>-1</sup> (Figure 39). The index of refraction between 7 and 26 cm<sup>-1</sup> was determined to be 2.93 ± 0.05. Measured EO coefficient values of the end members, AgGaS<sub>2</sub> and AgGaSe<sub>2</sub>, have been reported at 3.2 x 10<sup>-2</sup> M/V and 3.8 x 10<sup>-12</sup> M/V, respectively.



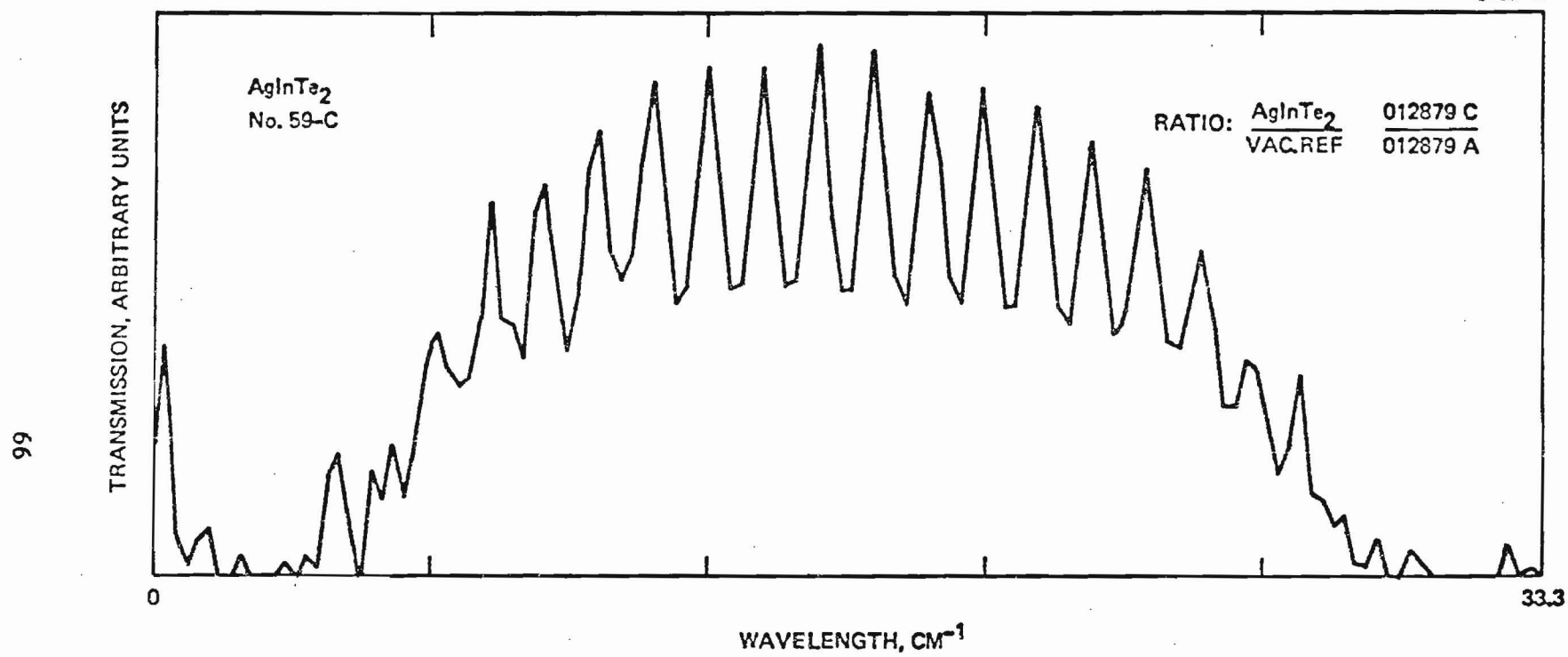


Figure 35. Far-IR transmission of AgInTe<sub>2</sub>.

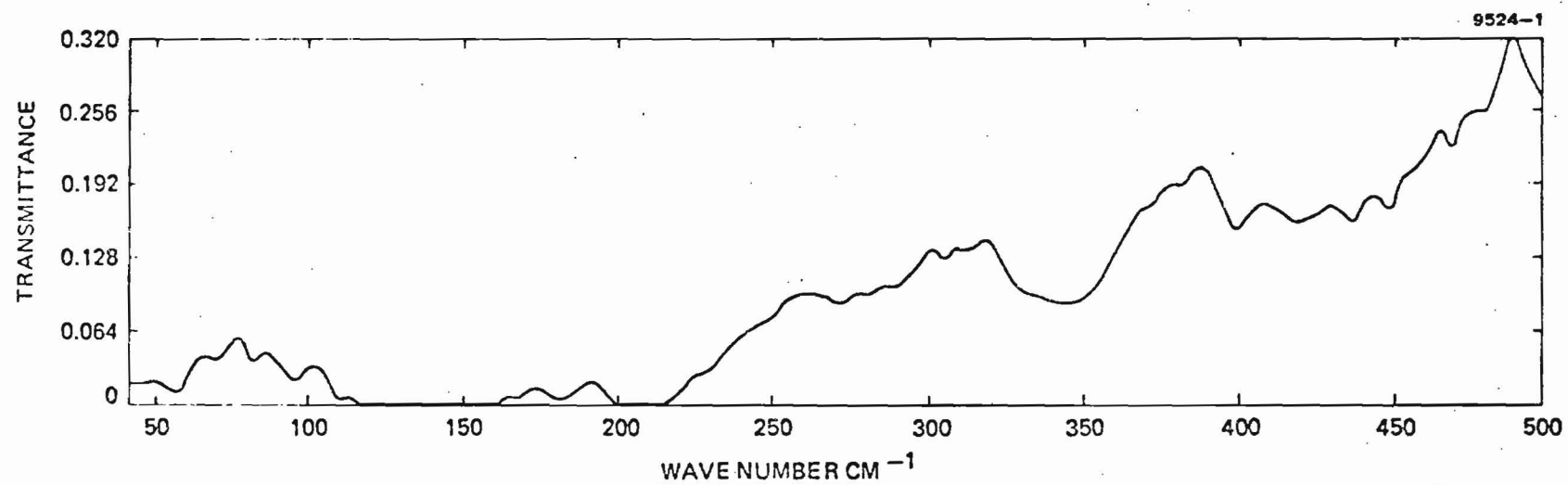


Figure 36. Far-IR transmission of CdIn<sub>2</sub>Te<sub>4</sub>.

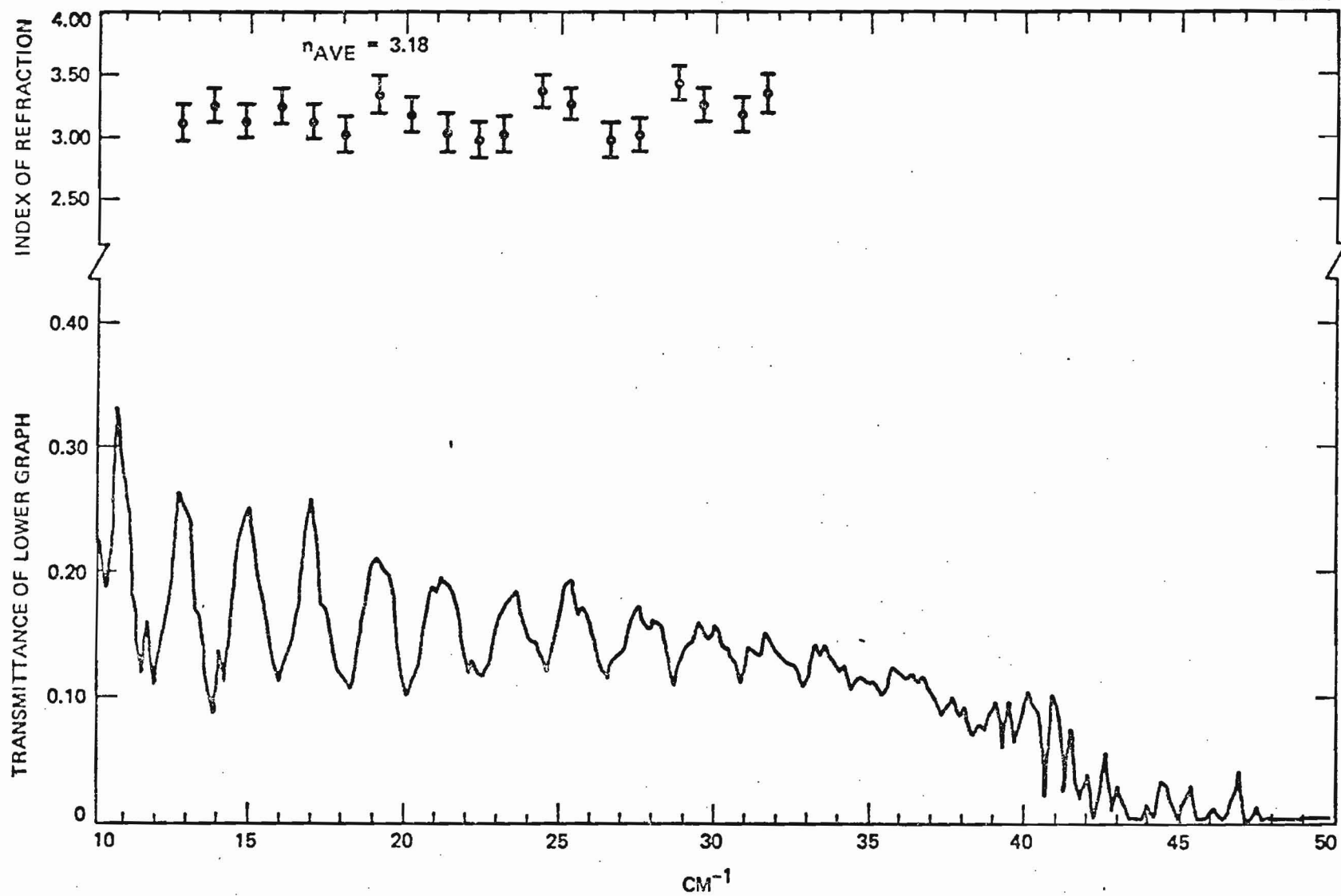


Figure 37. Far-IR transmission of  $\text{AgInSe}_2$ .

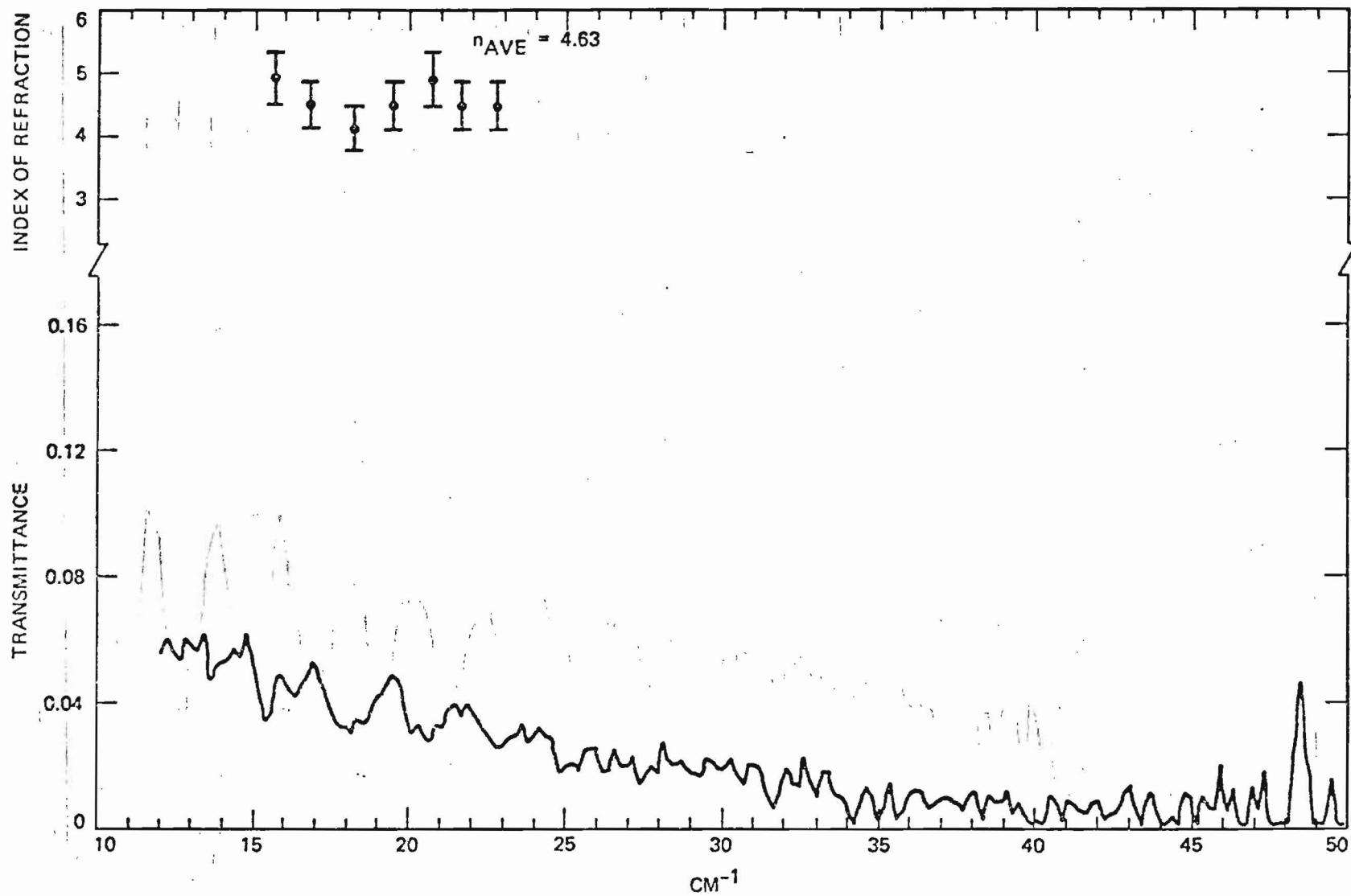


Figure 38. Far-IR transmission spectrum of TlSe.

Figure 38. Far-IR transmission spectrum of TlSe.

## 7. Other Samples

Samples of  $\text{CuInSe}_2$  and  $\text{Ag}_3\text{AsS}_3$  with thicknesses of 0.016 and 0.014 in., respectively, showed no far-IR transmittance at a sensitivity level of  $\tau < 10^{-3}$  over the frequency range  $10 < \nu < 40 \text{ cm}^{-1}$ .

All that we can conclude is that there is either very large absorption in these samples or that the index of refraction is much greater than 10, giving very high-Q Fabry-Perot resonances that are smeared out by irregularities in the sample thickness.

Additional samples submitted for measurement were not transparent in the far IR. Several low-resistivity samples with apparent free-carrier absorptions could not be analyzed by our methods.

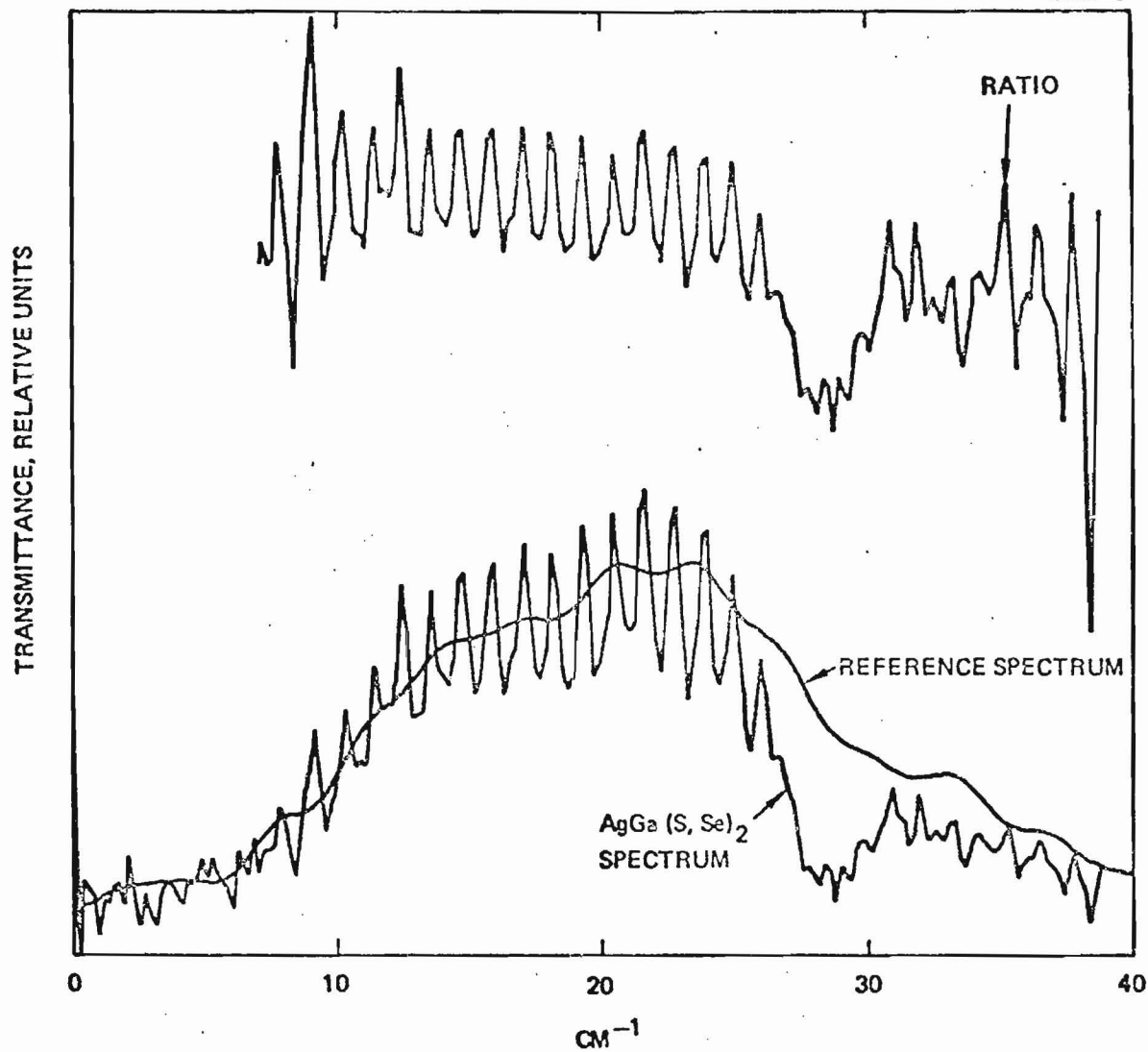


Figure 39. Far-IR transmission of  $\text{AgGa}(\text{S}, \text{Se})_2$ . Reference spectrum is scan without sample. Peaks above and below reference level indicate channel spectra due to resonances in sample. Ratio represents transmittance (i.e., ratio of sample spectrum (point-by-point) to reference spectrum).

## SECTION 5

### THEORETICAL MODEL: ELECTROOPTIC EFFECT IN CRYSTALS

During this program, a parallel effort was pursued by Professor Amnon Yariv and Dr. C. Shih, Applied Physics Department at Caltech, to develop a theoretical model for the EO effect in coordination with the structural analog concepts pursued in this program. The prime motivation of the theoretical effort was to obtain an expression that could be used to calculate and predict the EO coefficient of new crystals. Yariv and Shih, by applying the localized bond charge model of Phillips and Van Veehten,<sup>17,18</sup> which attributes the dielectric response of covalent crystals to the localized bond charge, have developed a method for calculating the EO tensor coefficients. Comparisons with experimental values for binary compounds having zincblende and wurtzite structures were excellent. Their method and results are presented in detail in Appendix B (Ref. 19).

Yariv and Shih recently extended the calculation to ternary compounds (e.g.,  $\text{LiNbO}_3$ ,  $\text{CdIn}_2\text{Te}_4$ ), where they also find very good agreement. These results are presented in Table 6.

We applied the theoretical model for calculating the EO coefficient to the crystal  $\text{CdIn}_2\text{Te}_4$ . We used the following data:

- Covalent radii ( $\text{Cd}_j\text{In}_j\text{Te}$ ) - 1.405 Å
- Structure -  $\bar{4}$

Using published data of bond susceptibilities, we calculated the optical dielectric constant  $\epsilon_\infty = 7.25$ . Using the above data in the equations

$$\begin{aligned}
 (r_{ijk})_{\text{ionic}} = & - \frac{\epsilon_o (\epsilon'_{dck} - \epsilon'_{cok})}{V N e_c^* \epsilon'_i \epsilon'_j} \sum_{\mu} \frac{\beta^{\mu}}{r} \left[ (f_i \alpha_i^{\mu} \alpha_j^{\mu} \alpha_k^{\mu}) \right. \\
 & \left. + 1/2 (\alpha_i^{\mu} \delta_{jk} + \alpha_j^{\mu} \delta_{ik}) \right] \quad (1)
 \end{aligned}$$

Table 6. Results for  $\text{LiNbO}_3$  and  $\text{LiTaO}_3$

	$\text{LiNbO}_3$		$\text{LiTaO}_3$	
$\epsilon_{dc3}$	28		43	
$\epsilon_{dc1,2}$	43		41	
$\epsilon_c^*/\epsilon$	1.8		2.0	
	Nb-O (Short)	Nb-O (Long)	Ta-O (Short)	Ta-O (Long)
$2r_o$	1.889 Å	2.112	1.891	2.071
$f_i$	0.821	0.830	0.847	0.853
$-f$	0.292	0.241	0.282	0.238
	$r_{33}$	$r_{51}$	$r_{33}$	$r_{51}$
$r_{\text{ionic}}$	+19.9	+19.7	+27.8	+16.5
$r_{\text{elec}}$	+ 6.0	+ 0.8	+ 3.70	+ 0.24
$r_{\text{theo}}$	+25.9	+20.5	+31.5	+16.7
$r_{\text{sum}}$				
$r_{\text{exptl}}$	+28	+23	+30	+15

7209

$$f = \left( \frac{k_s r}{2} - 1.48 \right) f_i - 0.02 ,$$

we obtained

$$r_{41} = 220 \times 10^{-12} \text{ m/V} \pm 30\% .$$

This predicted value is a huge number (roughly 100X that of GaAs and 10X that of  $\text{LiNbO}_3$ ). The main difference between this crystal and  $\text{LiNbO}_3$ , as an example, is due to the factor:



$$\frac{\epsilon_{dc} - \epsilon_k}{\epsilon_i \epsilon_j},$$

which is equal to 8.55 in  $\text{CdIn}_2\text{Te}_4$  and to 1.02 in  $\text{LiNbO}_3$ . It will be very exciting to see if this prediction is actually true.

We also predict a large EO coefficient for  $\text{AnIn}_2\text{S}_4$  since it has  $3m$  symmetry so that the form

$$\sum_u \alpha_i^u \delta_{ijk}$$

is non-vanishing for  $r_{ijj}$ . The more numerical prediction awaits the result of measurement of  $\epsilon_{dc}$ .

## SECTION 6

### CONCLUSIONS AND RECOMMENDATIONS

At the conclusion of this study program, there are many observations and experiences to be noted. We have had a very successful program which has illuminated several possible materials having potentially high EO coefficients. These materials, especially  $\text{CdIn}_2\text{Te}_4$  and  $\text{AgGaTe}_2$ ; have been shown to have high dielectric constants, as we had predicted from the structural analog model. In addition, a new theoretical calculation (Appendix A) is now available for the calculation of the EO coefficients based on the localized band charge model of Phillips and Van Vechten. This was developed in a parallel effort by A. Yariv and C. Shih of Caltech.

Many problems arose during this program concerning materials synthesis, crystal growth, and measurements. We were grossly misled by many reports in the Russian literature, especially concerning crystal synthesis by vapor transport techniques. Fortunately, our association with Dr. Alexander Borshchevsky, formerly at the Center for Materials Research, Stanford University, led to the clarification of the Russian literature both as to content and quality.

In addition to misleading literature, the ternary chalcogenides have some unique synthesis problems. Particularly difficult are combinations where one of the binary constituents (e.g.,  $\text{In}_2\text{S}_3$  or  $\text{Ga}_2\text{S}_3$ ) is considerably more volatile than the other (e.g.,  $\text{ZnS}$  or  $\text{CdS}$ ). This typically creates problems in achieving the desired stoichiometry. An extreme example is  $\text{ZnIn}_2\text{S}_4$ , where we encountered approximately a dozen identified compounds of the type  $\text{Zn}_x\text{In}_y\text{S}_z$ . The desired stoichiometry,  $\text{ZnIn}_2\text{S}_4$ , was finally achieved by regrinding the other compounds and adding excesses of  $\text{In}_2\text{S}_3$  and  $\text{S}_2$ .

There are many areas of study (pointed out above) where considerably more work is needed. Surveying a wide range of compounds, especially "new" compounds where there is little information on synthesis or on properties, only serves to open more areas where research is needed. We have only scratched the surface to families of new materials with a wide variety of applications.

Many crystalline samples were fabricated but could not be measured because of their low resistivity. These samples, in addition, exhibited new transmission in the far IR due to free carrier absorption. Some annealing was attempted to increase resistivity by modifying crystal stoichiometry, but the scope of this program would not allow an in depth study of these phenomena.

The high dielectric constant and structural analog approach which led to the selection of new materials with potentially higher EO coefficients also carries with it the possibilities of higher nonlinear coefficients and higher acoustooptic figures of merit compared to known materials. The applications of these materials go beyond that which was our main objective — the EO tunable filter. New materials in these families can be selected with wide variations in band gap and phase matching from which to select new improved materials for frequency upconversion, parametric oscillators, SAW devices, modulators, and IR detectors.

We recommend that the study of these ternary compounds be continued with the applications in mind so that standard synthesis and crystal growth techniques can be developed to make them available for future devices.

In many aspects of the program, we have made measurements and observations, but, because of the limited depth of study required in any program of limited resources, we were unable to draw significant conclusions. One prime example is the work done in dielectric relaxation, where an in depth study of defects of the crystal would be required to understand and interpret the data.

In conclusion, we have developed a new approach which is now backed by theory for the selection of new materials with potential for higher performance in a variety of devices. This field should now be pursued in greater depth.

## REFERENCES

1. HALO Focal Plane Technology Program, Contract No. F04701-76-C-0174, Sponsored by Defense Advanced Research Projects Agency, Order No. 322, monitored by Air Force Space Division, to Strategic Systems Division, Electro-Optic and Data Systems Divisions, Hughes Aircraft Company, Culver City, California.
2. J. Lotspeich, Personal Communication, Hughes Research Laboratories, August 1977.
3. L.I. Berger and V.D. Prochukhan, "Ternary Diamond-Like Semiconductors," Consultants Bureau (New York - London, 1969).
4. Developed as part of HALO Program, see Reference 1.
5. F.A. Shunk, Constitution of Binary Alloys, 2nd Supplement, (McGraw Hill Co., 1969).
6. L. Thomassen et al., J. Electrochem Soc. 110, 1127 (1963).
7. Now located at General Radio Corp., Palo Alto, California.
8. J. Rivet, J. Flahut, and P. Laruelle, Compt. Rendue Acad. Sci. (Paris) 257, 161 (1963); J. Rivet, Ann. Chim. (Paris) 10, 5 and 6, 243 (1965).
9. H. Hahn, W. Klinger, P. Ness, and H. Schulze, Naturwissen 53, 18 (1966).
10. E. Parthé and J. Garin, Monatshelfte für Chemie 102, 1197 (1971).
11. L.S. Palatnik, V.M. Koshkin, L.P. Galchinetski, V.I. Kolesnikov, and Yu. V. Komnik, Sov. Phys. Solid State 4, 1052 (1962).
12. G.K. Averkieva, A.A. Viapolin, and N.A. Gorunova, "Soviet Research on New Materials," Ed. D.N. Nasledov and N.A. Goryunova, Consultants Bureau, New York (1965).
13. M. Khanafer, O. Gorochov, and J. Rivet, Mat. Res. Bull. 9, 1543 (1974).
14. B.R. Pamplin, Scientific Advisers Report SAMSS 5/65 (1965).
15. B.B. Sharma, PhD. Thesis, University of Delhi (1979).

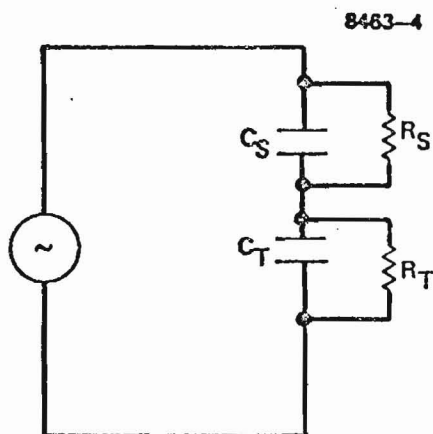
16. L.S. Van der Pauw, Phillips Res. Repts. 13:1 (1958).
17. J.C. Phillips, Phys. Rev. Lett. 20, 550 (1968).
18. J.A. Van Vechten, Phys. Rev. 182, 891 (1969); 187, 1007 (1969).
19. C-C Shih and A. Yariv, Phys. Rev. Letters 44, 281 (1980).

APPENDIX A

ANALYSIS OF CAPACITANCE MEASUREMENTS USING BLOCKING CONTACTS

Problem:

An impedance bridge measures the total capacitance  $C_M$  and the total resistance (equivalent shunt)  $R_M$  of the two capacitors  $C_S$  and  $C_T$  in series at a frequency  $f$ . The bridge independently also measures  $C_S$  and  $R_S$ . Find the value of  $C_T$  and  $R_T$ .



Solution:

Since  $C_S$  and  $R_S$  are in parallel, the net (total) impedance  $Z_S$  of  $C_S$  and  $R_S$  is given by

$$\frac{1}{Z_S} = \left\{ \frac{1}{R_S} + \frac{C_S \omega}{j} \right\},$$

where  $\omega = 2\pi f$ , and  $j = \sqrt{-1}$ . Therefore, it follows that

$$Z_S = \frac{R_S}{(1 + \omega^2 R_S^2 C_S^2)} + j \frac{R_S^2 C_S \omega}{(1 + \omega^2 R_S^2 C_S^2)}.$$

Similarly for the circuit of  $C_T$  and  $R_T$ ,

$$Z_T = \frac{R_T}{1 + \omega^2 R_T^2 C_T^2} + j \frac{R_T^2 C_T \omega}{1 + \omega^2 R_T^2 C_T^2}.$$

Since  $Z_S$  and  $Z_T$  are in series, the total measured  $Z_M$  is equal to  $Z_S + Z_T$ . The measurement of  $Z_M$  yields a value for  $R_M$  and  $C_M$  since

$$Z_M = \left\{ \frac{1}{R_M} + \frac{C_M \omega}{j} \right\}^{-1}$$

$$= \frac{R_M^2}{1 + \omega^2 R_M^2 C_M^2} + j \frac{R_M^2 C_M \omega}{1 + \omega^2 R_M^2 C_M^2}$$

From  $Z_M = Z_S + Z_T$ , we get, after equating real and imaginary parts,

$$\frac{R_M}{1 + \omega^2 R_M^2 C_M^2} = \frac{R_S}{1 + \omega^2 R_S^2 C_S^2} + \frac{R_T}{1 + \omega^2 R_T^2 C_T^2} \quad (A-1)$$

and

$$\frac{R_M^2 C_M}{1 + \omega^2 R_M^2 C_M^2} = \frac{R_S^2 C_S}{1 + \omega^2 R_S^2 C_S^2} + \frac{R_T^2 C_T}{1 + \omega^2 R_T^2 C_T^2} \quad (A-2)$$

Therefore,

$$\frac{R_T}{1 + \omega^2 R_T^2 C_T^2} = \frac{R_M}{1 + \omega^2 R_M^2 C_M^2} - \frac{R_S}{1 + \omega^2 R_S^2 C_S^2} = \theta, \text{ a constant,}$$

since  $R_M$ ,  $R_S$ ,  $C_M$ ,  $C_S$ , and  $\omega$  are measured values. Then it follows that

$$R_T = \theta + \omega^2 R_T^2 C_T^2 \theta$$

Similarly, from Eq. A-2 we get

$$\frac{R_T^2 C_T}{1 + \omega^2 R_T^2 C_T^2} = \frac{R_M^2 C_M}{1 + \omega^2 R_M^2 C_M^2} - \frac{R_S^2 C_S}{1 + \omega^2 R_S^2 C_S^2} = \lambda, \text{ a constant} \quad (A-3)$$

and

$$R_T^2 C_T^2 = \lambda + \lambda \omega^2 R_T^2 C_T^2 \quad (A-4)$$

Thus, for the two unknowns  $C_T$  and  $R_T$ , we have two equations:

$$R_T^2 C_T^2 \omega^2 \theta - R_T + \theta = 0 \quad (A-5)$$

and

$$R_T^2 C_T^2 - \lambda - \lambda \omega^2 R_T^2 C_T^2 = 0 \quad (A-6)$$

The simplest solution will be derived from Eq. A-5:

$$C_T^2 = \frac{R_T - \theta}{R_T^2 \omega^2 \theta}$$

or

$$C_T = \pm \sqrt{\frac{R_T - \theta}{R_T^2 \omega^2 \theta}}$$

Since only positive roots are possible, we can write

$$C_T = \frac{1}{R_T \omega} \sqrt{\frac{R_T - \theta}{\theta}}$$

Substituting for  $C_T^2$  in Eq. A-5, after squaring both sides of Eq. A-6, yields



$$R_T^4 C_T^2 = \lambda^2 + 2\lambda^2 \omega^2 R_T^2 C_T^2 + \lambda^2 \omega^4 R_T^4 C_T^4$$

From this we obtain

$$R_T^4 = \frac{(R_T - \theta)^2}{R_T^2 \omega^2 \theta} = \lambda^2 + 2\lambda^2 \omega^2 \frac{R_T^2 (R_T - \theta)}{R_T^2 \omega^2 \theta} + \frac{\lambda^2 \omega^4 R_T^4 (R_T - \theta)^2}{R_T^4 \omega^4 \theta^2}$$

or

$$R_T^2 \frac{(R_T - \theta)}{\omega^2 \theta} = \lambda^2 + \frac{2\lambda^2}{\theta} (R_T - \theta) + \frac{\lambda^2 (R_T - \theta)^2}{\theta^2}$$

$$\theta R_T^2 (R_T - \theta) = \lambda^2 \omega^2 \theta^2 + 2\lambda^2 \omega^2 \theta (R_T - \theta) + \lambda^2 \omega^2 (R_T - \theta)^2$$

or

$$\lambda^2 \omega^2 R_T^2 - 2\lambda^2 R_T \theta + \lambda^2 \theta^2 + 2\lambda^2 \theta R_T - 2\lambda^2 \theta^2 + \lambda^2 \theta^2 = R_T^3 \theta - R_T^2 \theta^2$$

Therefore,

$$R_T^3 \theta - R_T^2 \theta^2 = \lambda^2 \omega^2 R_T^2$$

giving

$$R_T \theta = \lambda^2 \omega^2 + \theta^2$$

$$R_T = \frac{\lambda^2 \omega^2}{\theta} + \theta$$

and

$$C_T = \sqrt{\frac{R_T - \theta}{\theta}} / R_T \omega$$

$$= \sqrt{\frac{\frac{\lambda^2 \omega^2}{\theta} + \theta - \theta}{\theta}} / R_T \omega$$

$$= \pm \frac{\lambda}{R_T} = \frac{\lambda}{R_T} = \frac{\lambda \theta}{\lambda^2 \omega^2 + \theta^2} \cdot$$

Quantitative Calculation of Electro-Optic Coefficients of Diatomic Crystals

Chun-Ching Shih and Amnon Yariv<sup>(a)</sup>

Department of Applied Physics, California Institute of Technology, Pasadena, California 91125

(Received 19 September 1979)

The bond-charge dielectric theory of Phillips and Van Vechten is applied to the calculation of the electro-optic tensor coefficients. The agreement of the theoretical predictions with experimental values in the case of zinc blende and wurtzite crystals is very good.

The second-order nonlinear optical response of asymmetric crystals is usually represented by the relation  $P_i^{(\omega+\Omega)} = \chi_{ijk} E_j^{(\omega)} E_k^{(\Omega)}$  between the amplitude of the induced polarization at  $\omega + \Omega$  and the inducing field amplitudes at  $\omega$  and  $\Omega$ . The case when both  $\omega$  and  $\Omega$  are optical frequencies, that is, frequencies above the lattice response but below optical absorption, has been considered by Levine.<sup>1</sup> He used the localized bond-charge model [see Fig. 1(a)] of Phillips and Van Vechten<sup>2,3</sup> (PV) which attributes the dielectric response of covalent crystals to the localized bond charge resulting in a linear susceptibility:

$$\chi = (h\Omega_p)^2 / E_g^2 \tag{1}$$

Here  $\Omega_p$  is the plasma frequency due to valence electrons and  $E_g$ , the effective energy gap, is given by  $E_g^2 = E_h^2 + C^2$ , where  $E_h$  is the homopolar component and  $C$  the heteropolar (ionic) component of the gap energy. Levine starts with the linear dielectric response  $P_i^{(\omega)} = \chi_{ij} E_j^{(\omega)}$ , taking

$\chi_{ij}$  to be an instantaneous function of the second field  $E_k^{(\Omega)}$ . This field causes a change  $\Delta r_\alpha (= -\Delta r_\beta)$  in the bond charge position, as shown in Fig. 1(b), which oscillates at  $\Omega$ . The explicit dependence of  $E_j$  and  $C$  on  $r_\alpha$  given by PV is then used to obtain  $\chi_{ijk}$ , where

$$\begin{aligned} \chi_{ij} &= \chi_{ij}^{(0)} + \Delta \chi_{ij}(t) \\ &= \chi_{ij}^{(0)} + 2\chi_{ijk} E_k^{(\Omega)} \cos \Omega t. \end{aligned} \tag{2}$$

If the frequency  $\Omega$  is below the lattice response region (we will refer to it in this case as "low"), then in addition to the purely electronic nonlinear response described above we now have a contribution to  $\chi_{ijk}$  due to the fact that now the crystal ions are capable of following the field  $E_k^{(\Omega)} \cos \Omega t$ . This is illustrated in Figs. 1(c) and 1(d). In addition to the displacement  $\Delta r_\alpha$  of the covalent bond charge we now have an elongation  $\Delta d_0$  of the atomic separation as well as a rotation  $\Delta \theta$  of the bond direction, both caused by the ionic displacement  $\Delta x_k$ .  $\Delta x_k$  is obtained from "low"-frequency dielectric constant measurements and is used to determine  $d_0$  and  $\Delta \theta$ . We use, in the spirit of Levine,<sup>1</sup> the change  $\Delta d_0$  to calculate the corresponding change  $\Delta \chi \cos \Omega t$  in bond susceptibility. This will give rise to a polarization  $P_i^{(\omega+\Omega)} = \chi_{ijk} E_j^{(\omega)} E_k^{(\Omega)}$ . A second contribution to  $\chi_{ijk}$  is due to the rocking at  $\Omega$  of the bond angle ( $\theta = \theta_0 + \Delta \theta \cos \Omega t$ ) which yields a dipole component along the direction  $i$  at  $(\omega + \Omega)$  even when  $\Delta d_0 = 0$ .

In what follows we will obtain expressions for the ionic contributions to  $\chi_{ijk}$  which are due to  $\Delta d_0$  and  $\Delta \theta$ . When the result is added algebraically to  $\chi_{ijk}^{elec}$ , as measured by second-harmonic-generation experiments or calculated by Levine,<sup>1</sup> the result is the total nonlinear tensor  $\chi_{ijk} = \chi_{ijk}^{ionic} + \chi_{ijk}^{elec}$ . The constants  $\chi_{ijk}$  thus determined are those which characterize the linear electro-optic (Pockels) effect. The relationship between the conventionally defined electro-optic tensor  $r_{ijk}$  and  $\chi_{ijk}$  is

$$\chi_{ijk} = -(\epsilon_i \epsilon_j / 2\epsilon_0) r_{ijk} \tag{3}$$

The linear susceptibility of a diatomic crystal

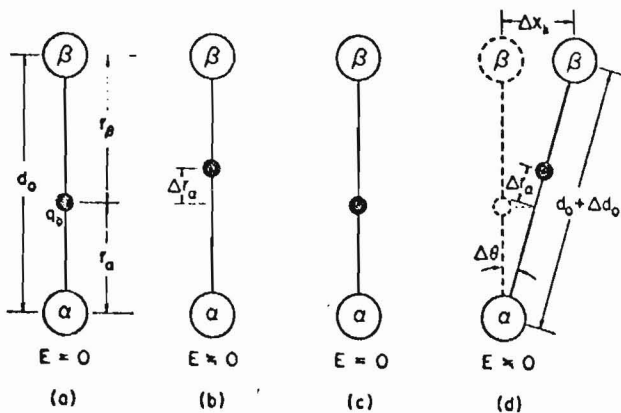


FIG. 1. The response of the ions and the bond charge to the applied electric field. In (a) and (b) the frequency of the field is higher than the lattice response. Only the bond charge is displaced, while the ions remain stationary. In (c) and (d) the frequency of the field is lower than the lattice response. It induces a displacement of the bond charge ( $\Delta r_\alpha$ ), a variation of the bond length ( $\Delta d_0$ ), and a bond rotation ( $\Delta \theta$ ).

is given as  $\chi = (h\Omega_p)^2/E_g^2$ .<sup>2</sup> The ionicity and covalency of the bond are defined as  $f_i = C^2/E_g^2$ ,  $f_c = E_h^2/E_g^2$ .<sup>3</sup> The expressions used in the evaluation of  $E_h$  and  $C$  are<sup>1,2</sup>

$$E_h \propto r_0^{-s}, \quad s = 2.48, \quad (4)$$

$$C \propto \exp(-k r_0)(Z_\alpha/r_\alpha - Z_\beta/r_\beta)e^2, \quad (5)$$

$$r_\alpha \approx r_\beta \approx r_0 = d_0/2,$$

where  $d_0 = r_\alpha + r_\beta$  is the bond length,  $r_{\alpha, \beta}$  are the atomic radii, and  $\exp(-k r_0)$  is the Thomas-Fermi screening factor. In order to consider crystals with highly unequal atomic radii, a generalized form for  $E_h$  was proposed<sup>1</sup> as

$$E_h^{-1} \propto r_0^{-2s} \frac{[(r_\alpha - r_c)^{2s} + (r_\beta - r_c)^{2s}]}{2(r_0 - r_c)^{2s}}, \quad (6)$$

where  $r_c$  is the average core radius.

The linear macroscopic susceptibility tensor  $\chi_{ij}$  is related to the bond polarizability  $\beta_n$  by

$$\chi_{ij} = V^{-1} \sum_n \alpha_{ni} \alpha_{nj} \beta_n, \quad (7)$$

where  $V$  is the volume of unit cell,  $\alpha_{ni}$  is the direction cosine of the  $n$ th bond, and the summation is over all the bonds in a unit cell. Although PV describe the macroscopic susceptibility  $\chi$  in terms of the average energy gap, we assume that  $E_h$  and  $C$  are also related to the bond polarizability directly, i.e.,

$$\beta_n \propto (h\Omega_p)^2/E_g^2. \quad (8)$$

When the bond length varies, it is reasonable to assume that the ratio of  $r_\alpha$  and  $r_\beta$  remains constant. With this assumption, the two independent parameters,  $r_{\alpha, \beta}$ , can be transformed into two quantities which relate directly to the macroscopic properties of crystals:

$$\Delta r_\alpha = (r_\alpha/d_0)\Delta d_0 + \delta$$

$$\Delta r_\beta = (r_\beta/d_0)\Delta d_0 - \delta, \quad (9)$$

where  $\delta$  is the displacement of the bond charge in the case of no bond elongation,  $\Delta d_0 = 0$ . From Eqs. (5), (6), (8), and (9), the change of bond polarizability is obtained as (here we drop the bond index  $n$ )

$$\frac{\Delta \beta}{\beta} = \left[ f_i \left( 1 + \frac{k r_0}{2} \right) + s f_c - \frac{3}{2} \right] \frac{\Delta d_0}{r_0} + \left[ 4 f_i \frac{Z_\alpha + Z_\beta}{Z_\alpha - Z_\beta} + S(2s - 1) \frac{f_c \rho d_0^2}{(r_0 - r_c)^2} \right] \frac{\delta}{d_0}, \quad (10)$$

where  $\rho = (r_\alpha - r_\beta)/(r_\alpha + r_\beta)$ . In the first term,  $k r_0/2$  is obtained because the screening wave number  $k_s$  is proportional to  $d_0^{-1/2}$ ,<sup>4</sup> and the number  $-3/2$  is because  $\Omega_p$  is proportional to  $d_0^{-3/2}$ . The second term on the right-hand side of (10) is identical to that obtained by Levine in his calculation of the nonlinear optical susceptibility.<sup>5</sup> The first term, which is proportional to  $\Delta d_0$ , is thus the ionic contribution of a single bond due to bond stretching.

The rotational contribution can be obtained by considering the changes in bond direction cosines. These are related to the ionic displacement  $\Delta x_k$  by  $\Delta \alpha_{ni} = (\delta_{ik} - \alpha_{ni} \alpha_{nk}) \Delta x_k$ .

From (7) we have

$$\Delta \chi_{ij} = V^{-1} \sum_n (\alpha_{ni} \alpha_{nj} \Delta \beta_n + \Delta \alpha_{ni} \alpha_{nj} \beta_n + \alpha_{ni} \Delta \alpha_{nj} \beta_n). \quad (11)$$

The complete ionic contribution to the nonlinear susceptibility is thus

$$\Delta \chi_{ij}^{ion} = \left\{ \sum_n (\beta_n / V r_0) \left[ f \alpha_{ni} \alpha_{nj} \alpha_{nk} + \frac{1}{2} (\alpha_{ni} \delta_{jk} + \alpha_{nj} \delta_{ik}) \right] \right\} \Delta x_k, \quad (12)$$

where

$$f = f_i \left[ 1 + \frac{1}{2} (k r_0) \right] + s f_c - 2.5 = \left[ \left( \frac{1}{2} k r_0 \right) - 1.48 \right] f_i - 0.02. \quad (13)$$

$\Delta x_k$  is related to the dielectric constant of the crystal as

$$N e_c^* \Delta x_k = \epsilon_0 (\epsilon_{dc}' - \epsilon_{\omega}' ) E_k, \quad (14)$$

where  $N$  is the number of pairs of atoms per unit cell,  $e_c^*$  is the Callen effective ionic charge,<sup>6</sup>  $\epsilon_{dc}'$  is the relative dielectric constant,  $\epsilon_{\omega}'$  is the relative optical permittivity, and  $E_k$  is the low-frequency electric-field component along the  $k$  direction.

Using (3) we obtain the final working expression for the ionic component of the electro-optic tensor:

$$r_{ijh}^{ion} = - \frac{\epsilon_0 (\epsilon_{dc}' - \epsilon_{\omega}')}{V N e_c^* \epsilon_0 \epsilon_{\omega}'} \left\{ \sum_n \frac{\beta_n}{r_0} \left[ f \alpha_{ni} \alpha_{nj} \alpha_{nh} + \frac{1}{2} (\alpha_{ni} \delta_{jh} + \alpha_{nj} \delta_{ih}) \right] \right\}. \quad (15)$$

TABLE I. Comparison of calculated and measured electro-optic coefficients (clamped) of zinc blende ( $r_{ij}$ ) and wurtzite ( $r_{3j}$ ) crystals (in units of  $10^{-12}$  m/V). The signs of  $r_{\text{expt}}$  have not been determined except where specified.

	GaAs	GaP	Zinc blende			Wurtzite			
			ZnSe	ZnS	ZnTe	CuCl	ZnS	CdS	CdSe
$\epsilon_{dc}'^a$	13.2	12.0	9.1	8.3	10.1	7.5	8.7 <sup>c</sup>	9.5	10.2
$f$	-0.09	-0.11	-0.16	-0.18	-0.12	-0.21	-0.18	-0.16	-0.15
$e_c^*/e$	0.20	0.23	0.33	0.35	0.26	0.27	0.35	0.41	0.36
$r_{\text{ion}}^b$	+1.03	+1.53	+2.64	+2.93	+2.07	-5.56	+3.63	+3.80	+3.61
$r_{\text{elec}}^b$	-2.73	-3.20	-4.68	-4.77	-6.41	+2.66	-5.63	-6.71	-7.40
$r_{\text{sum}}^{\text{theo}}$	-1.7	-1.7	-2.0	-1.8	-4.3	-2.9	-2.0	-2.9	-3.8
$r_{\text{expt}}^a$	-1.5	-1.1	2.0	1.6	4.3	-2.4	1.8	2.4	4.3

<sup>a</sup>I. P. Kamlnow and E. H. Turner, in *Handbook of Lasers*, edited by R. J. Pressley (Chemical Rubber Co., Cleveland, 1971), p. 453.

<sup>b</sup>S. Singh, in *Handbook of Lasers*, edited by R. J. Pressley (Chemical Rubber Co., Cleveland, 1971), p. 489.

<sup>c</sup>I. B. Kobayakov, *Kristallografiya* **11**, 419 (1966) [*Soviet Phys. Cryst.*, **11**, 369 (1966)].

For wurtzite crystals, we neglect the small distortion from the perfect tetragonal structure.  $\beta_n$  can be expressed in terms of the measured macroscopic susceptibility  $\chi$  as in (7), and the electro-optic coefficients of zinc blende and wurtzite crystals are obtained as follows: zinc blende,

$$r_{14}^{\text{ion}} = 0.3689 a_0^2 w f / (e_c^* / e); \quad (16)$$

wurtzite,

$$r_{33}^{\text{ion}} = -2r_{13}^{\text{ion}} = 0.4260 a_{\text{eff}}^2 w f / (e_c^* / e), \quad (17)$$

where  $a_{\text{eff}}^3 = \sqrt{3} a_0^2 c_0$ ,  $a_0$  and  $c_0$  are the lattice constants,  $w = (\epsilon - 1)(\epsilon_{dc} - \epsilon) / \epsilon^2$ , and  $r_{ij}$  are in units of  $10^{-12}$  m/V,  $a_0$  and  $a_{\text{eff}}$  in angstroms. Values of the parameters  $\epsilon_{dc}'$ ,  $f$ ,  $e_c^*$  are listed in Table I.

The dependence of the electro-optic coefficients  $r_{ijk}^{\text{ion}}$  on the bond geometry is perhaps the most illuminating feature to emerge from this work.

This dependence is contained in curly brackets in (15). For diatomic single-bond crystals  $\beta_n$  is a constant and the geometrical factor becomes

$$G_{ijk} = \left[ \sum_{\text{bonds } n} f \alpha_{ni} \alpha_{nj} \alpha_{nk} + \frac{1}{2} (\alpha_{ni} \delta_{jk} + \alpha_{nj} \delta_{ik}) \right].$$

The factor  $f$  is typically  $|f| \leq 0.3$ . Table II contains a listing of these factors for some key directions ( $ijk$ ) in crystals of the zinc blende, wurtzite and  $\text{LiNbO}_3$  classes. It follows immediately that when  $\sum_n \alpha_{ni} \neq 0$  the second term in  $G_{ijk}$  is an order of magnitude larger than the first one. In such crystals the ionic contribution to  $r_{ijk}$  is about an order of magnitude larger than the electronic term. This is the case in  $\text{LiNbO}_3$  or  $\text{LiTaO}_3$ . When  $\sum_n \alpha_{ni} = 0$ , as in zinc blende and wurtzite, we have to settle for the smaller term  $\sum_n f \alpha_{ni} \alpha_{nj} \alpha_{nk}$ . This is the main reason why  $\text{LiTaO}_3$  has  $r_{33} = 30.3$

TABLE II. Comparison of the geometrical factors between zinc blende, wurtzite, and  $\text{LiNbO}_3$ . The quantities shown have been divided by the number of bonds per unit cell,  $n_b$ .

	Zinc blende	Wurtzite	$\text{LiNbO}_3$	
			(Nb-O) <sub>short</sub>	(Nb-O) <sub>long</sub>
$n_b^{-1} \sum \alpha_{ni}$	0	0	0.475	-0.669
$n_b^{-1} \sum \alpha_{ni}^2$	$\frac{1}{3}$	$\frac{1}{3}$	$\frac{1}{3}$	$\frac{1}{3}$
$n_b^{-1} \sum \alpha_{ni} \alpha_{nj} \alpha_{nk}$ $= n_b^{-1} \sum \alpha_{ni}^2 \alpha_{nj}$	0	$-\frac{1}{9}$	0.184	-0.185
$n_b^{-1} \sum \alpha_{ni}^3$	0	$\frac{2}{9}$	0.107	-0.300

$\times 10^{-12}$  m/V, while in GaAs and ZnS,  $r_{41} \sim 2 \times 10^{-12}$  m/V.

The effective charge  $e_c^*$  is related to the Sziget effective charge  $e_s^*$  by  $e_c^* = [(\epsilon_\infty + 2)/3\epsilon_\infty]e_s^*$ . The value of  $e_c^*/e$  varies from 0.2 to 0.4 and seems to be independent of the number of valence electrons. The calculated values of  $r_{ijk}^{\text{ion}}$  using (17) and (18) are shown in Table I as  $r_{\text{ionic}}$ . The pure electronic contribution is entered as  $r_{\text{elec}}$ . It is obtained directly from the experimentally determined second-harmonic-generation coefficient by  $r_{ijk} = -4d_{ijk}/\epsilon^2$ . For most of the crystals in Table I,  $r_{\text{ionic}}$  is positive and  $r_{\text{elec}}$  is negative. Therefore, the predicted electro-optic coefficients,  $r_{\text{sum}}^{\text{theo}} = r_{\text{ionic}} + r_{\text{elec}}$ , involve the algebraic addition or cancellation of two numbers of comparable values. The only exception is CuCl. Because of the unfilled shell in Cu, the sense of bond polarization in CuCl is different from that in other crystals.<sup>7</sup> The signs of  $r_{\text{ionic}}$  and  $r_{\text{elec}}$  of CuCl are thus different from others. However, the magnitude of  $r_{\text{ionic}}$  is larger than that of  $r_{\text{elec}}$  in CuCl. We still obtain a negative electro-optic coefficient for CuCl. The predicted values in Table I are in good agreement with experiment. The worst case is GaP. It is interesting to note that the electronic contribution is about double the ionic contribution. This is in excellent agreement with the experimental observation.<sup>8</sup>

We intend to extend this model to complex crystals with different point-group symmetries. The generalization of the bond parameters used above

to multibond crystals has already been considered. The one parameter which will need added thought is  $e_s^*$ , the effective ionic charge. It was found empirically to be equal to  $C/\hbar\omega$ , in diatomic crystals.<sup>9</sup> If this relation and  $e_c^* = [(\epsilon_\infty + 2)/3\epsilon_\infty]e_s^*$  are valid in the more complex crystals, then our model can be applied to these cases. Calculations now in progress on  $\text{KH}_2\text{PO}_4$ ,  $\text{LiNbO}_3$ ,  $\text{LiTaO}_3$ , and ternary chalcopyrite crystals will be reported separately.

The authors acknowledge gratefully numerous discussions and suggestions from A. Gentile. This research was supported in part by the U. S. Air Force Office of Science Research.

<sup>(a)</sup>Consultant: Hughes Research Laboratories, Malibu, Cal. 90265.

<sup>1</sup>B. F. Levine, Phys. Rev. Lett. 22, 787 (1969), and 25, 440 (1970).

<sup>2</sup>J. C. Phillips, Phys. Rev. Lett. 20, 550 (1968).

<sup>3</sup>J. A. Van Vechten, Phys. Rev. 182, 891 (1969), and 187, 1007 (1969).

<sup>4</sup>C. Kittel, *Introduction to Solid State Physics*, (Wiley, New York, 1976), 5th ed.

<sup>5</sup>B. F. Levine, Phys. Rev. B 7, 2600 (1973).

<sup>6</sup>H. B. Callen, Phys. Rev. 76, 1394 (1949).

<sup>7</sup>I. P. Kaminow and E. H. Turner, Phys. Rev. B 5, 1564 (1972).

<sup>8</sup>W. L. Faust and C. H. Henry, Phys. Rev. Lett. 17, 1265 (1966).

<sup>9</sup>P. Lawaetz, Phys. Rev. Lett. 26, 697 (1971).